**The Dissertation Committee for Henry Fredrick Schreiner III certifies that this is the approved version of the following dissertation:**

# Methods and Simulations of Muon Tomography and Reconstruction

**Committee:**

---

**Roy Schwitters, Supervisor**

---

**Duane Dicus**

---

**Karol Lang**

---

**Peter Onyisi**

---

**Paul Navratil**

**Methods and Simulations of Muon Tomography and Reconstruction**

by

**Henry Fredrick Schreiner III, B.S.**

**Dissertation**

Presented to the Faculty of the Graduate School of
The University of Texas at Austin
in Partial Fulfillment
of the Requirements
for the degree of
**Doctor of Philosophy**

The University of Texas at Austin
May, 2016

Dedicated to Søren, who was born 8 weeks early so that he could be included here.

# Acknowledgments

First of all, I would like to thank my supervisor, Roy F. Schwitters, for the support and encouragement through the last six years. The detectors he designed are the core of this project, and amazingly kept working in adverse conditions to make the data presented in this work possible.

I would like to thank Marek Proga for his work on the design and construction of the detectors, and for his help and his work in Belize on the solar power system and debugging power problems with the detector. The late H Adam Stevens and John McGill, who worked on building the first three detectors, including the one that survived the ARL underwater experiment, are fondly remembered.

I would like to thank the students who have gone before me, such as CheukKai Hui, for laying the groundwork in the analysis that I am building on. Eric Wright wrote the original versions of the detector code, and came back several times to help me debug it. I would like to thank Garrick Thurston for building detector 4, currently collecting data in Belize.

I would also like to thank Carlos Villarreal his work on the detectors and FPGAs, and for his flexibility in making quick and repeated trips to Belize with or without me on short notice.

At the Applied Research Laboratories, Martin Barlett has been a valuable ally during the low momentum measurement and thereafter. Ricky Lenhart designed the underwater enclosure and worked diligently to ensure it was waterproof and durable. Axel Bigham provided transportation for us to the station on the lake, and operated the detector during many of the moves. Gary Wilson stepped in and helped with data collection and transfer when Marti was not available. And William Fergerson provided networking access to the detectors. Minh Van-Dinh, a student working on a project at ARL, prepared and ran the target runs during the summer of 2014.

I would like to acknowledge the Texas Advanced Computing Center (TACC) at The University of Texas at Austin for providing HPC resources that have contributed to the research results reported within this document. URL: http://www.tacc.utexas.edu

Finally, I would like to thank my wife Desirée for putting up long hours and encouraging me through setbacks during this time.

**Methods and Simulations of Muon Tomography and Reconstruction**

Publication No. _____

Henry Fredrick Schreiner III, Ph.D.
The University of Texas at Austin, 2016

Supervisor: Roy Schwitters

This dissertation investigates imaging with cosmic ray muons using scintillator-based portable particle detectors, and covers a variety of the elements required for the detectors to operate and take data, from the detector internal communications and software algorithms to a measurement to allow accurate predictions of the attenuation of physical targets.

A discussion of the tracking process for the three layer helical design developed at UT Austin is presented, with details of the data acquisition system, and the highly efficient data format. Upgrades to this system provide a stable system for taking images in harsh or inaccessible environments, such as in a remote jungle in Belize. A Geant4 Monte Carlo simulation was used to develop our understanding of the efficiency of the system, as well as to make predictions for a variety of different targets.

The projection process is discussed, with a high-speed algorithm for sweeping a plane through data in near real time, to be used in applications requiring a search through space for target discovery. Several other projections and a foundation of high fidelity 3D reconstructions are covered. A variable binning scheme for rapidly varying statistics over portions of an image plane is also presented and used.

A discrepancy in our predictions and the observed attenuation through smaller targets is shown, and it is resolved with a new measurement of low energy spectrum, using a specially designed enclosure to make a series of measurements underwater. This provides a better basis for understanding the images of small amounts of materials, such as for thin cover materials.

# Contents

# List of Figures

# List of Tables

# List of Listings

# Chapter One: Introduction

## 1.1 History of Muon Tomography

The idea of using cosmic ray muons to provide information about the composition of material is not a new one. In 1955, George [1] measured the overburden of a tunnel in Australia, comparing the flux of muons at the surface to the flux underground. Muons are abundant at sea level, with a spectrum of different energies. Muons lose energy as they pass through material, causing the lower energy muons to attenuate, reducing the flux as a function of the thickness of the material. Muons also undergo multiple-Coulomb scattering, causing them to change direction slightly when passing through a material. The natural occurrence and convenient attenuation length in materials make muons an attractive method for imaging structures and other targets of up to a few hundred meters of rock or similar material.

The first major imaging project was performed by Alvarez *et al.* [2], in the late 1960's, when he imaged the interior of the second pyramid at Giza from the Belzoni Chamber. The object of the study was to find undiscovered chambers that might have been built into the pyramid. Although no significant archaeological discovery was made, the process was able to correctly identify the corners of the pyramid, as well as the limestone cap on top of the pyramid. The process was quite involved, and used an immovable iron filled detector and lengthy numerical analysis techniques on the computers of that time [3]. The Alvarez group established the feasibility of muon tomography by observing the meter-scale limestone cap on the outside of the pyramid. Their principal scientific discovery was definitive, but negative: there are no additional chambers inside Chephren's Second Pyramid.

Despite the technical success of the method, the impracticality of the detection system limited further experiments with that technology. Developments in technology pertaining to methods of particle detection and analysis during the intervening years have made muon tomography a viable tool for surveying large structures with reasonably compact detectors, such as those described here.

### 1.1.1 Attenuation Based Tomography

The process used by Alvarez *et al.*, as well as this experiment, uses attenuation-based tomography.[1] The basic idea behind attenuation-based muon tomography is to measure the rates of cosmic-ray muons detected underground at diverse angles and locations. Much like an x-ray image, differences in the numbers of muons detected along particular directions and at different locations indicate differences in the total mass of material between the detector and the open sky in the direction being studied. These differences can be assembled using methods of computer-assisted tomography (CT) into a 3D image of the overburden.

In the mid 1990's, Nagamine *et al.* used muon tomography with near horizontal muons to image two volcanoes in Japan, Mt. Tsukuba [4] and Mt. Asama [5]. The project successfully created images of the targets, resolving the twin peaks of Mt. Tsukuba. They took advantage of these higher momentum muons in the 300 mrad to 200 mrad from horizontal to receive counts in the interior through more than a kilometer of rock. The system originally used an analog measurement system with three plastic scintillator planes, using timing differences between photomultiplier tubes on each of the four corners of the planes to determine location, but moved to a segmented system in 2003 [6] made of strips. Work has continued over similar geologic applications of similar detectors, called "muon telescopes". The study of this method on volcanoes expanded to Europe in 2008 with the DIAPHANE and MURAY projects [7]. Another project at the University of Texas at Austin is also building muon telescopes using similar equipment to ours [8].

In the early 2000s, the MayaMuon project was conceived at the University of Texas to develop portable Muon detectors and use them to image the interiors of sealed Mayan pyramids in Belize, Central America. After several iterations of the design that was described in Schwitters [9] in 2004, two detectors were taken down to Belize in 2013 and have been taking the first images of the interior structure of the pyramids. These detectors have a variety of possible applications, which will be explored in detail.

Other uses proposed have included monitoring tunnels for border control and safety [10] and monitoring underground CO2 storage [11] using bore-hole detectors [12]. A company was founded in Vancouver, Canada, called CRM GeoTomography

[1] Also called absorption tomography

Technologies, Inc., with the intent of using muon tomography for mineral exploration [13].

### 1.1.2 Scattering Based Tomography

Another method of muon tomography, only discussed briefly here, is scattering-based tomography. In this form of muon tomography, a muon's trajectory is measured both upon entering and leaving a target area. The inventing material will cause multiple-Coulomb scattering, giving the muon a slightly different track in the second detector. The density and placement of material can thus be reconstructed based on the degree of scattering observed. This method allows for high precision detection of high-$Z$ targets, and is not affected by scattering outside the target area, but requires two detection systems that must completely cover all potential trajectories being investigated. It also requires at least one of the systems must be able to measure the muon direction with sufficient precision to identify a change in trajectory within the target material. The two systems must also be synchronized to sufficient time resolution to identify matching tracks. The size and complexity of this system makes it completely impractical for most of the suggested uses we are interested for attenuation-based detectors. The detectors also detect and can use attenuation information directly, since a track that only occurs in the upper detector can be analyzed, as well.

This method was suggested with a proof of concept in 2003 by Borozdin *et al.* [14] and further developed for applications by Morris *et al.* [15] at Los Alamos National Labs (LANL) as a method for investigating high density targets, such as searching trucks in a noninvasive manner for border security [16]. The methods used for reconstruction, Point of Closest Approach (PCA) and Maximum Likelihood Scattering (MLS), have seen use in other experiments, such as the creatively named CREAM TEA (Cosmic Ray Extensive Area Mapping for Terrorism Evasion Applications) developed at the University College of London [17].

The Cosmic Ray Imaging and Passive muon Tomography (CRIPT) system by Armitage *et al.* [18] includes a muon spectrometer after the final muon tracker, giving a measurement of muon momentum, to allow faster and more accurate measurements of the density of the target. This system adds two 10 cm steel plates to make this measurement. It is intended, like the experiments before it, primarily for monitoring for high $Z$ materials hidden in cargo.

Other uses have been proposed and demonstrated, including corrosion and degradation in the power industry [19] and imaging of nuclear reactors [20], including investigating the recent Fukushima reactor meltdown [21]. Another proposed use for these methods is for the investigation of the walls on old structures, such as dome of the cathedral of Santa Maria del Fiore. There is a mystery surrounding its construction in 1420; it was the largest dome constructed at the time and it was not built with a supporting structure. A common theory is that large iron chains were used inside the structure, and a large quantity of iron was known to be purchased during the construction, no conclusive evidence has yet been found. Scattering based tomography could be used to search for these chains, as well as measure the depth of cracks in the dome [22].

Most of the attenuation based detectors and some of the scattering based detectors use plastic scintillator, including ours, due to it's cost effectiveness, durability, and portability. There are a few exceptions, such LANL's use of drift tubes, or the proposal to use gas detectors in Reference [23].

## 1.2 Uses of the UT Muon Tomography System

Muons used in muon tomography systems, such as ours, are naturally occurring, so no extra radiation is introduced when making a measurement. In fact, we do not have any other practical source of muons for imaging immovable targets; an accelerator is required to produce an artificial beam of muons (though such a beam of muons can be used for imaging portable targets [24]). The non-invasive nature of this allows muon tomography to be used in a wide variety of archaeological and civil applications.

We have designed our detectors to be portable with the intention of operation in remote areas. The current design is small enough for a single detector to be easily carried by four people, takes about 70 W to power continuously, and has been shown to be able to operate without human intervention for months at a time. There are currently four working detectors, and each detector has produced at least two years of data in various locations.

The goal of this project has been to investigate sealed structures with archaeological significance. The design parameters of our detector were tuned with the dimensions and operating conditions of a pyramid in a Belizean jungle in mind. Ini-

Figure 1.1: A detector in the jungles of Belize, imaging a pyramid.

tial results from the work in Belize will be presented here over such a situation.

Other uses with our design have also been pursued. The detectors can be placed underground, and then they can detect nearby tunnels, with a detection rate relative to the angle from the zenith. We have successfully used our detectors in this manner, discovering static tunnels in less than two days. The detectors could also be used for underground change detection, to monitor the ground surrounding critical installations. This has applications in border control, archeology, and in civil sectors.

There are geologic applications too: the detector can fit into a commercial 24 inch outer-diameter pipe, allowing use in bore holes or an underwater enclosure. Both of these were used in the course of this project, and examples of the data collected will be shown in this work.

Our detectors are designed to have an angular resolution idea for imaging meter scale structures at 20 to 40 m, giving them less directional resolving power than the muon telescope projects, but they are sensitive to almost any direction in the upper hemisphere, except for muons passing through the ends of the cylinder. This gives them a wider field of view than almost all the other attenuation based detectors. They do not have a method to measure the momentum of the muons being tracked, which is a feature primarily relegated to the immobile scattering detectors, due to the extra weight and complexity that such a system requires. Our detectors can be moved as a complete enclosed package, and are resistant to harsh conditions, such as sand and weather.

## 1.3 Difficulty in Imaging

Initial runs with our detectors have provided excellent images for targets ranging a few centimeters to tens of meters thick; the resolution and contrast of our detectors has met or exceeded expectations. One of the remarkable properties of an attenuation based measurement (see Equation 2.12) is that many of the details of the detector performance, such variations in efficiency in the strips and minor geometrical aberrations, are effectively canceled out by the use of a "flat-field", a run without a target present.

One of the primary issues that was discovered during the course of this project was that attenuation measurements of targets with less than 1 GeV of attenuation show significantly more attenuation than expected from simplistic attenuation calculations. Even using a Geant4 Monte Carlo simulation with multiple scattering, the discrepancy in the absorbed flux from the muon spectrum persisted. This is an excellent issue to have, since this meant our images were even better than predicted, but still indicated a lack of knowledge, and made absolute predictions about the depth and composition of the targets from the images collected impossible for these smaller targets. This discrepancy, as you will see, stems from two separate issues. Our detectors are significantly more sensitive to the low momentum portion of the spectrum than previously thought. I will be presenting a thorough Monte Carlo simulation that predicts a minimum value to trigger our detector under 125 MeV/c. The second issue is from a poor model of the low momentum portion of the spectrum; under 1.2 GeV we are seeing significant departure from common models. I will be presenting a measurement of the low momentum spectrum made with our detectors, mapping out the spectrum at a wide range of angles from 200 MeV to several GeV, overlapping the commonly measured $> 1$ GeV portion of the spectrum.

# Chapter Two: Muons and Detection

## 2.1 Cosmic Rays

Primary cosmic rays are made of nucleons, primarily protons and helium nuclei, that originate outside our solar system. These particles collide with the upper atmosphere with an intensity of approximately

$$I_N(E) \approx 1.8 \times 10^4 \left(\frac{E}{1\,\mathrm{GeV}}\right)^{-\alpha} \frac{\text{nucleon}}{\mathrm{m}^2\ \mathrm{s\ sr\ GeV}}, \tag{2.1}$$

where $E$ is the energy per nucleon, and $\alpha$ is the differential spectral index [25]. To a large degree, the cosmic ray primary spectrum is isotropic.

The interactions of primary cosmic rays with the upper atmosphere produce mesons. From neutral mesons, we get photons and electrons, which are quickly absorbed. From the charged mesons, we get muons and neutrinos. The muon is the most abundant charged cosmic ray particle at the surface.

For most energies, the muon distribution can be extrapolated to the earth's surface to give:

$$\frac{dN_\mu}{dE_\mu d\Omega} \approx \frac{0.14 E_\mu^{-2.7}}{\mathrm{cm}^2\ \mathrm{s\ sr\ GeV}} \times \left(\frac{1}{1 + \frac{1.1 E_\mu \cos\theta}{115\ \mathrm{GeV}}} + \frac{0.054}{1 + \frac{1.1 E_\mu \cos\theta}{850\ \mathrm{GeV}}}\right), \tag{2.2}$$

where the two terms represent the contributions from pions and charged kaons, as given by Gaisser [26]. This equation neglects higher order terms from charm and heavier flavors, due to the minimal contribution except at higher energies. This is only valid for $E_\mu > 100/\cos\theta\,\mathrm{GeV}$ and $\theta < 70°$, which is well outside of our area of interest.

At the earth's surface, the vertical flux of muons is approximately $1\,\mathrm{min}^{-1}\ \mathrm{cm}^{-2}\ \mathrm{sr}^{-1}$; cosmic ray muons form an appreciable fraction of the natural background of ionizing radiation at the earth's surface. Cosmic ray muons strike the earth's surface over a broad range of directions with a spectrum of energies. They lose about 2 GeV traveling through the atmosphere and have an average energy of 4 GeV at sea level [25], with a higher average for larger zenith angles from vertical [27].

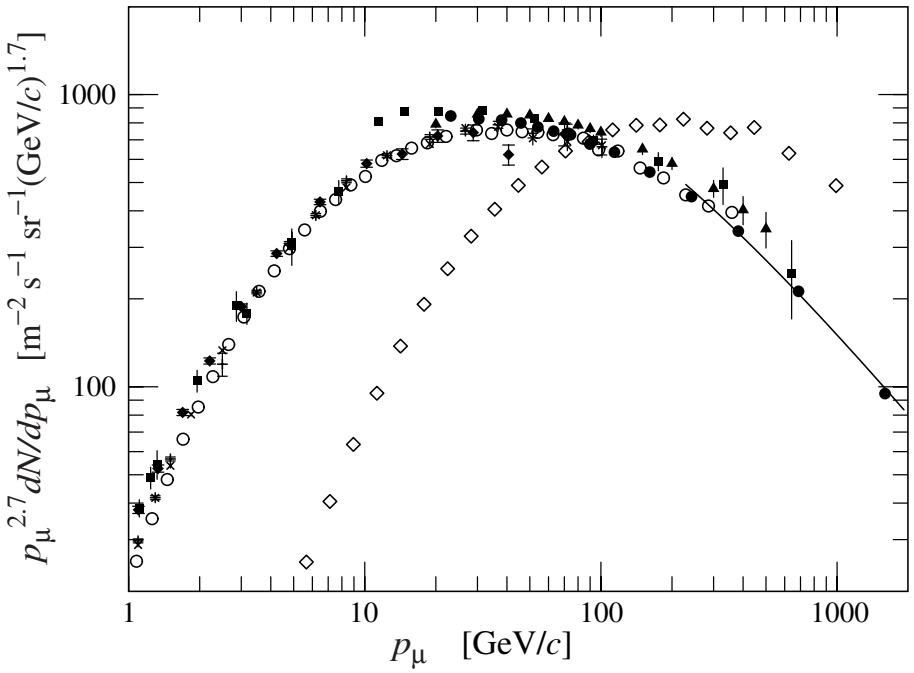


Figure 2.1: Spectrum of muons at the surface, taken from the PDG collaboration [25]. The ◇ points indicate the spectrum at 75°. The line is the PDG fit, discussed in Section 2.2.1.

## 2.2 Muon Spectrum and Rates

There currently are several different models for the cosmic ray flux. We are primarily interested in the the flux under 10 GeV, since the targets we are proposing this method for are in this range. The conventional definition of the flux is rate $\dot{N}_\mu$ of muons crossing an element of area $dA$ perpendicular to the muon direction per unit solid angle $d\Omega$:

$$\Phi_\mu = \frac{d^2\dot{N}}{dA\, d\Omega}. \tag{2.3}$$

The units of the flux are generally m$^{-2}$ s$^{-1}$ sr$^{-1}$.

### 2.2.1 PDG Model

The Particle Data Group [25] describes the muon spectrum in fairly general terms. The mean energy at the ground is about 4 GeV, the spectrum is proportional to

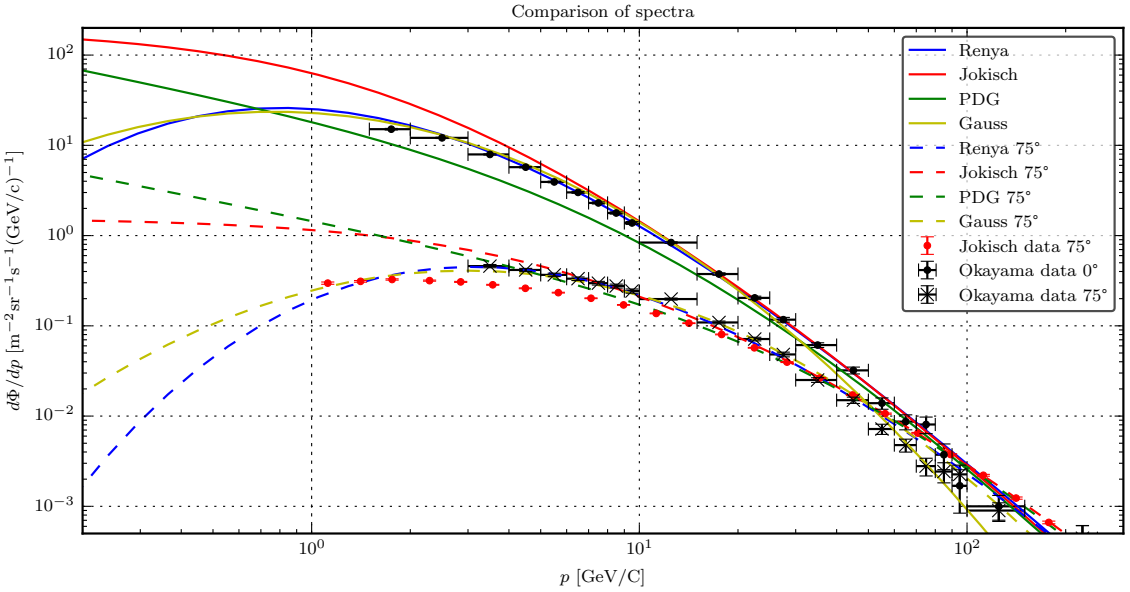


Figure 2.2: The models of the differential spectra discussed are plotted here for comparison. The Jokisch model provides the highest rates at low values of $p$. Data are from Jokisch *et al.* [28] and the OKAYAMA telescope, Wada *et al.* [29]. The unmodified log Gaussian spectrum from Section 6.1.1 is included for comparison. Both vertical and 75° are shown.

$\cos^2\theta$, and is generally flat for $E < 1\,\text{GeV}$. For mid range energies, they give Gaisser's equation, given above as Equation 2.2.

An ansatz to this spectrum [30] to give it reasonable behavior in low momentum is to give it the following modified form:

$$\frac{d\Phi_\mu}{dp_\mu} = \frac{0.14 p_\mu^{-2.7}}{\text{cm}^2\,\text{s}\,\text{sr}\,\text{GeV}} \times \left( \frac{1}{1 + \frac{1.1\zeta}{115\,\text{GeV}}} + \frac{0.054}{1 + \frac{1.1\zeta}{850\,\text{GeV}}} \right) \left( \frac{\zeta}{\zeta + 8\,\text{GeV/c}} \right)^2, \tag{2.4}$$

where we are making the useful substitution $\zeta = p_\mu \cos\theta$. This substitution will become important in several other models.

### 2.2.2 Jokisch Model

It the late 1970s, Jokisch *et al.* [28], proposed the following spectrum for high angle (70°) muons:

$$\frac{d\Phi_\mu}{dp_\mu} = \frac{a}{p_\mu / \sec\theta + b} \left(5 p_\mu + c \sec\theta\right)^{-2.57} \times \frac{p_\mu + d}{p_\mu + d \sec\theta}, \tag{2.5}$$

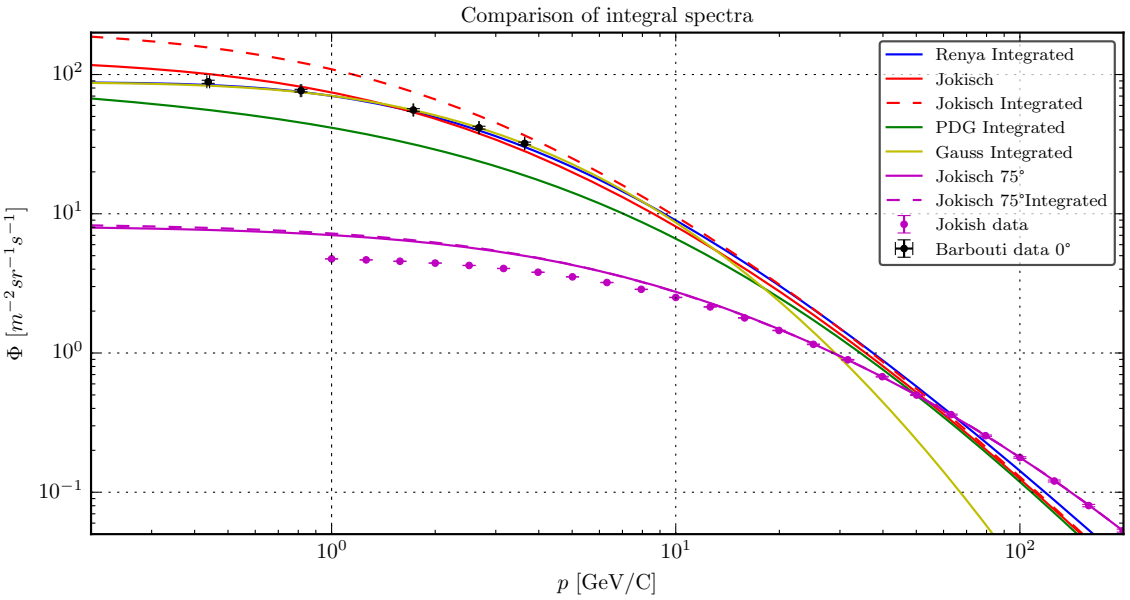


Figure 2.3: The integral models discussed are plotted here for comparison. Again, the Jokisch model provides the highest prediction for low $p$, but the difference is small. The PDG spectrum is particularly off, but this spectrum was not intended to be valid for low $p$, so this is expected. The integrated version of Jokisch's differential spectrum (- -) is similar to the fit that they made for high angles, such as the 75° measurement they based it on. Data are from Jokisch *et al.* [28] and Barbouti and Rastin [31].

where the parameters are $a = 51 \pm 15\,\mathrm{cm^{-1}sr^{-1}s^{-1}}$, $b = 77.2 \pm 4.8\,\mathrm{GeV/c}$, $c = 9.2 \pm 0.5$, and $d = 19.8\,\mathrm{GeV/c}$. This can be rewritten in the more modern form:

$$\frac{d\Phi_\mu}{dp_\mu} = j_1 \cos^{3.57}\theta \frac{(\zeta + j_2)^{-2.57}}{\zeta + j_3} \times \frac{p_\mu + j_4}{\zeta + j_4}, \tag{2.6}$$

where the parameters are $j_1 = 7.2 \times 10^4\,\mathrm{m^{-2}\,s^{-1}\,sr^{-1}}$, $j_2 = 1.84\,\mathrm{GeV/c}$, $j_3 = 77.2\,\mathrm{GeV/c}$, and $j_4 = 19.8\,\mathrm{GeV/c}$.

Jokisch made a separate fit to the integral spectrum, so will be used instead of deriving such a spectrum from the one listed above. Using the modern notation again, and with the lower bound of the integration over the spectrum written as $p$, we arrive at:

$$\Phi_j = j_5 \cos^{2.57}\theta \frac{(\zeta + j_6)^{-1.57}}{\zeta + j_7} \times \frac{p + 3j_8}{\zeta + j_8\,(2\cos + 1)}. \tag{2.7}$$

### 2.2.3 Reyna Model

One of the more popular descriptions of the spectrum today is that of Reyna [32], who made observation that greatly simplified the form of the model. He suggested there was a vertical spectrum, and that the angular spectrum only depended on the vertical spectrum as:

$$\frac{d\Phi_\mu}{dp_\mu} = \cos^3\theta\, I_V\left(\zeta\right), \tag{2.8}$$

where the vertical differential muon flux $I_V$ is evaluated at $\zeta$. He combined this with a phenomenological parametrization from Bugaev *et al.* [33], and fit a large collection of data from different angular measurements, to obtain:

$$I_V\left(p_\mu\right) = c_1\, p_\mu^{-\sum_{i=2}^{5} c_i \log_{10}^{i-2}(p_\mu)}. \tag{2.9}$$

The values of the coefficients that he found are given in Table 2.1.

| Coefficient | Reyna's value | Bugaev Value | Units |
|---|---|---|---|
| $c_1$ | 25.3 | 29.50 | $\mathrm{m}^{-2}\ \mathrm{s}^{-1}\ \mathrm{sr}^{-1}\ (\mathrm{GeV/c})^{-1}$ |
| $c_2$ | 0.2455 | 0.3040 | |
| $c_3$ | 1.288 | 1.2743 | |
| $c_4$ | -0.2555 | -.2630 | |
| $c_5$ | 0.0209 | 0.0252 | |

Table 2.1: Reyna [32] and Bugaev *et al.* [33] coefficients. The spectrum proposed by Bugaev *et al.* was intended to be valid in the range $1 - 928\,\mathrm{GeV}$.

A log normal approximation to this spectrum is derived in Chapter 6 for effective Monte Carlo generation.

### 2.2.4 Comparison

These models were all designed to be used for cosmic rays with a momentum of at least $1\,\mathrm{GeV/c}$; all the models behave differently in the low momentum portion of the spectrum we are interested in. For this lowest portion of the spectrum, several factors are beginning to take effect, changing the physics of the spectrum and making a single equation model difficult.[1] The differential spectra are plotted in Figure 2.2.

[1]The same holds true for the high energy spectrum, where pions begin to interaction with the atmosphere and energy loss via other processes becomes important.

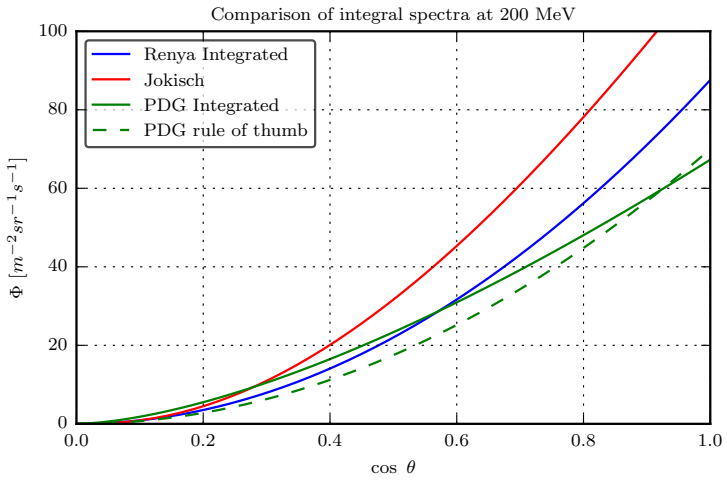


Figure 2.4: The differing behaviors of the models in $\theta$ are illustrated here. The PDG rule of thumb of $70\cos\theta$ (- -) is here as a baseline for comparison. The Gauss model has the same behavior as the integrated Reyna spectrum.

The integral spectra are plotted in 2.3. The differing behaviors vs. $\cos\theta$ are plotted in Figure 2.4. The models behave in a similar fashion for higher energies. A slight divergence is observed for lower energies. The reduced data available over these lower energies leave them not as well defined.

## 2.3 Attenuation in Materials

To be detected, muons moving toward the detector must have energies at the surface sufficient to penetrate the intervening material. When muons pass through matter, the dominant interaction is ionization of atoms along the path which results in a loss of energy of the muon in direct proportion to the mass of material traversed. Thus, paths with more total material between the surface and the detector require higher energy muons at the surface and, therefore, will have smaller yields for a given exposure time. The distribution of muon energies and directions at the earth's surface is known from experiments; representative data are displayed in Figure 2.1. The units of energy (or momentum) displayed in the figure are GeV; for reference, a high-energy muon loses, on average, about 1 GeV in passing through 5 meters of water or 2 meters of rock.

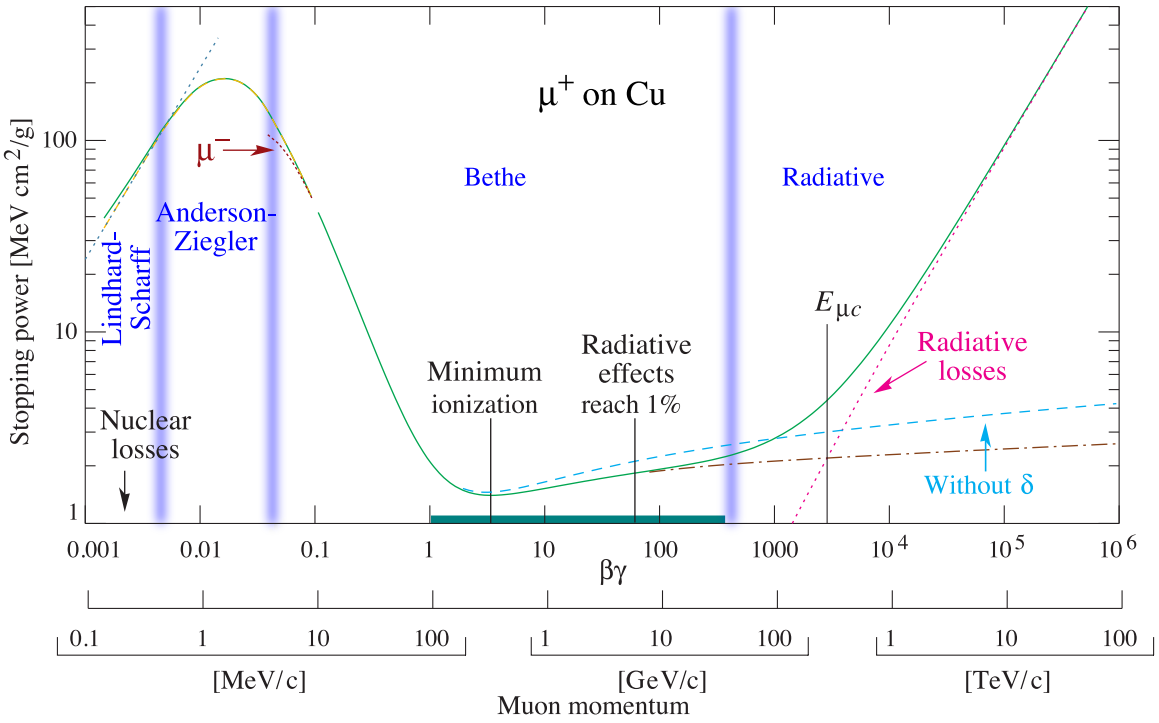


Figure 2.5: Muon energy loss in Cu, primarily from the Bethe equation, as a function of muon momentum. The highlighted range at the bottom of the graph shows the region of interest in this study. In this region, the energy loss is nearly constant, and is close to the minimum ionization momentum. Figure taken from Groom and Klein [34].

The energy loss of a muon through material in the range we are sensitive to, 100 MeV to 30 GeV, is primarily through ionization and is well described by the Bethe equation[2] [34]:

$$-\left\langle \frac{dE}{dx} \right\rangle = Kz^2 \frac{Z}{A} \frac{1}{\beta^2} \left[ \frac{1}{2} \ln \left( \frac{2m_e c^2 \beta^2 \gamma^2}{I^2} \right) - \beta^2 - \frac{\delta(\beta\gamma)}{2} \right], \tag{2.10}$$

where $m_e$ is the electron mass, $Z/A$ is the atomic number over the atomic mass of the absorber, $\delta(\beta\gamma)$ is the density effect correction for the ionization at high energies, $I$ is the mean excitation energy, and $K$ is a constant for an electron density,

[2]Before 2010, The PDG called this equation the Bethe-Bloch equation, causing some controversy since the corrections have several terms, the Bloch one would be the smallest. The name Bethe-Barkas-Andersen-Bloch would correctly order the contributions by importance.

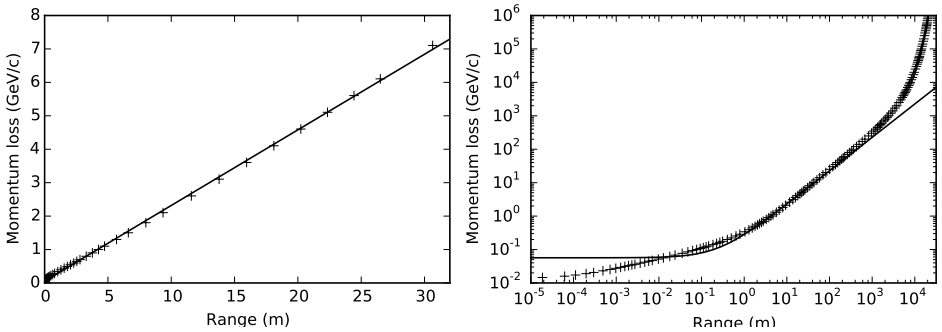


Figure 2.6: Muon range $R$ in water. The fit $0.2262R+0.0567$ is shown for comparison. Log-log scale on the right. Data for figure taken from Olive [25].

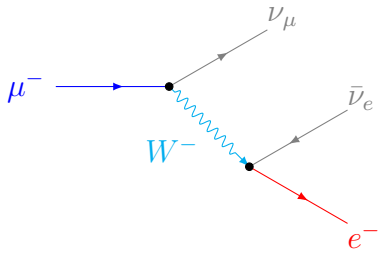


Figure 2.7: Example of a $\mu^-$ decay into muon neutrino, electron anti-neutrino, and electron. The neutrinos are not detected by our scintillator strips, and the electron is quickly absorbed and does not penetrate the detector.

$0.307075\,\mathrm{MeV\,cm^2\,mol^{-1}}$. The other means of energy loss, Bremstraulgin and pair production, are not significant at these energy levels [35].

The stopping power of an electron in copper are shown in Figure 2.5. The stopping power is nearly constant throughout the range we are interested in for muon tomography.

A more useful combination of these methods is the range, the distance which muons will travel through a material given an initial energy. Using tabulations provided by the Particle Data Group Olive [25], the range for muons in water is shown in Figure 2.6, along with the simple fit $0.2262R + 0.0567$, which provides the useful relation of $p/R \approx 0.2262\,\mathrm{GeV\ c^{-1}\ m^{-1}}$ in water. This relationship is useful for converting the depth of the detector in water to an approximate momentum loss.

As a muon loses energy and approaches a non-relativistic momentum, the muon

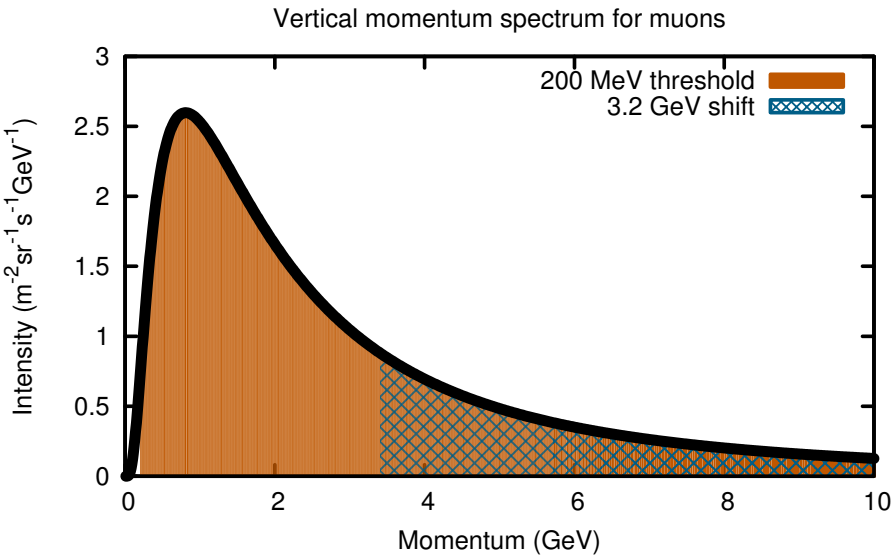


Figure 2.8: Spectrum with and without a target, showing attenuation. The spectrum shown is the vertical Reyna spectrum. The shaded regions represent the integral flux. The threshold before the target is introduced is 200 MeV; when the target is present it shifts the threshold as shone in the second shaded region.

will quickly decay in flight, such as seen in Figure 2.3, and will no longer be tracked by our detector. This means that the detected flux:

$$\Phi = \int_{p_{\min}}^{\infty} \frac{d\Phi}{dp_\mu} dp_\mu \tag{2.11}$$

will change as $p_{\min} \to p_{\min} + p_{\text{loss}}$, where $p_{\text{loss}}$ is the momentum lost in the intervening material. This can be described as an effective threshold momentum that is based on the attenuation in the material. An example is shown in Figure 2.3. The area under the curve without a target is $\Phi_{\text{b}}$, and with a target is $\Phi_{\text{d}}$; the attenuation is then:

$$D_\mu \equiv -\ln\left(\frac{\Phi_{\text{d}}}{\Phi_{\text{b}}}\right). \tag{2.12}$$

Muons also scatter from the nuclei in the material through Coulomb interactions. The change in direction from the deflection of muons through multiple-Coulomb scattering becomes larger as the muons lose energy; this effect is most prominent at the muons are close to decay. More details of multiple-Coulomb scattering are presented in Section 4.4.5.

The most important feature of the attenuation is that as material is added, it always increases (except for minor higher order scattering corrections and statistical fluctuations). An accurate knowledge of the spectrum and the detection threshold for our detector allows the two integrals in Equation 2.12, given in Equation 2.11, to be evaluated to relate $D_\mu$ to $p_{\text{loss}}$. This can be used to find the density of targets given the thickness if it is known, either *a priori* or using information from spatially separated tracks[3] to measure from the collected data.

A variety of attenuation measurements will be shown and discussed in Chapter 8, and a measurement of the spectrum using our detector and the reconstruction and efficiency discussions in the next few chapters will begin in Chapter 9. A new spectrum description that improves our description of muons with $p < 1.2\,\text{GeV/c}$, suitable for imaging small targets with our detectors, will be presented.

[3]Gathering information about the depth of a target from multiple points, either from separate detector locations for distant targets or from the field information from the spacial extent of the detector, for targets within a few meters of the detector, is often called "stereo" information, although it is usually from more than just two points.

# Chapter Three: A Unique Detector Design

The MayaMuon group at the University of Texas at Austin has developed a unique cylindrical detector design, with two helical and one axial layer of scintillator strips. This design was based on the MINOS near detector [36], and was originally proposed in the note [9], and has gone through several iterations.

The first design contained most of the components present in the current cylindrical design, but was three times bigger [9], [37], [38]. The primary reason for the size was twofold; the size provided a nine times faster track rate over the current design, and had the potential for the addition of a Cherenkov system in the interior to monitor the muon energy using Cherenkov radiation, in order to allow a larger cut on the minimum detectable energy. A smaller detector does not have enough space to pick up the required number of photons for such a detection system. The cylinder of "Detector I" was 1.55 m in diameter, 4.22 m in length, and weighed a metric ton, making it impractical for many applications that a portable detector could be used for. The loss of track rate in a smaller design can be accounted for by simply allowing more time for the imaging process. The lower threshold increases our sensitivity to soft muons, muons with high levels of scattering. This, however, does not negatively impact our ability to make images of targets, in fact there appears to be a general enhancement to the contrast from thin targets (see Chapter 8).

Two more detectors, with a design similar to the one that is described here, were created after that detector was constructed. These two detectors were called "A" and "B".

The final design was used for the construction of four detectors from 2009 to 2011, "1", "2", "3", and "4", and will be the basis for future detectors [39]. In 2010, the first complete working reconstruction software system was implemented, allowing the detectors to begin operation. A simplified diagram indicating the principal design is given in Figure 3.2. Descriptions of the technologies chosen for the detector components follow.


Figure 3.1: H. Adam Stevens (left) is helping place our first prototype detector in the shaft constructed for it. Our first imaging studies were made in the vertical orientation, however both horizontal and vertical orientation were used once we made the one-third scale final design.

## 3.1 Physical Design

The tracking system comprises ionization/location detectors (scintillator strips) and the means to convert ionization signals to data appropriate for computer analysis (WLS fibers, photomultipliers and front-end electronics). The tracking system is used to indicate when a muon hits the detector and it provides the measurement of the muon track position and direction. The muon tracking system is based on detector technology developed for the MINOS experiment at Fermilab [36].

Briefly, we use strips of doped polystyrene scintillator to detect and locate charged particles. Scintillation light emitted by the scintillator when ionizing tracks pass through is absorbed in a wavelength-shifting (WLS) optical fiber located in a groove extruded along a face of the scintillator strips. The WLS fiber will re-emit the absorbed scintillator light at a slightly different wavelength; this light is transmitted

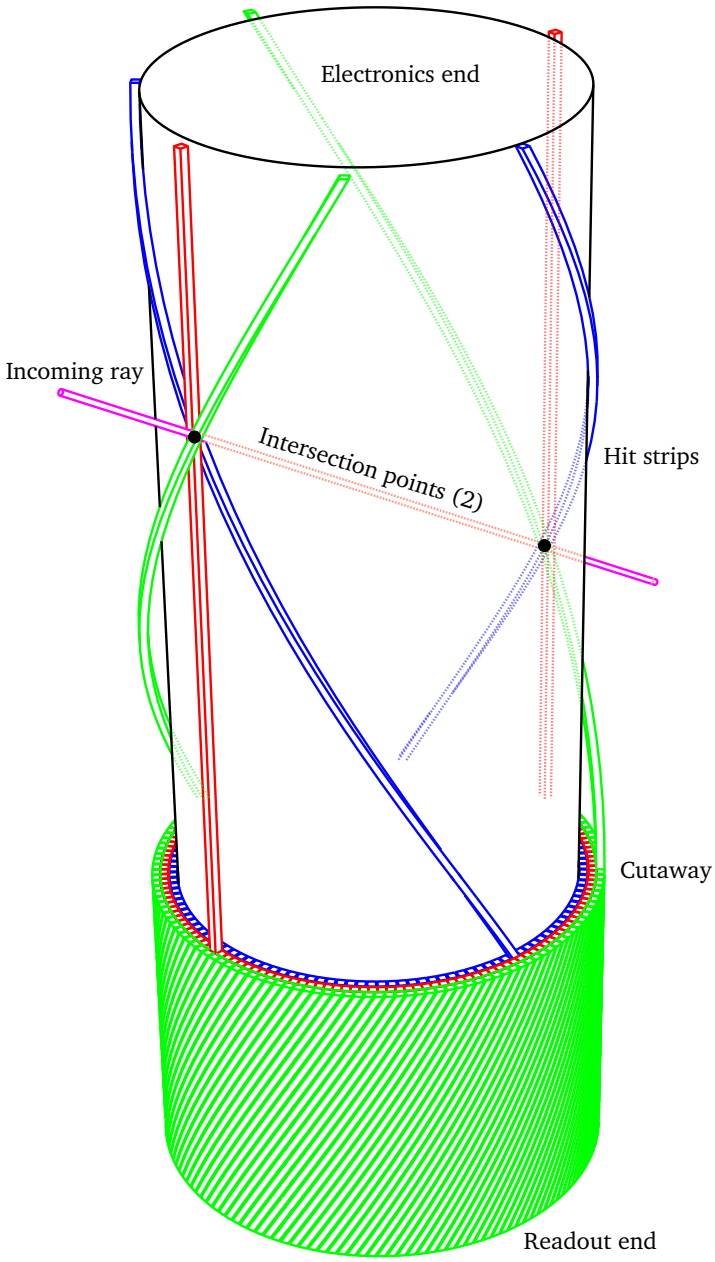


Figure 3.2: Cylindrical design of the detector. The detector is made of three layers of strips; the first layer (blue) is helical, with a total wrap angle less that one-half way around the cylinder. The second layer (red) is axial. The third layer (green) is helical, with opposite helicity compared to the first. Sets of strips are hit by an incoming cosmic ray muon and trigger in a unique pattern. In this figure, the strips that were not hit by the incoming muon (magenta) are cut away from the upper portion of the detector to illustrate the hit pattern.

down the fiber with relatively low loss to photomultiplier tubes (PMTs). Electrical signals from the photomultipliers provide information on the timing of the track passing through the scintillator strip; the particular fiber/strip hit indicates location. Scintillator strip/WLS fiber technology was chosen for the Maya project because it is simple, robust, efficient, well understood by the MINOS group and relatively inexpensive.

We use extruded polystyrene strips doped with 1.0% PPO and 0.3% POPOP scintillator dyes. They are $10^{+.0}_{-1.0}$ mm square with a $1.8 \pm 0.2$ mm diameter hole in the center. The measurements include an opaque, white $0.25 \pm 0.13$ mm polystyrene with 12% titanium dioxide cladding. A 1.2 mm diameter WLS fiber, viewed on the positive end by multi-anode photomultipliers senses the ionization signals. The strips are arranged in three adjacent layers on a 0.2465 m diameter, 1.372 m long cylindrical surface. On the outer and inner layers, the strips form helices of pitch angle $\pm 30°$ relative to the axis; on the middle layer strips are oriented parallel to the detector axis. The stereo layers make one-half wrap around the cylinder from one end to the other, thereby incurring no small-angle-stereo ambiguities in track reconstruction. Each detector has a total of 448 strips and associated WLS fibers which are read out on each end by Hamamatsu M64 multi-anode photomultiplier tubes[1]. These PMTs have been characterized for the MINOS experiment, and have been found to exhibit uniform efficiency across all channels, to within 10%, and are sensitive to the levels photoelectrons expected from the scintillator strips [40].

## 3.2 Brief Construction Details

The detector is built around a hollow cylindrical aluminum base. End plates are affixed to the ends of the cylinder to support the structure and assist with the wrapping process. The interior of the cylinder is painted black to absorb photons.

Special tooling was created for the construction of the current detectors. The wrapping process can be done mechanically without heat, but requires controlled positioning and clamping of the strips. This device holds the detector horizontally and has a foot-pedal to control the rotation through a small motor. The fiducial strip, strip 0 of the inner layer, is attached to the can on either end at measured locations

[1]Hamamatsu H7546B, `https://www.hamamatsu.com/resources/pdf/etd/H7546A_H7546B_TPMH1240E.pdf`

Figure 3.3: John McGill is using the tooling to wrap the first helical layer on Detector 1.

using a small hole and a pin. Small metal clips are used at either end to hold the strips in place. Using a piece of mylar with the correct rotation, the strip is then taped to a helical path. Further strips are applied with a 0.1 mm shim to ensure even coverage. The strips are bent with a custom hand-held clamp. Minor adjustments after the layer is applied are made to ensure even spacing between strips and true helical shape.

Between layers, tape is applied in five bands to keep the strips in position. The middle layer does not require wrapping, but spacing is still important. The final layer is wrapped in a manner similar to the first. The detector is then wrapped in kevlar twine and RTV[2], fixing the positions of the strips permanently, allowing the clamps to be removed and the ends to be cut flush to the correct length.

Wavelength-shifting fibers are then threaded down the holes in the strips. In the first two detectors, glue was added to create a uniform index of refraction (IOR) connection between the fibers and the strips. Upon further testing, the glue was deemed unnecessary and the detector performance without it was as good or marginally better, due to the unavoidable occurrence of air bubbles in the glue upon injection.

[2]Room temperature vulcanizing silicone.

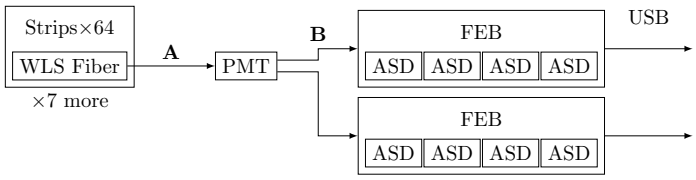


Figure 3.4: Block diagram of data flow. At connection A, light is transmitted through fibers, which are aligned to channels on the PMTs via plastic "cookies". At connection B, the analog signals from the PMTs are connected directly to breakout boards which are each connected via two ribbon cables to each FEB. This diagram is for one PMT, of which there are seven. A few of the channels on some FEBs are not connected, since there are slightly less than 448 strips on a detector.

Further details on the construction of the detector is available in Thurston [39].

## 3.3 Front-end Electronics

A muon passing through the cylindrical detector will normally hit three strips—called a "triplet"—on each side of the cylinder. Only two layers are needed to completely reconstruct hit locations; the third layer is used to filter noise, as an extra hit will not create any extra reconstructions. By knowing which six strips were hit, the azimuthal and longitudinal coordinates of the entry and exit points on the muon track can be reconstructed.

There is an up-down ambiguity in the direction of the muon which, in principle, can be resolved by a timing measurement. However, due to the relativistic nature of the muons, it is not possible to capture and use this information. Because the vast majority of muons will be downward-going, we will simply choose this solution when reconstructing the track direction. Custom front-end electronics from the ATLAS experiment [41] amplify, shape and discriminate (ASD) the PMT signals. The resulting digital signals are brought to field-programmable gate arrays (FPGA) from which the tracking information is combined to form a trigger indicating a muon has crossed the detector and, when triggered, read into a computer for subsequent analysis along with other detector information by the data acquisition system (DAQ). The front end boards (FEBs) have a 40 Mhz clock that is synchronized between the boards, and allows the hits to contain timing information. There is a small delay of 1-5 clock

| Content | Bits | Default | Notes |
|---|---|---|---|
| Chip mode | 1 | 1 | Turns on the board |
| Channel mode (8) | $2 \times 8$ | Active | Active, Low, or High |
| Dead time | 3 | 0 | |
| Wilkinson current | 3 | 0 | |
| Wilkinson integration | 4 | 0 | |
| Hysteresis | 4 | 0 | |
| Wilkinson threshold | 3 | 0 | |
| Main threshold | 8 | $t$ | Configurable value $t$ |
| Injection capasitor | 3 | 0 | |
| Channel mask (8) | $1 \times 8$ | 0 | 1 to mask out channel |

Table 3.1: ASD settings in packet. The most important value for our purposes is the main threshold $t$. Empty channels are not masked at this stage, due to low rates on those channels.

cycles as the synchronization signal is sent around the FEBs through an Ethernet loop connection. This was measured and is corrected for later in software.

The PMTs and FEBs are mounted at the readout end of the detector in order to minimize the lengths of WLS fibers and low-level electrical signal cables. The FEB boards are connected to an onboard computer through USB cables and hubs. The computer, hubs, and power supplies are mounted on a removable "tree" the other end of the detector, to reduce electronic interference.

Data from FEBs for the tracking system is pipe-lined through FPGAs to the onboard computer, where a software trigger is performed. USB cables and hubs are used to connect the FEBs to the computer. On the computer, a moving window of roughly four FEB clock cycles is used to look for events, where an event is six or more hits. This filters a significant portion of the dark noise [42] and partial hits. When an event is found, it goes through the reconstruction outlined in Section 4.2, and if a track can be reconstructed and passes a set of goodness of fit requirements, the track is placed in a four dimensional histogram. Small (roughly 10 second) samples of complete hit information are stored with each run to monitor the signal to noise ratio.

### 3.3.1 FPGA System

The ASDs are configured through a 53 bit binary signal [41] (see Figure 3.1) that sets thresholds and other options. The boards send data directly to the FEBs as part of the VHDL drivers on the FEBs. The configuration packet sent to the FEBs is made of four of these packets, as well as a run-stop bit that controls some aspects of the boards (depending on the firmware version, see below).

The FEBs have a custom firmware that is currently being revised. The old system is described first, followed by the one that I developed with Carlos Villarreal.

#### 3.3.1.1 Original System

Upon powering up through the digital power connection, the boards prepare a initialization packet, containing the FEB number read from the board's physical dip-switches. This packet is only created this one time, and it is the first packet that is sent when the computer requests a packet.

The boards are in a stop state when starting. When a configuration is sent, they read a run/stop bit, and if that is true, they start preparing packets. The rest of the configuration packet is sent directly to the four ASD boards. The first time a configuration packets is sent, the master board (the one that identifies as board 0) sends a timing signal down the ethernet clock cable to the other boards, causing all of them to start their internal clock synchronized to this signal. This has a known delay as it propagates, and that delay is included as a correction to the timestamps on reconstruction.

When the boards are in a run state, they monitor the incoming channels from the ASDs. Every time they get a hit, they fill in an event in the outgoing packet. An event consists of 32 binary bits that indicate the status of the four eight-channel ASDs. A 64-bit timestamp, consisting of 52 bits of data and a few bits mixed in for error checking purposes, is included with each event. The 512-byte packet contains 42 of these events, and is placed on the send queue when full. The send queue holds four packets and is overwritten if a new packet is ready when four packets already exist. Care must be taken to ensure the packets are not stale, from a previous run. Also, if the packets do not fill, there is nothing to send and the USB board communications simply waits until a packet is ready. Very quiet PMTs or the run-stop bit being off can both cause this.

This system has a couple of issues. One is the initial state of the boards changes after the first communication packet, making an initial read required in order to ascertain the board number. While the board number is in all packets, it does not get sent if a packet is not ready, and the number is placed in a different location in the packet. This ties the computer system state to the board state; restarting the computer without cycling the power on the FEBs, for example, will cause issues.

The other issue is that the boards will not communicate until they have a full packet; if the boards are in an "off" state, this will cause the board to hang and be declared dead by the system.

#### 3.3.1.2 New System

The new system creates only one type of packet, a data packet with a "signature" of 0. Future packet types or revisions to the packet style can be created with new signatures, coexisting with the current packets using the signature to signal the computer that the packet has different contents. The data packets have a design shown in Figure 3.5. The sizes of the data members were chosen to make reading into a C or Python based system easier and efficient. There is more information in this packet than in the classic system, and it can store a variable number of hits, and can contain more hits per packet.

Upon powering up through the digital power connection, the boards start preparing data packets at a constant rate. The rate is obtained from a special counter set up for this purpose, since the board clocks have not been initialized yet. These packets always have a time stamp of zero, since the internal clock is not yet synced.

Once the first configuration packet is sent to the boards, the boards initialize the clock. The master board (the one that identifies as board 0) sends a timing signal down the Ethernet clock cable to the other boards, causing all of them to start their internal clock synchronized to this signal. This has a known delay as it propagates, and that delay is included as a correction to the timestamps on reconstruction.

Boards then start producing packets based on the 17th bit of the timestamp. By choosing this point to send a packet, the packets only need to include the lower 32 bits of the timestamp, since a packet is sent before rollover occurs. Careful timing on the FEB ensures that the dead time of 4 clock cycles[3] to prepare a packet always

[3]The old packet system required 6 clock cycles

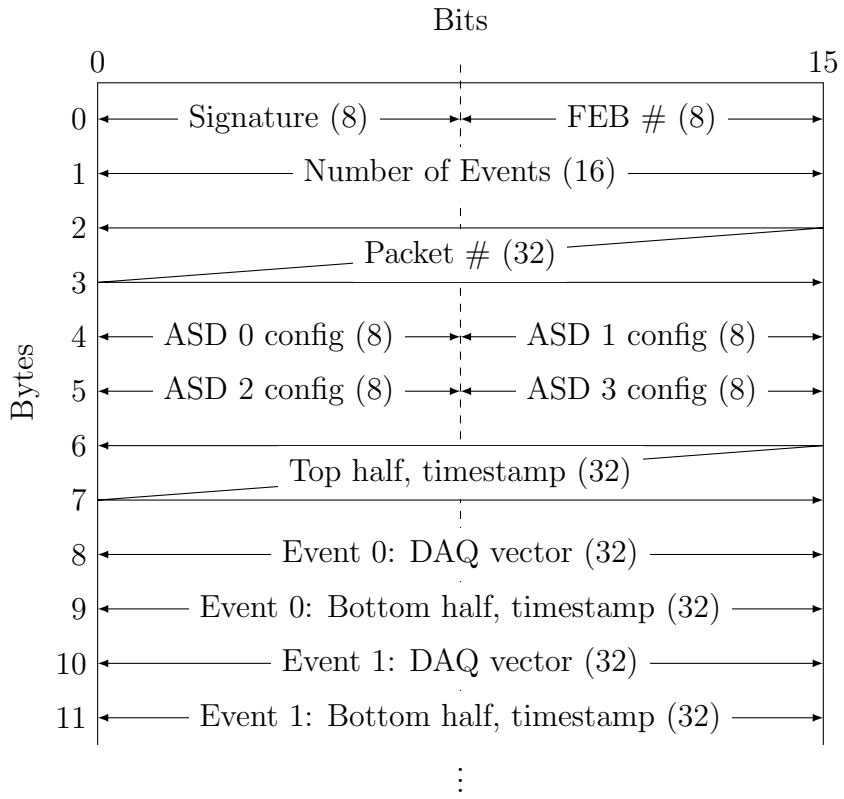


Figure 3.5: The bit layout of the new style packet, with packet signature 0. The number of bits are listed in parenthesis.

occurs at this point.

### 3.3.2 Software Packages

There are two packages that implement the tracking as described in the next chapter. The first package, MuLibrary, was used to collect most of the data up to this point. The main output is the histogram described above, as well as 1 MB (roughly 10 seconds) of unprocessed hit information. It used an older Intel Atom computer system, and internal memory. Written in a terrifying blend of C, C++, and goto statements, it had several problems, including being designed around a bug in the LibUSB package, a complex and inflexible data format, and a confusing clash of programming paradigms.

The current package is called UDAQ, and solves these issues in an elegant multi-

threaded C++11 solution. By using the open source HDF5 file format [43], details about the reconstruction are also collected and stored for each run, along with track rate, providing a more complete picture of the system. Data is compressed and periodically stored, providing a robust system under power failure. The system is powered by a Hummingboard ARM computer, with low power consumption and low heat output. The system has a backup battery pack for clean shutdown during power failure. With all FEBs active, the computer clocks under 15% load on its two cores.

# Chapter Four: Tracking

## 4.1 Details of Detector Geometry

The detector is made of three layers with radii $R_s$, where $s = -$, 0, + are three layers. These radii are measured to the center of the strip layer. The strips have a width $W$ and a thickness $T$. The detector has a length $L$ along the $z$ axis. The strips are described by a wrap angle $\Omega_i$, measured as $\Omega = \theta_b - \theta_t$, where $\theta_b$ is the angle of the center of the strip at the bottom of the strip active area, and $\theta_t$ is at the top. The angular width of each strip is listed for reference, though it can be calculated using $\Delta\phi_s = W/\left(LR_s\right)\sqrt{\Omega_s^2 R_s^2 + L^2}$.

The location of the strip $i$ in layer $s$, $\phi_{s,i}$, at the $z = 0$ plane of the detector can be written as $\phi_{s,i} = \phi_{s,0} + i \cdot \Delta\phi_s$. The locations in $\phi$ are usually written in modulo $2\pi$, and care must be taken in calculations that depend on continuous lines passing through the wrap around point.

The first two detectors had small variations in the parameters used in construction. After the first two, the parameters were standardized, so that the same parameter descriptions can be used for all recent detectors. These parameters are summarized in Table 4.1.

| Param | Value | | | Unit |
|---|---|---|---|---|
| | $s = -$ | $s = 0$ | $s = +$ | |
| $L$ | | 1.372 | | m |
| $W$ | | 1.00 | | cm |
| $T$ | | 1.00 | | cm |
| $n_s$ | 132 | 158 | 143 | |
| $R_s$ | 0.247 | 0.2582 | 0.2684 | m |
| $\Omega_s$ | -3.1914 | 0 | 2.9146 | rad |
| $\phi_{s,0}$ | 1.7656 | 0.0194 | 4.6707 | rad |
| $\Delta\phi_s$ | 0.0476 | 0.0397 | 0.0440 | rad |

Table 4.1: Parameters for the latest detectors.

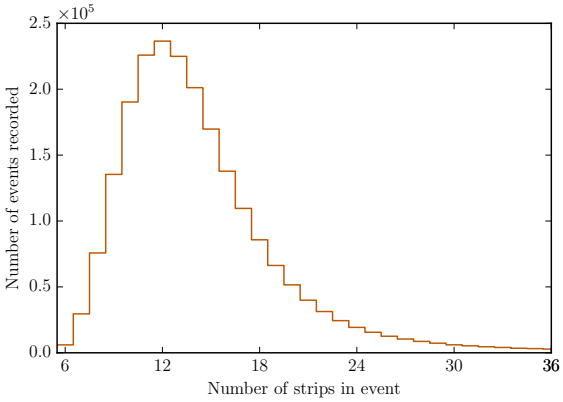


Figure 4.1: Hit multiplicity per event, for events with 6 or more hits, from a 21 hour run. There are almost always more than 6 strips involved in an event, with generally 14 or 15 strips involved.

## 4.2 Track Reconstruction

An event in the detector corresponds to a list of hit strips in a time window. Given a list of strips hit, each of the possible triplets (one strip each on the three layers) can be used to compute hit locations on the cylinder. Each of these triplets can be assigned a $\chi^2_t$, using the procedure defined below, to measure how well they come together to a single point. Once a set of valid triplets are found, passing a cut on $\chi^2_t$ are found, the triplets can be then taken in non-overlapping pairs and corrected for the physical thickness of each layer to find the best (minimal combined and corrected $\chi^2$) track. This is then a valid track if the value of $\chi^2$ is below a predefined threshold. This procedure is described in more detail below, and is based on the procedure developed by Schwitters [44].

The detector almost always has more than six hit strips in an event, from the physical width of the strips, cross-talk between PMT channels, and noise. The minimal $\chi^2$ reconstruction and the redundancy between the strip layers provides an effective filter for these extra hits. This will be shown in detail in Section 4.6.

The three sets of strips are on three separate concentric cylinders, each with a slightly different radius. The radius of the three cylinders can be approximated by the radius of the mid cylinder, $R = R_0$, a correction will be made later to undo this approximation. Once all the strips are on a single cylinder, triplets form intersections

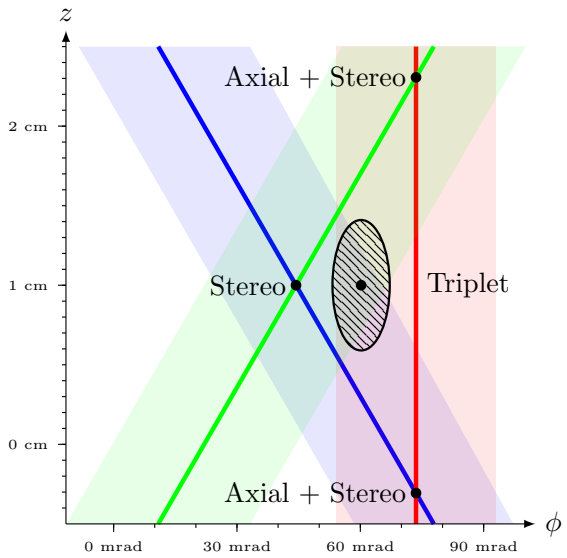


Figure 4.2: Strip intersections on flattened surface. Solid lines indicate strip centers and shaded areas represent strips. The triplet point has been calculated and is shown. If the strips do not have a significant overlap, the $\chi^2$ value will be large and the triplet will be ignored. The ellipse indicates the estimated error in the triplet reconstruction, using $\delta\phi_{\text{hit}} = w/\sqrt{12}\sqrt{\frac{1+\lambda^2}{3+\lambda^2}}$ and $\delta z_{\text{hit}} = w/\sqrt{12}\sqrt{\frac{1+\lambda^2}{2\lambda^2}}$, where $\lambda = \tan\theta_{\text{st}}$.

on the surface of the cylinder. Each strip is described by the equation:

$$\phi = \phi_{s,i} + \Omega_s \frac{z}{L}, \tag{4.1}$$

where $\phi$ is the azimuthal coordinate of the strip at location $z$ along the axis, and $\Omega_s$ is the wrap angle for that layer. This description, along with a suitable offset factor, can be used to parametrize the strips for simulation in a system such as Geant4.

### 4.2.1 Strip Intersections

To determine which strips registering a hit correspond to a common region where a muon passed through the detector, it is first assumed that the muon track intersected all three scintillator layers at the same azimuth and same $z$ location (that is another way of stating the previous assumption). This assumption of identical coordinates for all hits is unphysical, but it can provide an initial estimate of the muon trajectory which can be corrected for actual layer radii and other "real-world" effects using

methods described below. In what follows, we compute coordinates of idealized intersections of hit strips from each of the three tracking layers. The labels of a group of three strips are $\phi_s$; their corresponding intersections are denoted by $\phi_{s,i}$ and $z_{s,i}$ using $s$ to label the strip layer, as above. An example triplet is shown in Figure 4.2.

#### 4.2.1.1 Stereo Intersections

We will begin by looking at the two-strip intersections. The inner and outer layers, referred to as $-$ and $+$, respectively, need to be treated specially. We will start by looking at only these two layers, and finding the intersection point of just these two layers, the point labeled in Figure 4.2 as "Stereo".

Finding the intersection of strips from each of the stereo layers involves certain subtleties related to the "wrap-around" of the azimuthal coordinate at $\phi = 0,\, 2\pi$. Care must be taken to avoid nonsense results where true intersections map to the wrong ($\phi$, $z$) coordinate or where "fake" intersections are generated when the hit strips don't actually cross. Correct intersections are best visualized by considering the azimuths of the $-$, $+$ strips at the bottom end ($z = -L/2$) of the detector. It is clear that if the hit strips are nearby at the bottom end and if the strip on the $-$ layer is at a smaller azimuth than that of the hit $+$ strip, then there will be no intersection. To quantify this, we define the azimuthal difference $\Phi$ between the $-$ hit strip and the $+$ hit strip evaluated at the bottom of the detector. $\Phi$ is found by solving:

$$\cos\Phi = \cos\left(\phi_- - \phi_+ + \frac{\Omega_+ - \Omega_-}{2}\right) \tag{4.2}$$

$$\sin\Phi = \sin\left(\phi_- - \phi_+ + \frac{\Omega_+ - \Omega_-}{2}\right), \tag{4.3}$$

with the condition that $\Phi$ is chosen within the interval $0-2\pi$. The above relations will be satisfied for true hits when $\Phi$ is in the range $0 \le \Phi \le \Omega_+ - \Omega_-$. Not all $-$, $+$ pairs of strips will have valid intersections because not all stereo strips cross; combinations of stereo strips with a value for $\Phi$ falling in the range $2\pi > \Phi > (\Omega_+ - \Omega_-)$ are not kept for event reconstruction.

A stereo pair will intersect at a $z$-coordinate given by:

$$\frac{z_{-,+}}{L} = \frac{\Phi}{\Omega_+ - \Omega_-} - \frac{1}{2}. \tag{4.4}$$

The corresponding azimuthal coordinate is found from the previous equations. Taking care with "wrap-around", the conditions on the azimuthal intersection coordinate are:

$$\cos\phi_{-,+} = \cos\left(\phi_+ + \Omega_+\frac{z_{-,+}}{L}\right) \tag{4.5}$$

$$\sin\phi_{-,+} = \sin\left(\phi_+ + \Omega_+\frac{z_{-,+}}{L}\right), \tag{4.6}$$

with the usual requirement that the solution satisfy $0 \leq \phi_{-,+} < 2\pi$.

#### 4.2.1.2 Axial + Stereo Intersections

When only considering one of the stereo layers and the axial layer, the axial layer azimuth can be used as the azimuth directly, and the $z$-coordinate can be found:

$$\frac{z_{0,\pm}}{L} = \frac{(\phi_0 - \phi_\pm + \pi) \bmod 2\pi - \pi}{\Omega_\pm}, \tag{4.7}$$

subject to the condition $-0.5 \leq z_{0,\pm}/L \leq 0.5$.

#### 4.2.1.3 Wrap Angle Approach

It is easiest to understand the preceding results when the coordinates of the hit strips are in the first two quadrants of the detector azimuth, $0 \leq \phi_-, \phi_0, \phi_+ \leq \pi$. In this situation, there is no $2\pi$ wrap-around to contend with and the stereo strip intersection coordinates are simply:

$$\frac{z_{-,+}}{L} = \frac{\phi_- - \phi_+}{\Omega_+ - \Omega_-} \tag{4.8}$$

$$\phi_{-,+} = \frac{\Omega_+\phi_- - \Omega_-\phi_+}{\Omega_+ - \Omega_-}. \tag{4.9}$$

In the case where the stereo layers have stereo angles equal in magnitude, but opposite in sign with $\lambda = |\tan\theta_s|$ and their radii are separated from the axial layer by the thickness of the scintillator strips according to $R_\pm = R \pm T$, the above expressions reduce to:

$$\frac{z_{-,+}}{L} = \frac{\phi_- - \phi_+}{2\lambda} \tag{4.10}$$

$$\phi_{-,+} = \frac{\phi_- - \phi_+}{2} - \lambda\frac{T}{R}\frac{z_{-,+}}{R}. \tag{4.11}$$

It is interesting to note that the "thickness correction" implied by the second term in Equation 4.11 partially compensates for the thickness corrections which arise from the actual muon trajectory crossing tracking layers of different radii.

#### 4.2.1.4 Triplets

The essential idea in reconstructing triplets is that the intersection of two stereo strips provides an accurate determination of azimuth of the hit, comparable in resolution to that determined by the corresponding axial strip. We will use a $\chi^2$ test to determine if all three overlap within the estimated accuracy of the system.

The $z$-coordinate for triplets is taken from the overlap of the two stereo layers as described previously, $z_{\rm hit} = z_{-,+}$. It is straightforward to show that the optimum choice for the azimuthal coordinate $\phi_{\rm hit}$ is found from the stereo overlap $\phi_{-,+}$ and the axial coordinate $\phi_0$ by the weighted average:

$$\phi_{\rm hit} = \frac{w_0\phi_{-,+} + (w_- + w_+)\,\phi_0}{w_- + w_0 + w_+}, \tag{4.12}$$

where the indicated weights $w_s$ are given by:

$$w_- = \sigma_-^2 \frac{\Omega_+^2}{(\Omega_+ - \Omega_-)^2} \tag{4.13}$$

$$w_0 = \sigma_0^2 \tag{4.14}$$

$$w_+ = \sigma_+^2 \frac{\Omega_-^2}{(\Omega_+ - \Omega_-)^2}. \tag{4.15}$$

The $\sigma$'s represent the root mean squared (RMS) spread in azimuths across the particular strip. Using the angular width of the strips $\Delta\phi_s$, the corresponding RMS spread is $\sigma_s = \Delta\phi_s/\sqrt{12}$. The value of $\chi^2$ at the optimum hit is:

$$\begin{aligned} \chi^2_{\rm min} &= \frac{(\phi_{-,+} - \phi_0)^2}{w_- + w_0 + w_+} \\ &= \frac{w_- + w_0 + w_+}{w_0^2}\left(\phi_{\rm hit} - \phi_0\right)^2. \end{aligned} \tag{4.16}$$

This set of parameters, $\chi^2_{\rm min}$, $\phi_{\rm hit}$, and $z_{\rm hit}$, can be precomputed and stored in a three dimensional lookup table addressed by the strip indices. Plausible triplets are selected based on the value of $\chi^2_{\rm min}$; any values above a cut are not valid triplets. This is the first cut. Once a collection of possible triplets is created, the thickness corrections described below are used to select the best triplet pair.

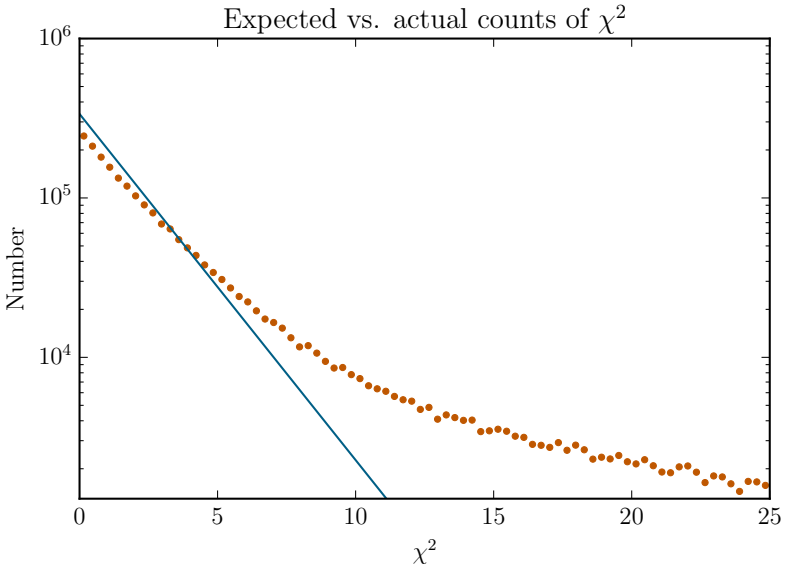


Figure 4.3: The $\chi^2$ distribution of the combined triplets approximately follows the expected curve from two degrees of freedom with the same total number of entries for small $\chi^2$. We cut on $\chi^2 < 10$. This is from 21 hours of data.

This information is enough to compute tracks; a point on the track from a given triplet is found from:

$$\mathbf{x} = R_0 \cos\phi_{\text{hit}}\hat{\mathbf{x}} + R_0 \sin\phi_{\text{hit}}\hat{\mathbf{y}} + z_{\text{hit}}\hat{\mathbf{z}}. \tag{4.17}$$

Two points are provided by the two triplets, thereby defining a line. The trajectory is defined with the unit vector along the track, $\hat{\mathbf{u}} = \frac{\mathbf{x}_1 - \mathbf{x}_2}{|\mathbf{x}_1 - \mathbf{x}_2|}$, and the point of closest approach $\mathbf{X} = \frac{x_1 + x_2}{2}$. The order of the two tracks is chosen to provide a positive vertical component for $\hat{\mathbf{u}}$.[1]

The sum of the two $\chi^2_{\text{min}}$ values is a $\chi^2$ distribution with two degrees of freedom, $e^{-\chi^2/2}$, because the six hit strips are used to determine two independent direction coordinates (azimuth and elevation) and two position coordinates (radial and axial coordinates of closest approach) for the track. As seen in Figure 4.3, the residuals approximate the line predicted by such a distribution for small $\chi^2$.

[1]Note that this must be done again after the thickness correction is applied, as that may change the orientation of nearly horizontal tracks.

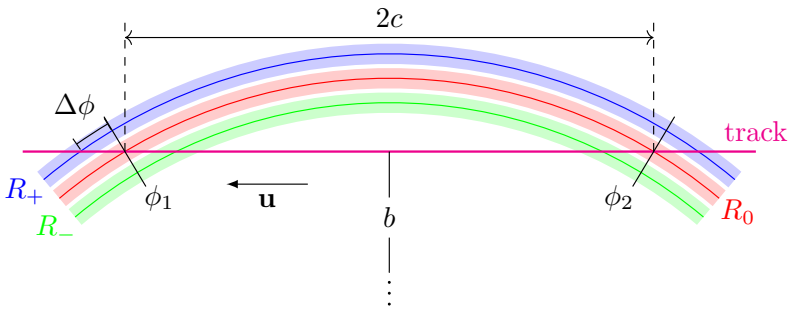


Figure 4.4: Track intersecting the three physical layers of the detector. The radius to the center of the layer is indicated and labeled for each of the three layers.

#### 4.2.1.5 Thickness Corrections

Implicit in the definition of hit coordinates associated with a triplet or doublet is that the track intersects each tracking layer at the same azimuth and same $z$-location. This is equivalent to assuming that all three tracking layers have the same mean radius. In reality, the layers have different mean radii, $R_-$, $R_0$, and $R_+$. Consequently, real tracks will intersect the inner and outer layers at different values of azimuth and $z$-location depending on trajectory. By symmetry, the inner and outer layers of both the entrance and exit intersections will be offset from the central location by common amounts (in magnitude) $\Delta\phi$ and $\Delta z$.

The net effect of the nonzero difference between radii of the various tracking layers is to move the apparent intersection of the stereo layers $\phi_{-,+}$, $z_{-,+}$ away from the true hit location. Because the layer thickness $t$ is comparable to typical strip widths, effects of nonzero layer thickness will affect system performance at levels that could be significant when compared to the irreducible tracking resolution.

We are using a two stage reconstruction. The first stage reconstructs tracks assuming no thickness corrections, as described above. The second stage uses the first-approximation to the trajectory in the zero-thickness approximation to compute $\Delta\varphi$, $\Delta z$, which are then used to find improved or "corrected" intersection coordinates.

In the following, the corrections to the apparent location of the intersection labeled by $\mathbf{x}_1$ are derived. As noted previously, the symmetry of the tracking system leads to the same corrections, but opposite in sign, being applied to $\mathbf{x}_2$, where $\mathbf{x}_1$ and $\mathbf{x}_2$ are related as above. The unit vectors and quantities indicated are useful for describing

thickness-corrections. In particular, the unit-normal to the track direction $\hat{\mathbf{b}}$, which lies in the horizontal plane, and a third tracking basis vector $\hat{\mathbf{t}}$ are defined by:

$$\hat{\mathbf{b}} = \frac{\hat{\mathbf{z}} \times \hat{\mathbf{u}}}{|\hat{\mathbf{z}} \times \hat{\mathbf{u}}|} = \frac{\hat{\mathbf{z}} \times \hat{\mathbf{u}}}{\sqrt{1 - (\hat{\mathbf{z}} \cdot \hat{\mathbf{u}})^2}} \tag{4.18}$$

$$\hat{\mathbf{t}} = \hat{\mathbf{u}} \times \hat{\mathbf{b}}. \tag{4.19}$$

The signed "impact-parameter" of the track $b$ and corresponding half-chord $c$ of the track crossing the detector are:

$$b = -\hat{\mathbf{b}} \cdot \mathbf{X} \tag{4.20}$$

$$c = \sqrt{R_0^2 - b^2}. \tag{4.21}$$

The respective $z$-coordinates of the intersection points are indicated by $z_1$ and $z_2$. Using these definitions, the thickness correction parameters are determined from geometry to be

$$\Delta\phi = \frac{t\, b}{R_0 c} \tag{4.22}$$

$$\Delta z = \frac{t\,(z_1 - z_2)\, R_0}{2c^2}. \tag{4.23}$$

The above parameters are related to the thickness-corrected shifts in the intersection coordinates of the stereo layers:

$$\delta\phi_{-,+} = \left(\frac{\Omega_+ + \Omega_-}{\Omega_+ - \Omega_-}\right)\Delta\phi - \left(\frac{2\Omega_+\Omega_-}{\Omega_+ - \Omega_-}\right)\frac{\Delta z}{L} \tag{4.24}$$

$$\delta z = \left(\frac{2L}{\Omega_+ - \Omega_-}\right)\Delta\phi - \left(\frac{\Omega_+ + \Omega_-}{\Omega_+ - \Omega_-}\right)\Delta z, \tag{4.25}$$

and therefore the corrected coordinates are:

$$\phi^{\mathrm{c}}_{\mathrm{hit}} = \phi_{\mathrm{hit}} + \frac{w_0}{w_- + w_0 + w_+}\delta\phi_{+,-} \tag{4.26}$$

$$z^{\mathrm{c}}_{\mathrm{hit}} = z_{\mathrm{hit}} + \delta z. \tag{4.27}$$

These coordinates can be used to determine the corrected intersection locations. The other hit location follows the same logic, only with opposite signs for the thickness correction parameters. The values of $\chi^2$ associated with each intersection are computing using the corrected azimuthal coordinates:

$$\chi^{2,\mathrm{c}}_{\mathrm{min}} = \frac{w_- + w_0 + w_+}{w_0^2}\left(\phi^{\mathrm{c}}_{\mathrm{hit}} - \phi_0\right)^2. \tag{4.28}$$

As mentioned above, the sum of the $\chi^2$ for both corrected triplets is a measure of "goodness-of-fit" for the reconstructed track even though a least-squares fit is not being used. A track with $\chi^2 > 10$ does not pass the requirements to be reconstructed into a track and is discarded.

## 4.3 Histogram Parameters

A key development that has enabled the use of the detectors for extended periods of time has been the adaptation of the on-board live histogram system. The detectors do not store individual tracks, but rather perform the reconstruction on-board the internal computer and store a histogram of the reconstructed parameters.

Once a track is reconstructed, the representation can be changed to use four unique parameters. Any ray can be described either by vector notation, $\mathbf{X} + t\hat{\mathbf{D}}$, or by four coordinates $\phi$, $\cot\theta$, $z$, and $b$. To convert to the four parameter notation, we will take $\mathbf{X}$ to be $\mathbf{X}_{\rm ca}$ and $\hat{\mathbf{D}}$ to be $\hat{\mathbf{u}}$, with everything defined in the detector coordinates, and we will use the parameters $\hat{\mathbf{u}}$, $\hat{\mathbf{b}}$, and $\hat{\mathbf{t}}$ from above. We have the parameters:

$$\tan\phi = \frac{\hat{\mathbf{y}}_{\rm d}\cdot\hat{\mathbf{u}}}{\hat{\mathbf{x}}_{\rm d}\cdot\hat{\mathbf{u}}} \tag{4.29}$$

$$\cot\theta = \frac{\hat{\mathbf{z}}_{\rm d}\cdot\hat{\mathbf{u}}}{\sqrt{1-(\hat{\mathbf{z}}_{\rm d}\cdot\hat{\mathbf{u}})^2}} \tag{4.30}$$

$$z = \frac{\hat{\mathbf{t}}\cdot\mathbf{X}}{\sqrt{1-(\hat{\mathbf{z}}_{\rm d}\cdot\hat{\mathbf{u}})^2}} \tag{4.31}$$

$$b = \hat{\mathbf{b}}\cdot\mathbf{X}. \tag{4.32}$$

Notice that this was built to only allow positive values of $\cot\theta$, so it covers all possible lines exactly once; that is, there is no redundancy for lines going in the opposite direction. The values of $\phi$ should be in the range $[0,\, 2\pi)$. If it is necessary to go back to the vector definition, that is simply:

$$\mathbf{X}_{\rm ca} = b\cos\left(\phi-\frac{\pi}{2}\right)\hat{\mathbf{x}}_{\rm d} + b\sin\left(\phi-\frac{\pi}{2}\right)\hat{\mathbf{y}}_{\rm d} + z\hat{\mathbf{z}}_{\rm d}, \tag{4.33}$$

and

$$\mathbf{D} = \cos(\phi)\hat{\mathbf{x}}_{\rm d} + \sin(\phi)\hat{\mathbf{y}}_{\rm d} + \cot\theta\hat{\mathbf{z}}_{\rm d}. \tag{4.34}$$

| Parameter | Min | Max | Cells | Width | Error | Simulated |
|---|---|---|---|---|---|---|
| $\phi$ | 0 | $2\pi$ | 600 | 10 mrad | 4.8 mrad | 8.3 mrad |
| $\cot\theta$ | 0 | 2 | 150 | 0.013 | .013 | 0.018 |
| $z$ | $-L/2$ | $L/2$ | 20 | 6.86 cm | 0.29 cm | 0.40 cm |
| $b$ | $-0.8R_0$ | $0.8R_0$ | 10 | 2.07 cm | 0.091 cm | .21 cm |

Table 4.2: Histogram parameters

Parameters of the histogram, with cell width. The expected error and Geant4 simulated tracking error are included for reference.

The tracks are required to pass several cuts to be valid. The value of $\cot\theta$ should be in the range [0, 2]. The $b$ parameter has a cut defined as $b_{\max} = 0.8\,R_0$, such that $-b_{\max} \leq b \leq b_{\max}$. The value for $z$ is cut to the length of the detector, such that $-L/2 \leq z \leq L/2$. Once these cuts are passed, the tracks are placed in a histogram with the parameters listed in Table 4.2. These parameters were carefully chosen to represent the detector resolution. The parameters were intended to be slightly oversampled in $\phi$ and $\cot\theta$, since the expected resolution from neighboring strips was of order 20 mrad. The distance parameters are undersampled, since these parameters are not as important for the expected distance scales that the detector was designed for.

The flux in each histogram cell is simply the count rate times the solid angle subtended by the individual histogram cell,

$$\Phi_i = \frac{n_i}{t} \frac{\left(\cot^2\theta_i + 1\right)^2}{\Delta\phi\Delta\left(\cot\theta\right)\Delta z\Delta b}. \tag{4.35}$$

Here, $t$ is the total runtime counting $n_i$ counts in the bin $i$. The weighting factor is constant for each run in three of the dimensions, changing only in $\cot\theta$.

## 4.4 Expected Detector Performance

### 4.4.1 Acceptance

The detector has an acceptance that depends on the angle $\theta$ from the $z$ axis of the detector. The acceptance is best described by the ratio of the active area to the ideal projected area $f_A = \frac{A}{2RL}$, where $R$ is the detector radius. If we make the

assumption that the muons are uniformly distributed in impact parameter $b$ and vertical coordinate of closest approach $z$ for any given value of $\theta$, then the acceptance is:

$$f_A = \frac{b_{\max}}{R} - \frac{R\cot\theta}{L}\left[\frac{b_{\max}}{R^2}\sqrt{R^2 - b_{\max}^2} + \sin^{-1}\left(\frac{b_{\max}}{R}\right)\right], \tag{4.36}$$

where $\theta$ must satisfy the cut condition $0 \leq \cot\theta \leq 2$, and $b_{\max}$ is the maximum impact parameter allowed by our tracking cut, $b_{\max} = 0.8R$. The detector has no acceptance outside of these values; that is called the "blind cone" of the detector due to the conical shape of the insensitive region.

### 4.4.2 Tracking Resolution

The finite granularity of the tracking system leads to irreducible errors $\delta$, $\zeta$ in the (corrected) coordinates $\phi_{\rm hit}$, $z_{\rm hit}$ deduced for the intersection locations on the basis of strip centers. The variances of these quantities $\langle\delta^2\rangle$, $\langle\zeta^2\rangle$ are related to strip widths through the weights $w_-$, $w_0$, $w_+$ introduced above as:

$$\langle\delta^2\rangle = \frac{w_0\,(w_- + w_+)}{w_- + w_0 + w_+} \tag{4.37}$$

$$\langle\zeta^2\rangle = L^2\left(\frac{w_-}{\Omega_+^2} + \frac{w_+}{\Omega_-^2}\right). \tag{4.38}$$

There are no cross-correlations, $\langle\delta\cdot\zeta\rangle = 0$, $\langle\delta_1\cdot\delta_2\rangle = 0$, etc. For a typical detector, such as detector 3, the values of these errors are $\langle\delta^2\rangle = .0041$ and $\langle\zeta^2\rangle = .0013\,\mathrm{m}^2$.

The resulting tracking errors of most interest are the track direction error $\delta\hat{\mathbf{u}}$, which is perpendicular to $\hat{\mathbf{u}}$, and the error in the location of the point of closest approach $\delta\mathbf{X}$. The relevant components of these errors are:

$$\left\langle\left(\hat{\mathbf{b}}\cdot\delta\hat{\mathbf{u}}\right)^2\right\rangle = \frac{1}{4}\left(\langle\delta_1^2\rangle + \langle\delta_2^2\rangle\right)\left[1 - (\hat{\mathbf{u}}\cdot\hat{\mathbf{z}})^2\right] \tag{4.39}$$

$$\left\langle\left(\hat{\mathbf{t}}\cdot\delta\hat{\mathbf{u}}\right)^2\right\rangle = b^2\frac{\left(\langle\delta_1^2\rangle + \langle\delta_2^2\rangle\right)}{|\mathbf{x}_1 - \mathbf{x}_2|^2}(\hat{\mathbf{u}}\cdot\hat{\mathbf{z}})^2 + 4c^2\frac{\left(\langle\zeta_1^2\rangle + \langle\zeta_2^2\rangle\right)}{|\mathbf{x}_1 - \mathbf{x}_2|^4} \tag{4.40}$$

$$\left\langle\left(\hat{\mathbf{b}}\cdot\delta\mathbf{X}\right)^2\right\rangle = \frac{1}{4}c^2\left(\langle\delta_1^2\rangle + \langle\delta_2^2\rangle\right) \tag{4.41}$$

$$\left\langle(\hat{\mathbf{z}}\cdot\delta\mathbf{X})^2\right\rangle = \frac{1}{4}\left(\langle\zeta_1^2\rangle + \langle\zeta_2^2\rangle\right). \tag{4.42}$$

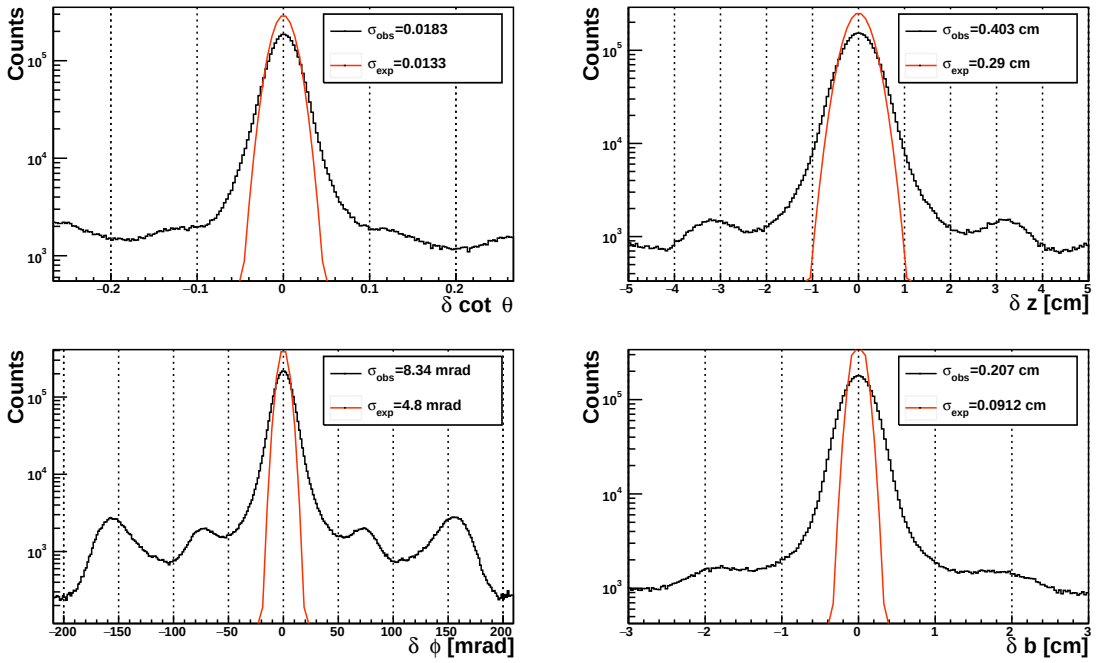


Figure 4.5: Difference in the track parameters before and after reconstruction. Muons were uniformly generated in momentum from 0 to 5 GeV and in direction, and run through a Geant4 simulation and reconstructed based on a response model on the hit strips. A Gaussian was fit with ROOT [45] (not shown) to measure the approximate $\sigma_{\text{obs}}$. The $\sigma_{\text{exp}}$ was calculated from Equations 4.39 to 4.42, and is shown as a normalized Gaussian curve in red for reference.

These tracking errors, given standard detector parameters, can be estimated. If we assume an average value of $c^2$ of $\frac{1}{2}R_0^2$ and $b^2$ of 0.1 m, take the average value of $(\hat{\mathbf{u}} \cdot \hat{\mathbf{z}})^2$ to be 0.5, and take an average triplet separation distance to be .5 m, we get the tracking errors of $\delta\phi \approx 4.8$ mrad, $\delta \cot\theta \approx 0.013$, $\delta b \approx 0.0912$ cm, and $\delta z \approx .29$ cm.

To test this simple model of tracking errors against Monte Carlo, a distribution that had muon direction uniformly distributed over the unit sphere was created. Muon momentum was uniformly distributed from 0 to 5 GeV/c. The tracking error is defined as the original generated parameter subtracted from the parameter derived from the reconstruction process using the energy deposited in each strip via Monte Carlo simulation. The resulting differences between generated and tracked parameters are plotted in Figure 4.5, along with the predicted errors from the finite strip widths and the geometry of the detector. The prediction is similar to the Monte Carlo,

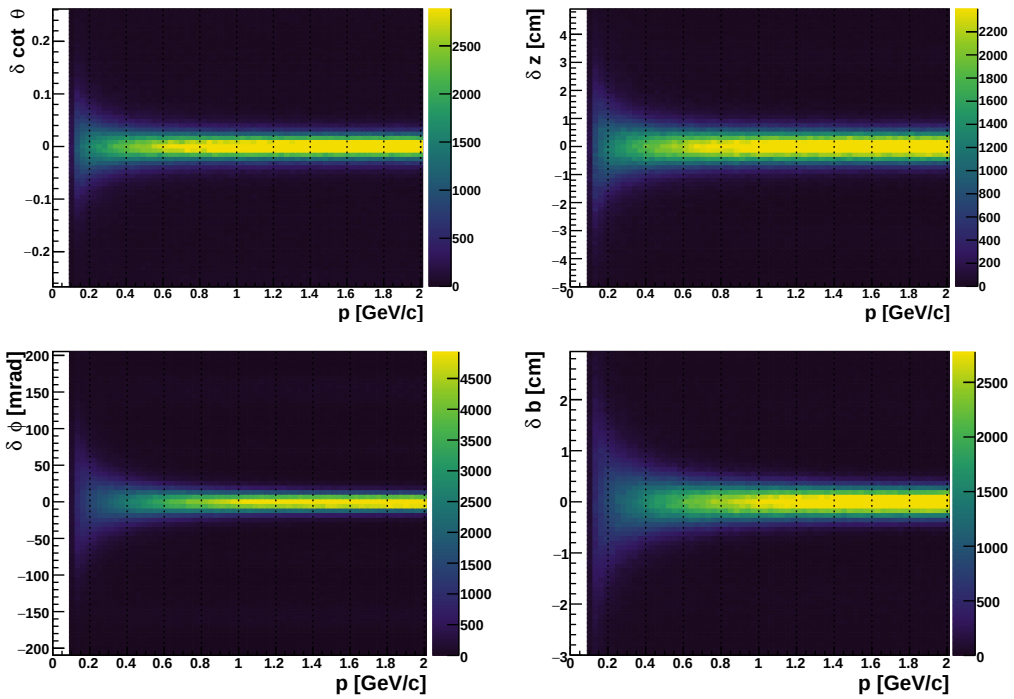


Figure 4.6: Difference in the track parameters before and after reconstruction. Muons were uniformly distributed in momentum from 0 to 5 GeV and in direction.

with a slightly wider distribution of simulated errors, due to the extra scattering and detector noise included in the simulation.

This provides a predictable baseline for observing the behavior of the detector as a function of momentum. In Figure 4.6, the original muon momentum has been included, showing good agreement with the predictions above, and a divergence in all tracking parameters around $p < 0.5 - 0.3\,\text{GeV}$.

In Figure 4.7, the width of the Gaussian fit on the tracking parameters is plotted as a function of momentum, clearly showing the divergence as the momentum drops. Above about 1.5 GeV, the Gaussian width approaches a constant value $A$. The explosion from multiple scattering at low momentum is characterized by $B$ in the empirical fit $A + B/p^2$, where $p$ is in GeV. This is just meant to roughly approximate the low momentum divergence.

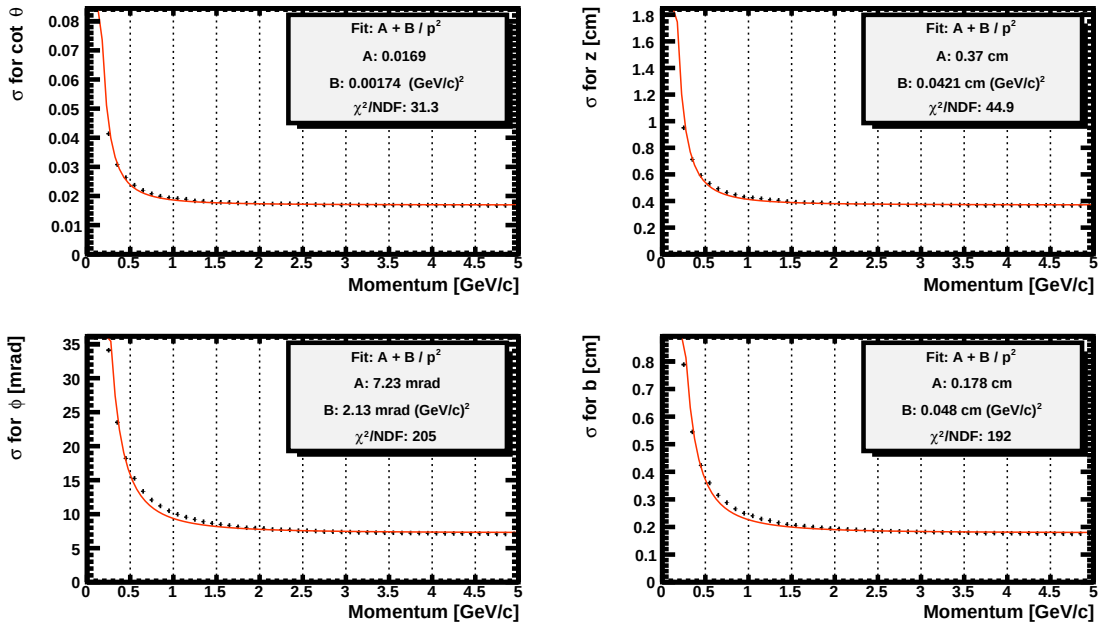


Figure 4.7: Plot of Gaussian $\sigma$ along slices of $p$. Muons were uniformly distributed in momentum from 0 to 5 GeV and in direction. Fits were made over the range 200 MeV to 5 GeV.

### 4.4.3 Trigger Low Momentum Limit

To test the minimum momentum required to trigger the detector, the same simulation described above was used, with a uniform momentum and direction distribution. The results are plotted in Figure 4.8. The low momentum cutoff is clearly defined at $100 - 125$ MeV, with a minor angle dependence, due to the larger amount of detector material to be traversed to trigger a hit for rays approaching the detector axis.

There is a slightly increased efficiency between 100 MeV and 300 MeV that can be attributed to extra hit strips probably due to extra scattering and energy deposit in this region as the muons are ranging out.

### 4.4.4 Detector Efficiency

Simulated runs (using the tools described in Chapter 6) were performed to test the tracking performance of the detector against the input distribution. With the log Gaussian distribution, the tracking and reconstruction efficiency from the simulation

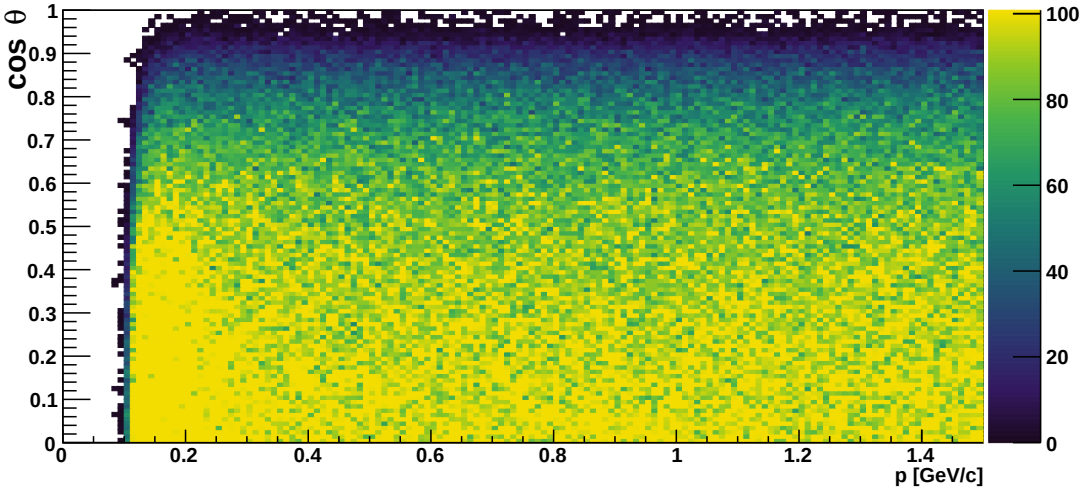


Figure 4.8: Original muon parameters for muons that successfully passed the tracking procedure. Muons were uniformly distributed in momentum from 0 to 5 GeV and in direction. The color scale represents counts detected.

was 55.4% in the horizontal orientation, and 52.5% in the vertical orientation. The uniform distribution from 0 to 5 GeV provided an overall efficiency of 62.3%.

The uniform distribution provides a clear look at the reconstruction efficiency over several parameters. The histograms in Figures 4.9 and 4.10 display the behavior of the detector over the angular spectrum. The aliasing from the strip design are visible in the $\phi$ plot.

The 2D $bz$ histogram, Figure 4.11, illustrates the correlation between the $b$ and $z$ parameters. The end caps of the detector cause reduced tracking efficiency for large $z$, especially for small $b$, due to the open ends. The visible asymmetry in $z$ is from the attenuation of light in the fiber and the readout at one end of the detector.

### 4.4.5 Multiple Coulomb Scattering

The measured track is used to estimate the true muon path before it reaches the detector; however, multiple-Coulomb scattering in the material between detector and a point of interest will cause an error in the track reconstruction that could soften the tomographic image. This effect is not always negative when imaging, however;

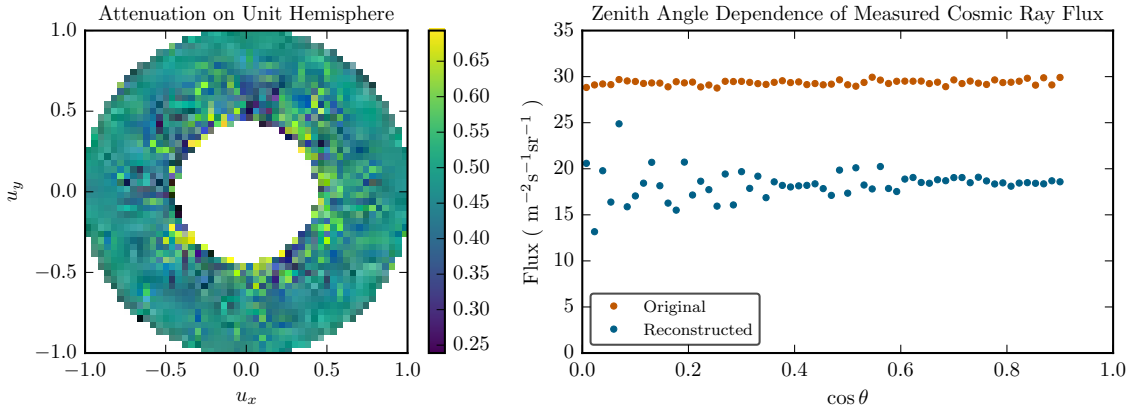


Figure 4.9: The simulated angular distribution, before and after the tracking process. On the left, a fly's-eye plot of the attenuation in the reconstruction shows excellent uniformity across the unit hemisphere, with a slight breakdown near the detector axis. On the right, a comparison over just $\cos\theta$ shows the effect of strip aliasing increase as the product $\hat{\mathbf{z}}_{\text{det}} \cdot \hat{\mathbf{u}}$ goes to zero.

if a muon scatters and misses the detector, it will appear to have attenuated in the material and will enhance the contrast for solid targets.

The original design of the detector, and the subsequent redesign, were based on the expected error from coulomb scattering first described in Schwitters [9]. For a homogeneous material with uniform density $\rho = 2.3\,\text{gm cm}^{-3}$, muon energy-loss $\frac{dE}{dx} = 2.2\,\text{MeV cm}^2\,\text{gm}^{-1}$ and radiation length $X_0 = 27\,\text{gm cm}^{-2}$, we can calculate the error $\delta y\,(t)$ in the muon trajectory at a distance $t$ from the detector (See Figure 4.12). The material between the point of interest along the reconstructed track and the detector is assumed to be thick compared to $X_0$, and only small-angle, Gaussian distributed scattering is considered. This description breaks down for larger angle scattering, where the scattered distribution will approach Rutherford scattering in the asymptotic limit, with larger tails than a Gaussian distribution [46]. The small angle behavior is sufficient for the discussion of error presented here.

Once a muon reaches the detector, it will have a final momentum $p_{\text{f}}$ . The RMS multiple scattering angle in each plane is computed by assuming a loss of momentum in the material of $p\,(x) = p_0 - x\frac{dE}{dx}$ and integrating over the uncorrelated mean-square

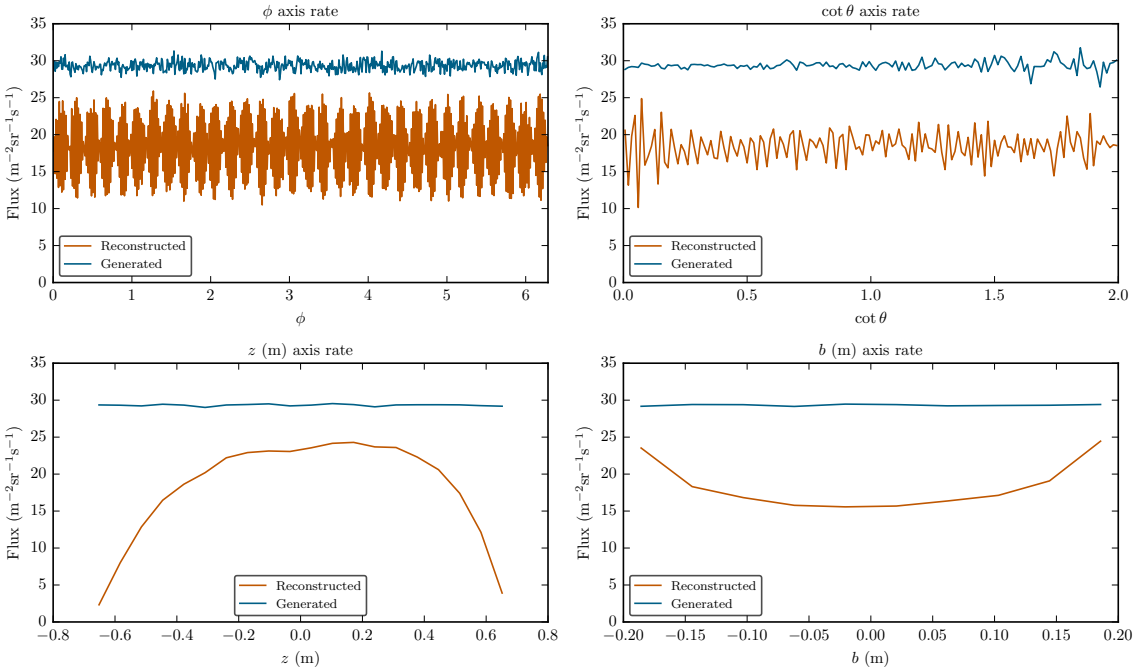


Figure 4.10: Simulated flux over each of the four parameters, before and after the tracking process. Strip aliasing is seen in the $\phi$ plot in the upper left. No strong dependence is seen in the $\cot\theta$ plot on the upper right. The overall slope and loss at the ends is seen in the $z$ plot on the lower left. The minor increase on either end of the $b$ plot on the lower right is from the extra trigger probability for large $|b|$ hits.

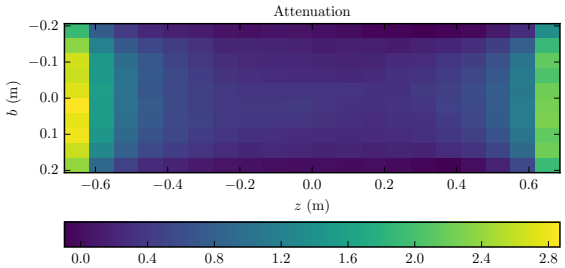


Figure 4.11: The simulated flux over $b$ and $z$ of the detector from a uniform distribution. The asymmetry in $z$ for this plot shows the detector readout end, as well as the losses due to the cylinder truncation.

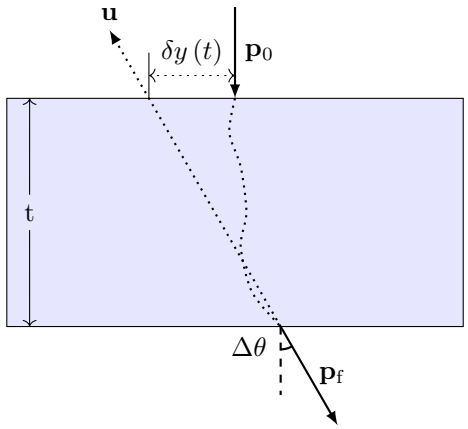


Figure 4.12: Multiple-Coulomb scattering in a medium of thickness $t$. The detected muon direction is denoted by its direction or by the unit vector pointing toward its reconstructed origin, $\mathbf{p}_\mathrm{f}/p_\mathrm{f} = -\hat{\mathbf{u}}$. The muon enters the medium with momentum $\mathbf{p}_0$. The error in the reconstructed path at the point where the muon enters the scattering medium is $\delta y\,(t)$.

scattering angle $\langle \delta\theta^2 \rangle$ in thin elements of width $dx$ across the full thickness,

$$\begin{aligned} \left\langle \delta\theta^2 \right\rangle &= \int_0^r \frac{dx}{X_0} \frac{\left(13.6\,\mathrm{MeV/c}\right)^2}{p^2\,(x)} && (4.43) \\ &= \frac{r}{X_0} \frac{\left(13.6\,\mathrm{MeV/c}\right)^2}{p_0 p_\mathrm{f}}, && (4.44) \end{aligned}$$

where $p_0 = p_\mathrm{f} + r\,dE/dx$.

The variance $\langle \delta y_0^2 \rangle$ in the predicted location $\delta y\,(r)$ of the muon track a distance $r$ from the detector is then related to the second moment of the mean-square scattering angle,

$$\begin{aligned} \left\langle \delta y_0^2 \right\rangle &= \int_0^r \frac{x^2 dx}{X_0} \frac{\left(13.6\,\mathrm{MeV/c}\right)^2}{p^2\,(x)} && (4.45) \\ &= D\left(\frac{r}{p_0}\frac{dE}{dx}\right) r^2 \left\langle \delta\theta^2 \right\rangle, && (4.46) \end{aligned}$$

where correlations between position and deflection angle in multiple-Coulomb scattering are described for thick targets by the function $D\,(a)$,

$$\begin{aligned} D\,(a) &= \left(\frac{1-a}{a^3}\right)\left[a\left(1+\frac{1}{1-a}\right)+2\ln\left(1-a\right)\right] \\ &= \frac{1}{3}+\frac{1}{6}a+\frac{1}{10}a^2+\frac{1}{15}a^3+\cdots. && (4.47) \end{aligned}$$

The function $D(a)$ monotonically increases over the interval $0 \leq a \leq 1$ with endpoint values $D(0) = 1/3$ and $D(1) = 1$. The thin target result is reproduced by setting $a = 0$, due to the large correlation between exit position and angle in thin targets. If $a = 1$, there is no correlation remaining between exit position and angle, as expected in thick scatterers.

For the case of very thick scatterers, the error in apparent track location can be expressed as an effective scattering angle $\delta_{\text{thick}}$ that only depends on $p_{\text{f}}$:

$$\begin{aligned} \delta_{\text{thick}} &= \lim_{p_0 \gg p_{\text{f}}} \left[ \frac{\langle \delta y_0^2 \rangle^{1/2}}{r} \right] = \frac{13.6\,\text{MeV}}{\sqrt{p_{\text{f}}}} \frac{1}{\sqrt{\frac{dE}{dx} X_0}} \\ &\approx \frac{55.8\,\text{mrad}}{\sqrt{p_{\text{f}}\,(\text{GeV/c})}}. \end{aligned} \tag{4.48}$$

The amount of scattering is inversely related to $p_{\text{f}}$, suggesting that filtering low momentum muons (hardening) will reduce the error from scattering. In the Alvarez experiment, this was accomplished by including a substantial quantity of iron absorber in the detector. In our detector, we did not provide a mechanism to filter low momentum muons, save for the thin shielding and six hit requirement. This has proved to remain useful for tomographic imaging, since two effects help cancel this problem. The first is that scattering occurs over all angles, causing the both scatter in to and out of of the angle of interest. The previously mentioned second effect is that, for dense targets, scattered muons may look like attenuation, because they still reduce the tracks originating from the target at the detector.

This was used to select the angular resolution of our detector design. The resolution of about 20 mrad between strips provides an ideal match for the cosmic ray muon spectrum with an average momentum of 4 GeV and for the distances expected. For larger distances, we expect to measure larger targets, so this has been an effective choice for most situations. The results of this expression are shown in Figure 4.13 for several values of $p_{\text{f}}$.

## 4.5 Flat-fielding

One of the most useful procedures for creating images with our detectors has been the use of flat-fielding. This takes aliasing and other detector design and construction specific effects and effectively removes them. We take the detector and run it under

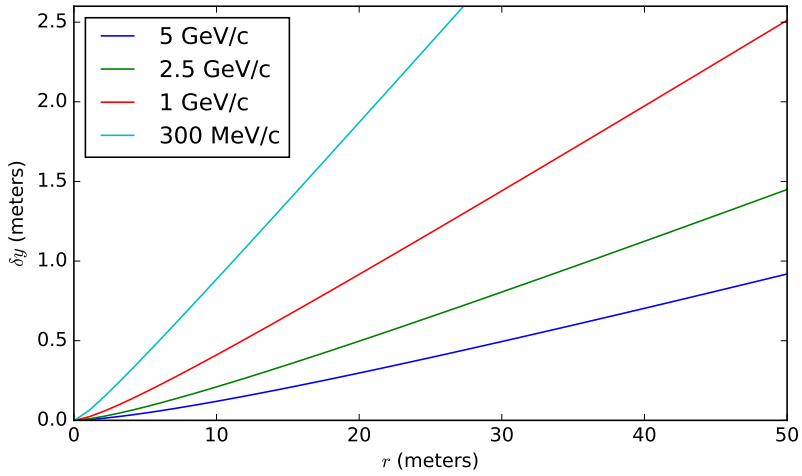


Figure 4.13: Expected error in apparent track location due to multiple-Coulomb scattering for different thickness of rock for a few values of final momentum $p_f$.

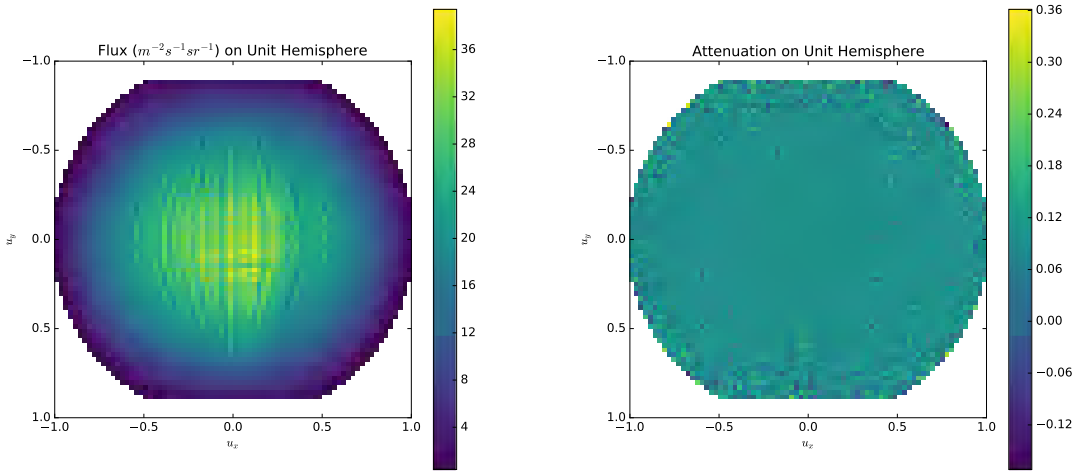


Figure 4.14: Comparison of pure flux and attenuation from detector data. On the left, a plot of the flux with the x and y components of the track direction vector (called a flyseye plot) shows the aliasing from the helical strip structure of the detector. On the right, the attenuation is plotted using a flat field, showing the cancellation of both the strip structure and the $\cos^2\theta$ spectrum.

an open sky (in a "flat field"), collecting at least as much run time as expected data. The attenuation can then be calculated for a given bin $i$ using flat-fielding tracks $b_i$, data tracks $d_i$, and run times $t_b$ and $t_d$, respectively, as:

$$D_{\mu,i} = \log\left(-\frac{d_i}{b_i}\frac{t_b}{t_d}\right). \tag{4.49}$$

An example of the aliasing seen in a run and the effect of flat-fielding is seen in Figure 4.14.

If it is not practical to create a separate flat-fielding run, due to time or other constraints, then there is a method that can be used if certain conditions are met. If one side of the detector has an unobstructed view of the sky, the detector can be rotated around the vertical axis to flat-field one side against the other. Because the strip aliasing will rotate with the detector, the side of the detector previously imaging the attenuating material will now be open to the sky, and the two separate pieces can be combined to get a usable image on one side. This situation is common when placing the detector next to a pyramid or other lone structure.

## 4.6 Detector Response

### 4.6.1 Channels

The detector should have similar hit rates for each channel, since each strip is measured independently, with the exception of small amounts of crosstalk on the PMTs). There are several adjustments that can be made to ensure the raw data are clean. The voltage on the PMTs can be varied to find an optimal signal to noise ratio. The trigger thresholds on the individual ASDs are adjusted to ensure similar performance from each FEB, as seen in Figure 4.15. Under normal running conditions, the eight ASDs corresponding to one PMT are usually close in value, with larger variations between PMTs. The PMTs that are nearest the ends of the high voltage power loop (PMT 0 and PMT 7) usually require the highest threshold. A few ASDs may have hot channels; that is, a single channel with a disproportionately large number of events. The thresholds on these ASDs often are set to maximum to filter as much of the noise as possible; single channel adjustments are not possible.

Filtering by coincidences, that is, events with six or more hits that occur within the four clock cycle time window, should provide a more uniform histogram, as it filters

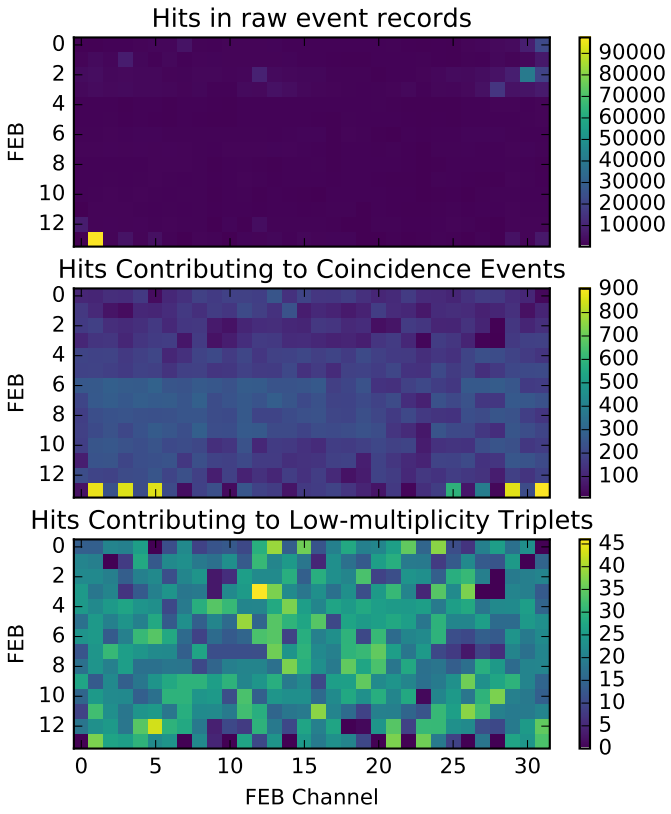


Figure 4.15: Raw hits on the FEBs during a 55 second run are plotted by FEB number and channel. A noisy run was selected to show resiliency to hot channels. Below, the events have been filtered by coincidences, eliminating many of the hits in FEB 13, channel 1, but still leaving several hot channels on FEB 13. Looking at low multiplicity triplets only, the previously hot channels are now completely normal. Several nearly empty channels in the lower plot are normal, since there are several FEB channels that do not have strips attached.

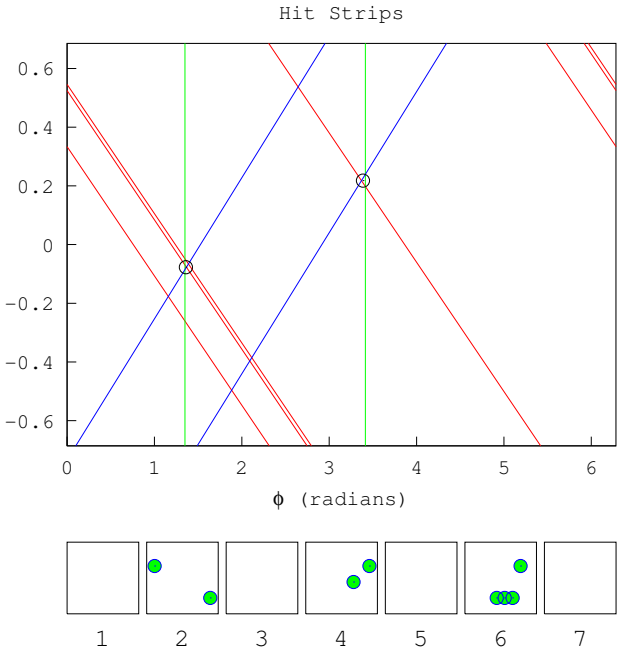


Figure 4.16: An example reconstructed track on an unwrapped cylinder plot. Strips are lines, triplet points are shown with a circle. On the lower left strip intersection, the outer (red) layer shows both neighboring hit strips, and a crosstalk strip (left). The lower portion includes a plot of the PMT hit distribution, showing the crosstalk hit on PMT 6.

out low multiplicity events that make up most of the noise. Tracks are separated by a few thousand clock cycles, so most noise in the sample is from cross-talk between neighboring PMT channels. An average group of hits from a run with Detector 1 is made of 5.7 single hits and 2.7 clustered hits, sharing at least one common edge. Clustered hits contained an averaged at 2.4 hits each. An average of 4.2 FEBs were involved in each event.

### 4.6.2 Tracks

An example of a typical hit track with two extra hits is given in Figure 4.16. The reconstruction system is quite stable even when several extra strips are present, since the minimum $\chi^2$ selection is not significantly affected by uncorrelated extra hits in the time window, or tracks added through crosstalk on neighboring PMT channels.

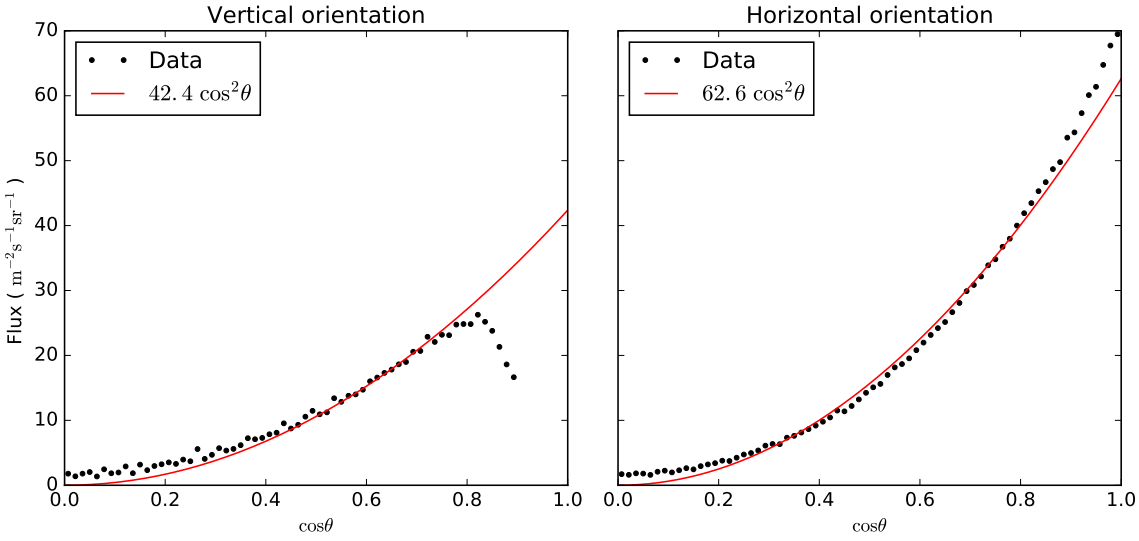


Figure 4.17: Vertical and horizontal orientation detector flux. The data was fit for $0.2 < \cos\theta < 0.8$. The feature visible at $0.8 < \cos\theta < 0.9$ is from the reduced detector efficiency from the hollow ends.

The reconstruction system loops over all possible combinations of triplets, so large events could cause significant increase in processing, but using look up tables for all possible triplets keeps the processing manageable even with extremely noisy data.

The total muon spectrum measured by the detector is given in Figure 4.17. The approximation that the spectrum should behave as $\cos^2\theta$ is plotted as well, using a best fit to the central portion of the plot. For small values of $\cos\theta$, the increase in signal can be attributed to soft muons. For large values of $\cos\theta$, the drop off on the vertical detector orientation is as expected from the dead zone of the detector. The detector observes a nearly $\cos^2\theta$ dependence of flux over almost all angles.

### 4.6.3 Detector Histograms

Several of the properties of the detector can be observed by looking at histograms over the tracking parameters. In Figure 4.18, the strip aliasing can be seen as a high frequency component in the $\phi$ histogram. The $\cot\theta$ histogram shows the reduced flux seen by the detector for tracks at they approach the dead ends at $\cot\theta = 2$. The slope of the $z$ histogram is from attenuation along the fiber, with the reduced

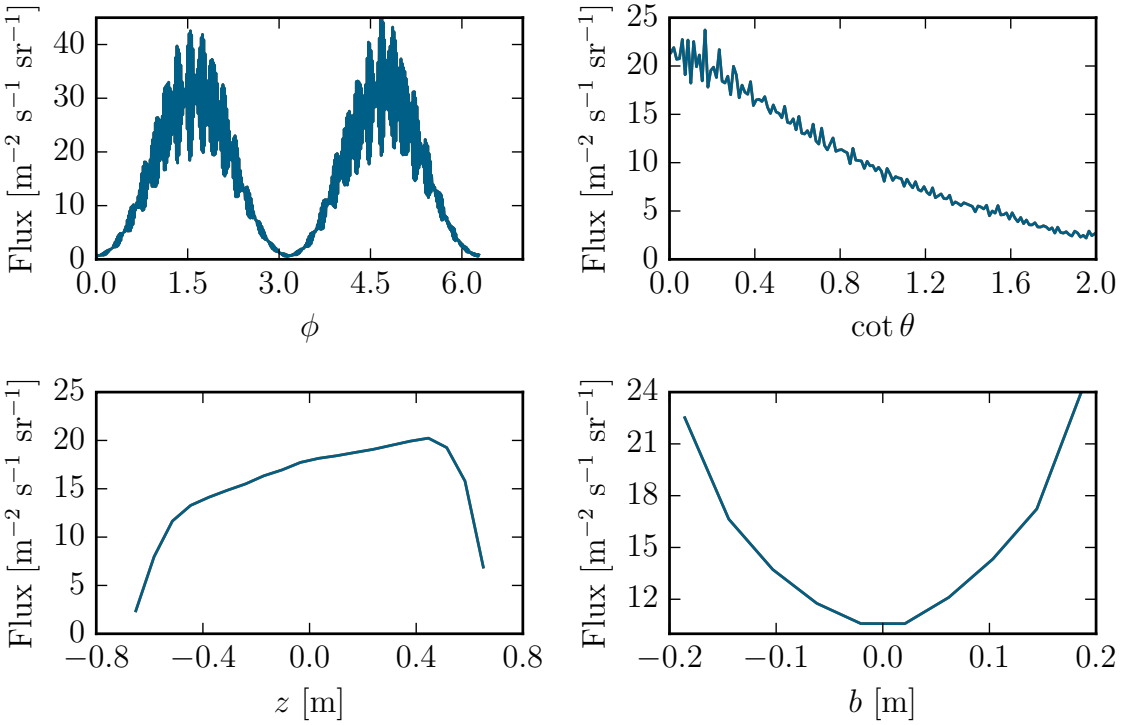


Figure 4.18: The flux observed by the detector in an average horizontal flat fielding run, summed over three of the four histogram parameters. The remaining parameter is shown on the $x$ axis of each plot.

efficiency on either end from the end caps. The increased efficiency on the edges of the $b$ histogram is due to the extra plastic traversed by muons with a large impact parameter.

In Figure 4.19, correlations between the parameters can be seen. The valley running down the middle of the $b$ vs. $z$ histogram is from muons passing close to the axis of the detector; the attenuation can be seen along $z$.

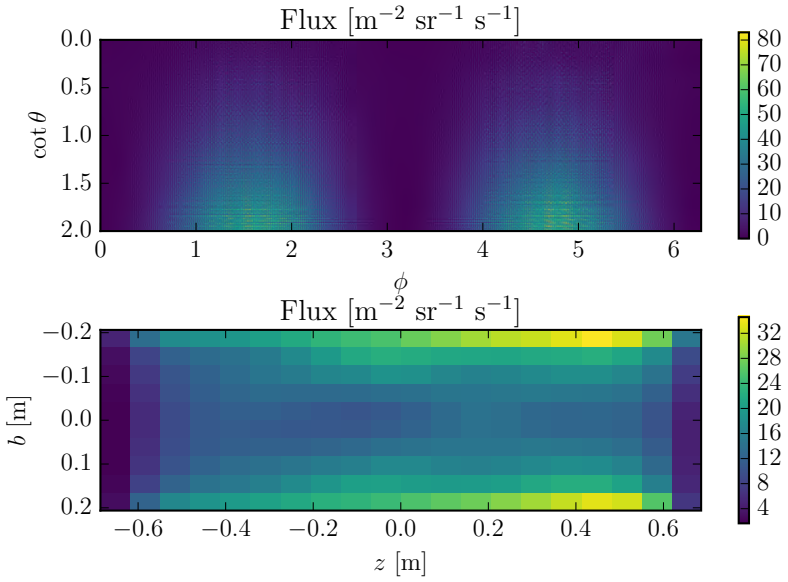


Figure 4.19: The flux observed by the detector in an average flat fielding run, summed over two of the four histogram parameters. The remaining two parameters are shown.

# Chapter Five: Imaging

## 5.1 Coordinate Systems

In order to discuss the imaging procedures, we will first need to lay a foundation for that discussion. The careful and consistent definition of coordinate systems allows several effective simplifications to be made in the imaging calculations.

The lab frame is a right handed coordinate system with $z$ defined to be in the upward vertical direction. Generally, lab $x$ is chosen to point East and lab $y$ is chosen to point North.

The detector frame is aligned with the detector, and is the frame in which all tracking is done. The x axis marks the start of the PMTs, and is at a seam inside the detector. The $z$ axis is along the axis of the cylinder of the detector, and points toward the electronics end. The detectors generally have $x$ and $y$ marked on them.

An orientation matrix $\mathcal{R}$ is used to describe the orientation of the detector. To build an orientation matrix, three basis vectors are constructed; the detector $x$ direction in the lab frame $\mathbf{x}_{\text{det}}$, the detector $y$ direction in the lab frame $\mathbf{y}_{\text{det}}$, and the detector $z$ direction in the lab frame $\mathbf{z}_{\text{det}}$. The matrix is constructed as [1]

$$\mathcal{R} = \begin{pmatrix} \mathbf{x}_{\text{det}} & \mathbf{y}_{\text{det}} & \mathbf{z}_{\text{det}} \end{pmatrix}. \tag{5.1}$$

For example, the standard vertical orientation, where detector $x$ is along lab $x$ (East), detector $y$ is along lab $y$ (North), and detector $z$ is along lab $z$ (up), we have

$$\mathcal{R}_{\text{v}} = \begin{pmatrix} 1 & 0 & 0 \\ 0 & 1 & 0 \\ 0 & 0 & 1 \end{pmatrix}, \tag{5.2}$$

and for the standard horizontal position, where detector $x$ is along lab $y$ (North), detector $y$ is along lab $z$ (up), and detector $z$ is along lab $x$ (East), we have

$$\mathcal{R}_{\text{h}} = \begin{pmatrix} 0 & 0 & 1 \\ 1 & 0 & 0 \\ 0 & 1 & 0 \end{pmatrix}. \tag{5.3}$$

[1] In the detector meta-files, the transpose is stored, to make it easier to enter the matrix as a single line.

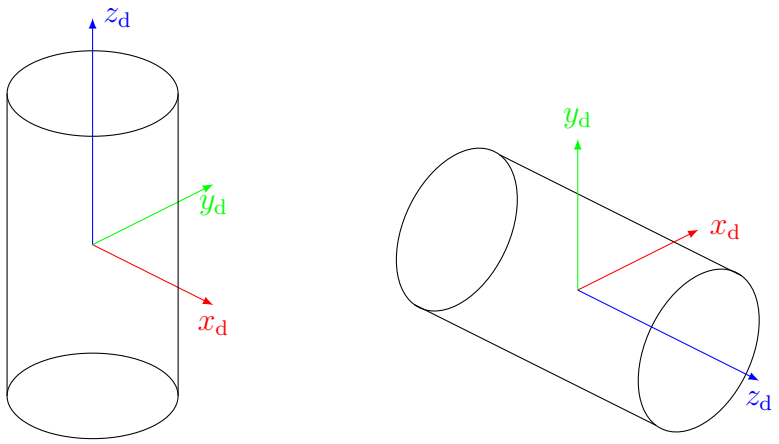


(a) Standard vertical orientation (b) Standard horizontal position

Figure 5.1: Cylindrical detector in different orientations.

To convert from one frame to another, this matrix or its transpose is used.[2] To convert, we can use

$$\mathbf{x}_\mathrm{det}\mathcal{R} = \mathbf{x}_\mathrm{lab}, \tag{5.4}$$

$$\mathbf{x}_\mathrm{lab}\mathcal{R}^T = \mathbf{x}_\mathrm{det}. \tag{5.5}$$

## 5.2 4-parameter Notation

Any ray can be described either by vector notation, $\mathbf{X}+t\hat{\mathbf{D}}$, or by four coordinates $\phi$, $\cot\theta$, $z$, and $b$ [47]. This notation will be called 4-parameter notation, and the other form will be called vector notation.

### 5.2.1 To 4-parameter Notation

To convert to this notation, we will need the signed track direction vector (chosen to always be in the positive $z$ direction)

$$\hat{\mathbf{u}} = \begin{cases} \hat{\mathbf{D}} & \text{if } \hat{\mathbf{z}}_\mathrm{d}\cdot\hat{\mathbf{D}} \geq 0 \\ -\hat{\mathbf{D}} & \text{if } \hat{\mathbf{z}}_\mathrm{d}\cdot\hat{\mathbf{D}} < 0 \end{cases} \tag{5.6}$$

[2]For a correctly formed rotation matrix, the columns will be orthogonal and $\mathcal{R}^{-1} = \mathcal{R}^T$

and the point of closest approach direction vector

$$\hat{\mathbf{b}} = \frac{\hat{\mathbf{u}} \times \hat{\mathbf{z}}_\mathrm{d}}{\sqrt{1 - (\hat{\mathbf{z}}_\mathrm{d} \cdot \hat{\mathbf{u}})^2}} \tag{5.7}$$

and the remaining orthogonal vector

$$\hat{\mathbf{t}} = \hat{\mathbf{b}} \times \hat{\mathbf{u}}. \tag{5.8}$$

Now, using these vectors, we can compute the 4-parameters,

$$\tan\phi = \frac{\hat{\mathbf{y}}_\mathrm{d} \cdot \hat{\mathbf{u}}}{\hat{\mathbf{x}}_\mathrm{d} \cdot \hat{\mathbf{u}}}, \tag{5.9}$$

$$\cot\theta = \frac{\hat{\mathbf{z}}_\mathrm{d} \cdot \hat{\mathbf{u}}}{\sqrt{1 - (\hat{\mathbf{z}}_\mathrm{d} \cdot \hat{\mathbf{u}})^2}}, \tag{5.10}$$

$$z = \frac{\hat{\mathbf{t}} \cdot \mathbf{X}}{\sqrt{1 - (\hat{\mathbf{z}}_\mathrm{d} \cdot \hat{\mathbf{u}})^2}}, \tag{5.11}$$

$$b = \hat{\mathbf{b}} \cdot \mathbf{X}. \tag{5.12}$$

Note that $\phi$ is defined on $[0, 2\pi)$ and that $\cot\theta > 0$. The sign of $b$ is used instead of allowing negative $\cot\theta$.

#### 5.2.1.1 To Vector Notation

The point of closest approach and direction vector can be constructed from these four parameters. This would be

$$\mathbf{X}_\mathrm{ca} = b\cos\left(\phi - \frac{\pi}{2}\right)\hat{\mathbf{x}}_\mathrm{d} + b\sin\left(\phi - \frac{\pi}{2}\right)\hat{\mathbf{y}}_\mathrm{d} + z\hat{\mathbf{z}}_\mathrm{d} \tag{5.13}$$

and

$$\mathbf{D} = \cos(\phi)\hat{\mathbf{x}}_\mathrm{d} + \sin(\phi)\hat{\mathbf{y}}_\mathrm{d} + \cot(\theta)\hat{\mathbf{z}}_\mathrm{d}. \tag{5.14}$$

Note that $\mathbf{D}$ is not a unit vector with this definition.

## 5.3 Plane Projection

### 5.3.1 Vector Approach

Projection on a surface at height $H$ using can be made by finding a point on the ray $\mathbf{X} + t\hat{\mathbf{D}}$, characterized by the scalar $t$, and with all basis vectors expressed in

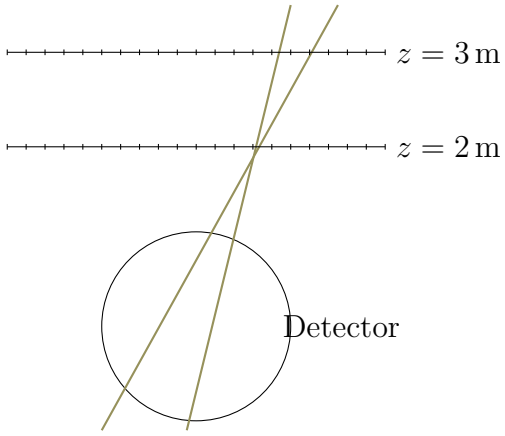


Figure 5.2: Projection of two tracks onto two different binned planes. The two tracks are "focused" into a single bin the 2 m plane, but are in different bins on the 3 m plane. If they are both attenuated tracks from a target at 2 m, the out of focus image on the 3 m plane is what we call our "shadowing" effect.

the projection plane's frame of reference. To find $t$, the point along the plane's basis vector $\hat{\mathbf{z}}$ where the ray intersects is:

$$t = \frac{H - X \cdot \hat{\mathbf{z}}}{D \cdot \hat{\mathbf{z}}}. \tag{5.15}$$

Then, the final coordinates on the plane $\mathbf{X}_p$ are

$$\mathbf{X}_p = \mathbf{X} + t\hat{\mathbf{D}}, \tag{5.16}$$

where only the $x$ and $y$ coordinates need to be computed, also called $h$ and $v$, respectively. As long as all calculations of $\hat{\mathbf{D}}$ and $\mathbf{X}$ use the plane coordinates, this works correctly for any orientation.

A histogram can be made using the $h$ and $v$ coordinates. After computing a ray, the contents of that 4D histogram bin is added to the 2D histogram cell. To represent the flux through each cell of this histogram, the per cell flux in the source histogram must also be added to a separate matching 2D weight histogram. The per cell flux is given in Equation 4.35. An illustration of this technique is shown in Figure .

This is the simplest description of the projection possible. However, the reconstruction can be made computationally faster[3] using a slightly different approach.

[3]Comparison made with multi-threading for both algorithms in C with OpenMP. Speedup varies on different architectures, from about 50% to about four times faster.

### 5.3.2 Fast Approach

Assume that we are working in the detector frame, and we have a plane in the detector frame with some relative orientation $R$ and location vector $\mathbf{C}$. The center of the bin parameters $\phi_i$, $\cot\theta_i$, $z_i$, and $b_i$ can be calculated and stored, along with the useful quantities $\sin\phi_i$, $\cos\phi_i$, and $\sqrt{1+\cot^2\theta_i}$. Since these are not correlated quantities, they only need to be calculated over the relevant bins.

First, the system should loop over the $\phi$ bins. Careful ordering of these loops provides significant calculation time improvements by avoiding repeating the most expensive calculations. Although we are going to calculate direction first, we need to calculate the first portion of the location of closest approach,

$$\mathbf{X}'_i = R \begin{bmatrix} \sin\phi_i \\ \cos\phi_i \\ 0 \end{bmatrix}. \tag{5.17}$$

Next, we leave this calculation and loop over the $\cot\theta$ variable. At this point, we fully know the direction, so we can project onto our plane from the center of the detector. We add the missing component to $\mathbf{X}'_i$,

$$X'_{z,i} = \mathbf{X}'_i \cdot \hat{\mathbf{z}} + (R \cdot \hat{\mathbf{z}}) \cdot \begin{bmatrix} 0 \\ 0 \\ \cot\theta_i \end{bmatrix}, \tag{5.18}$$

and then, as long as that is not zero[4], we can use that to project to the plane,

$$\mathbf{X}'_{pl} = \left( \mathbf{X}_d + X_d \cdot \hat{\mathbf{z}} \frac{\mathbf{X}' + R \cdot \hat{\mathbf{z}} \cot\theta_i}{X'_{z,i}} \right) \cdot \begin{bmatrix} 1 & 0 & 0 \\ 0 & 1 & 0 \\ 0 & 0 & 0 \end{bmatrix} \tag{5.19}$$

This is a two dimensional result; the third component of this equation should not be calculated. At this point, a cut can be made if the track misses the expected plane plus a penumbra equal to at most the length of the detector[5].

The quantities $\cot\theta_i \cos\phi_i$ and $\cot\theta_i \sin\phi_i$ can be computed at this point. The next loop is over $b$, allowing the values $b_i \cot\theta_i \cos\phi_i$ and $b_i \cot\theta_i \sin\phi_i$ to be stashed, as well.

[4]Zero if track is parallel to plane.

[5]An early version of the code missed this penumbra, causing missing tracks on the edges of the plane. Current versions do not currently make a cut here.

The final loop is over $z$, and at this point all the values are known. The final projection is

$$\mathbf{X}_{pl} = \mathbf{X}'_{pl} + R \cdot \begin{bmatrix} b_i \cot\theta_i \cos\phi_i + z_i \sin\phi_i \\ b_i \cot\theta_i \sin\phi_i - z_i \cos\phi_i \\ -b_i \end{bmatrix} \cdot \begin{bmatrix} -1 & 0 & 0 \\ 0 & 1 & 0 \\ 0 & 0 & 0 \end{bmatrix} \frac{1}{{X'}_{z,i}}. \tag{5.20}$$

Both of these algorithms are implemented in the `ctools` package, and they have C, Matlab, and Python bindings.

## 5.4 Validation

Two examples are presented here of this projection process; it the standard method for producing images from our detectors, and will continue to be used in later chapters.

### 5.4.1 Brick Targets

One of the most effective illustrations of the power of this process is from a simple study performed at UT with concrete and lead blocks. Two detectors were placed adjacent to each other in a lab under a 1 m thick concrete roof. After collecting a flat field, several lead bricks, $2 \times 4 \times 8$ in, were placed directly above each detector on a sheet of plywood. On the roof, concrete blocks were placed in a specific pattern above the center of the two detectors. The detectors were then run for 13 days. The resulting dataset can be projected through the different targets, resolving different images from the same dataset.

In Figure 5.3, two separate projection planes are shown. The bin size was adjusted for differing angular resolutions. The targets come into focus as the projection plane approaches them, and go out of focus as the plane leaves, creating a "shadowing" effect. The bins in the lower plane are 2 cm across, providing a high level detail, capturing the edges of the lead bricks effectively. The upper plane has larger bins, 6 cm square, and captures the larger concrete bricks.

The dead area of the detector can be seen in the lower image; this is the "blind cone" that is the result of the ends of the cylinder. The statistics drop at the edges of the lower histogram; this is due to each bin taking up a smaller solid angle as the distance from the detector increases. A larger bin size would improve these outer bins,

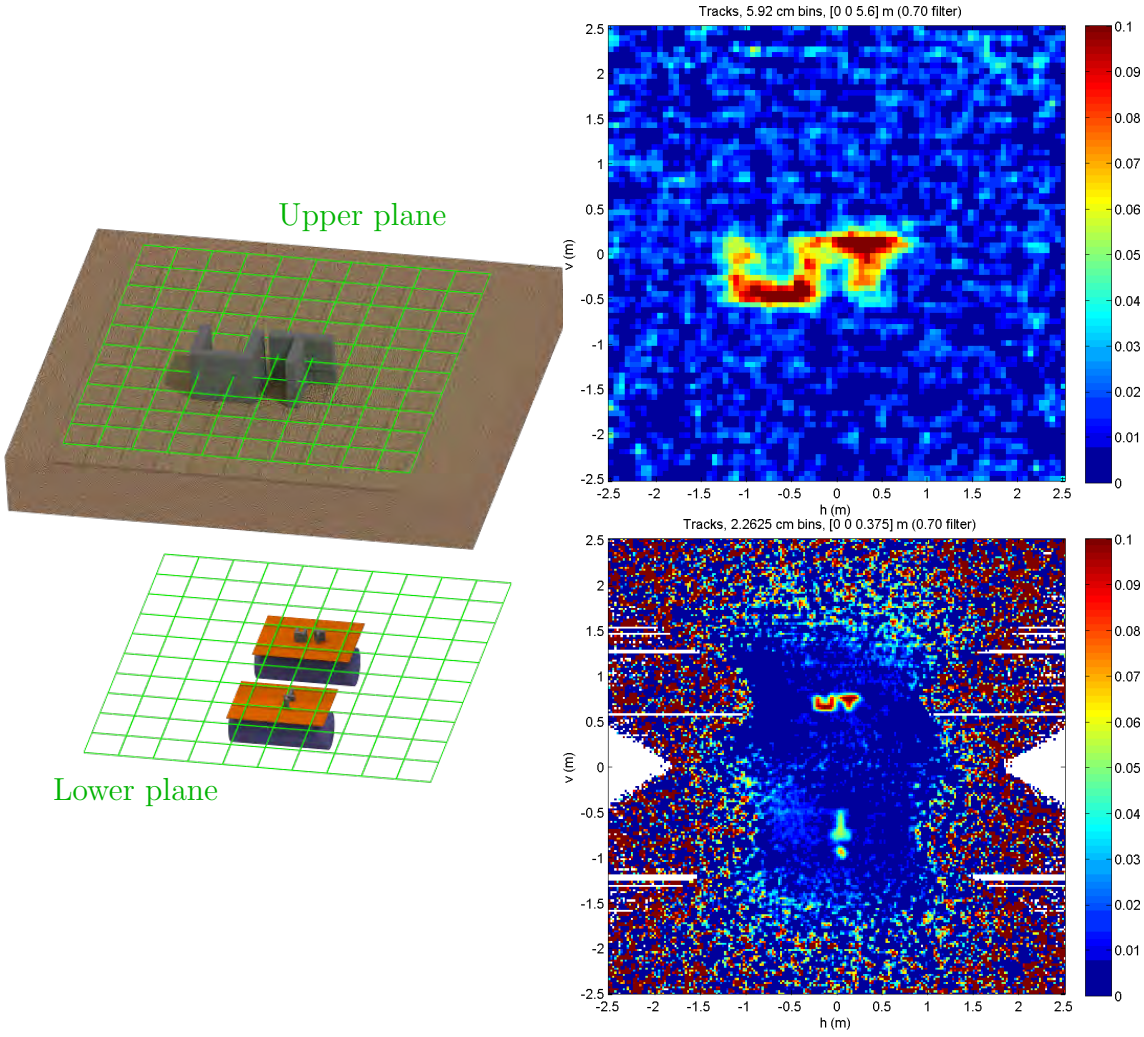


Figure 5.3: Projections at different heights. On the left, a to-scale illustration of the two detectors, plywood, bricks, and roof, along with the two projection planes, shown with a half meter grid. The upper image is 6.5 m above the detector center and captures the concrete bricks, and the lower image is 0.375 m above the detector and captures the lead bricks.

but would lose detail directly above the detector. Selecting a variable bin resolution along the individual axis would not be effective, due to the fact that the bin size of one axis cannot vary as a function of the other axis. A solution to this problem is presented in Section 5.5.

### 5.4.2 Sandia National Labs Study

The other example presented here is from a blind study done at Sandia National Labs (SNL) in 2010. A detector was placed horizontally on a track, and moved to 17 evenly spaced different positions down the center of a tunnel, running for two days at each position. There was approximately one meter of cement and top soil above the tunnel, and above that was a gentle slope. On this slope a variety of targets were placed to be imaged by the detector. By combining the data from multiple locations, a composite image was created that covered the entire active area of the experiment. The large number of locations gave excellent stereo information; by sweeping through the vertical axes, all the targets were found at their correct locations and heights (see Figure 5.4).

One target in particular had a particularly interesting structure; an arch created with a culvert and sandbags, visible around $h = -15\,\mathrm{m}$, and seen in detail in Figure 5.5. The excellent resolving power in the $z$ direction is due to the large amount of stereo information from the 17 detector locations.

One detail that was not resolvable, however, was the small sandstone block on top of the lead block on the far right of the image. The attenuation of the lead combined with the "shadowing" effect kept us from being able to resolve the brick. Vertical projection planes were tried as well, but were unable to prove there was a target on top of the lead block.

The final score card, created by SNL with our projection and their survey information, is seen in Figure 5.6.

## 5.5 Aside: Variable Resolution Binning

The histograms created thus far have primarily been evenly binned. However, due to the geometry of the projections, the count rates per bin can vary widely across the

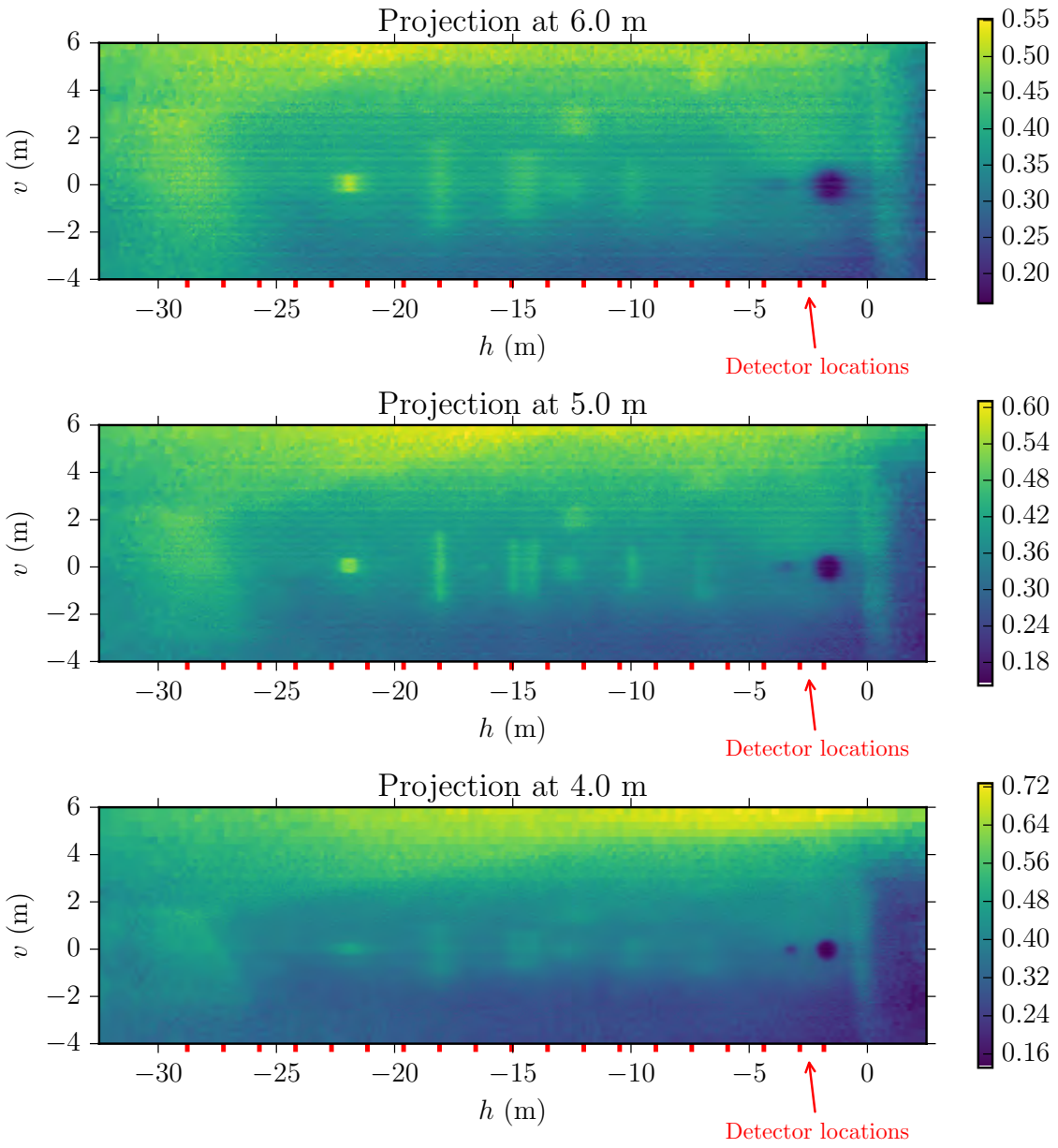


Figure 5.4: Three different projection planes, one meter apart, through the target area. The $h$ locations of the detector are marked; in $v$ the detector was centered at 0. The lowest projection (below) is out of focus through most of the image plane, except for the sharply defined round low attenuation structures (ventilation shafts) around $h = -2\,\mathrm{m}$. The next plane has clearly defined targets, and the previous structures are out of focus. The highest plane (top) has an extra target in focus, up the hill at $h = -7\,\mathrm{m}$.

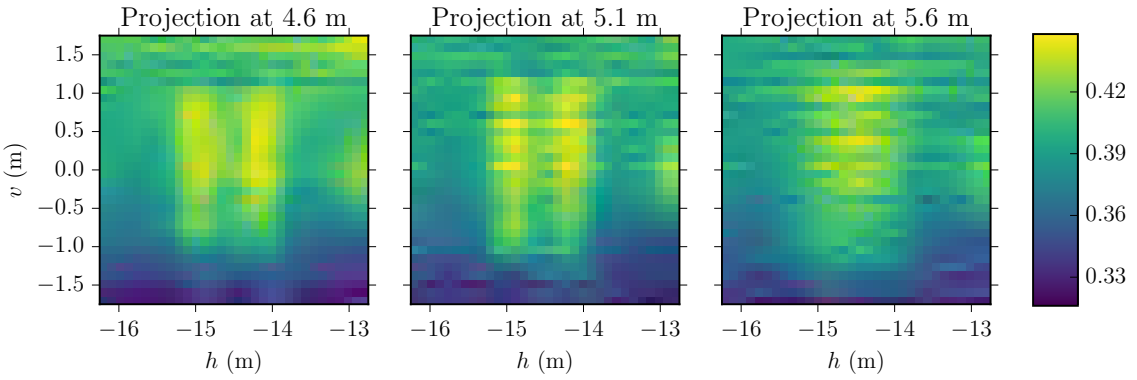


Figure 5.5: A closeup of a hollow culvert with sand bags piled on top, creating an arch. The lower projections (left) resolve the two sides separately, where as the higher projections (right) show the sides merge into one structure (the top of the arch).

histogram. A procedure for allowing dynamic bins size based on the error in each bin is presented here.

First, a high resolution histogram should be created, with dimensions that are divisible by two raised to some power $p$. The histogram should then be "shrunk" by combining bins $b_{i,j}$ to a new histogram $b'_{i,j}$, such that $b'_{i,j} = b_{2i,2j} + b_{2i+1,2j} + b_{2i+1,2j+1} + b_{2i,2j+1}$. This should be repeated $p$ times.

Then, the contents of the $4t$ cells of the original histogram should be replaced with $b'_{i,j}/4^t$ if the value of $b'_{i,j}/4^t < \frac{1}{\delta a^2}$, where $\delta a$ is the attenuation uncertainty cut and $t$ is the number of times the process has been done, from 1 to $p$. This provides a nearly constant uncertainty per bin, and supports the localized hit density over a central portion of a large plane that is common with projections near our detectors.[6]

This has provided an effective method to produce a single image that captures finer details near the detectors, while also preserving larger structures at large distances. This has eliminated the need to run several images at multiple resolutions for projections when using large planes near the detectors. For example, in Figure 8.1 in Chapter 8, it was not previously possible to study the entire strip of bricks in a single image.

[6]This algorithm is implemented in `muview` and can be used by running the method `.constant_unc(`$\delta a$ `= 0.01)` on a `Plane` instance that has already been projected.

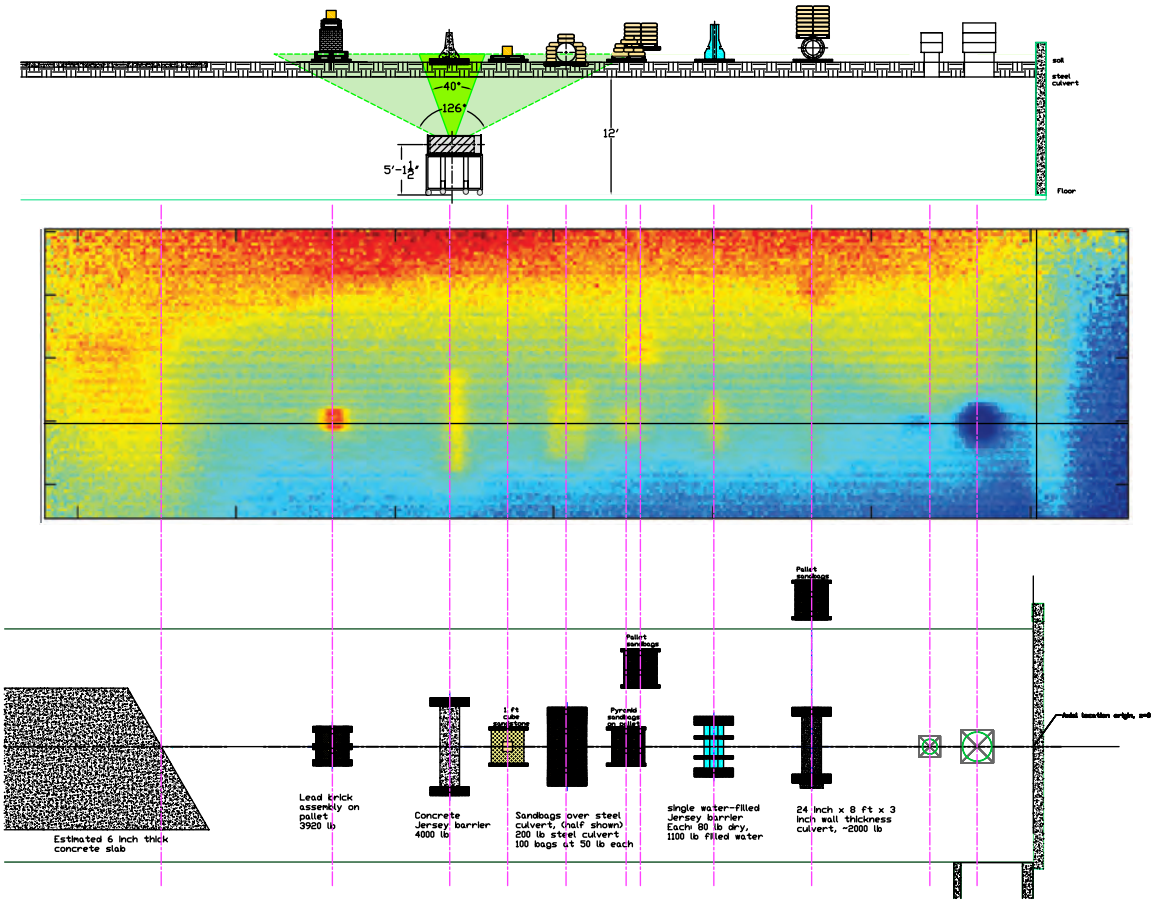


Figure 5.6: The score card from the Sandia National Labs (SNL) study. The image was projected through the targets. Targets and annotations added by SNL. Notice that details of the tunnel that were not originally intended to be part of the study are visible, too; the concrete slab on the left, the ventilation shafts on the right, and the end of the tunnel just to the right of the shafts.

## 5.6 Other Projections

The original method can be extended to cylinders and spheres relatively easily. For a cylinder, we can start with the intersection of the track with a circle in two dimensions. As in the first discussion, the vectors will be taken to be in the final coordinate frame (for the cylinder). The radius of the cylinder being projected to is $r$, and the length is $\ell$. It is oriented along the $\hat{\mathbf{z}}$ direction. We need the point of closest approach to the axis,

$$\hat{\mathbf{X}}'_c = \hat{\mathbf{X}}' + \frac{\mathbf{X}' \cdot \hat{\mathbf{D}}'}{\hat{\mathbf{D}}' \cdot \hat{\mathbf{D}}'} \hat{\mathbf{D}}', \tag{5.21}$$

where the primes indicate that these are just the first two components, along $\hat{\mathbf{x}}$ and $\hat{\mathbf{y}}$. Then, we have

$$t = \pm\sqrt{r^2 - \mathbf{X}'_c \cdot \mathbf{X}'_c}, \tag{5.22}$$

where only the $t$ value with the larger $z$ coordinate for the point of intersection should be selected, and no real solutions indicate a missed track. The remainder of the calculations are the same as Section 5.3.1. The image histogram will be binned over $\phi$ and $z$, with appropriate limits on $z$. All of the details of the detector location and the plane location are handled by the coordinate transforms into D and X in the plane frame.

For sphere projections, the only changes are in the point of closest approach,

$$\hat{\mathbf{X}}_c = \mathbf{X} + \frac{\mathbf{X} \cdot \hat{\mathbf{D}}}{\hat{\mathbf{D}} \cdot \hat{\mathbf{D}}} \hat{\mathbf{D}}, \tag{5.23}$$

and the selection of $t$,

$$t = \pm\sqrt{r^2 - \mathbf{X_c} \cdot \mathbf{X_c}}, \tag{5.24}$$

where we are using all three components of the point of closest approach, and appropriate binning parameters should be chosen.

Projections can also be made to voxels. This system is closely related to the planer projections, though without applying the optimizations suggested by Amanatides and Woo [48], it would be significantly slower.

## 5.7 New Reconstruction Method

### 5.7.1 Muon Attenuation

We will start with a model based on our understanding of muons, proposed by Reyna [32],

$$\frac{d\Phi_\mu}{dp_\mu} = \cos^3\theta I_v\left(p_\mu \cos\theta\right).$$

Since the attenuation is proportional to the component of the muon's momentum perpendicular to the surface, we can obtain a model for the attenuation

$$D_{\mu t} = -\ln\left(\frac{n_t}{Rf_t}\right) = \int_t P\frac{dz}{16 \text{ mwe}} = k\left(\Delta z\right). \tag{5.25}$$

This means that, to a good approximation, the attenuation is proportional to the vertical displacement through a voxel times its "density" factor of $k$. This simple model will be the basis for our work.

### 5.7.2 Expected Tracks

We will use the subscript $v$ to indicate the volumes, $t$ to indicate tracks, and $vt$ to indicate the volumes that a single track hits. We can assume that the expected tracks $\lambda_t$ will be exponentially decaying as

$$\lambda_t = e^{-\sum_v k_v z_{vt}} Rf_t, \tag{5.26}$$

where $k_v$ is the number proportional to the density in the volume that we are trying to find, $z_{vt}$ is the track's distance through the cube vertically, $R$ is a normalization constant, and $f_t$ are the expected flat field counts. $R$ is a normalization constant defined as

$$\sum_t n_t = R\sum_t f_t, \tag{5.27}$$

where $n_t$ are the observed counts. This normalization will keep $k_v$ small, so that we can use the Taylor expansion in $k_v$,

$$\lambda_t \approx \left(1 - \sum_v k_v z_{vt}\right) Rf_t. \tag{5.28}$$

### 5.7.3 Likelihood Analysis

The likelihood function for our observed counts is defined as

$$F = -\ln \mathcal{L} = -\ln \prod_t P_{n_t}(\lambda_t) = -\sum_t (n_t \ln \lambda_t - \lambda_t - \ln n_t!),$$

where $P_n(\lambda) = \frac{\lambda^n e^{-\lambda}}{n!}$ is a standard Poisson distribution that gives us probabilities for our expected values $\lambda_t$ in $n_t$. For the moment, we will ignore the term that does not include $\lambda_t$,

$$F \approx \sum_t (\lambda_t - n_t \ln \lambda_t).$$

Since we need to maximize the likelihood, we'll want to minimize $F$ with respect to our values for $k_v$, or

$$\frac{\partial F}{\partial k_v} = \sum_t \frac{\partial \lambda_t}{\partial k_v}\left(1 - \frac{n_t}{\lambda_t}\right) = 0.$$

Since $\frac{\partial \lambda_t}{\partial k_v} = -z_{vt}\lambda_t$ from our earlier definition, we can find that we need to solve

$$\sum_t z_{vt}(\lambda_t - n_t) = 0.$$

Using our Taylor series expansion (5.28), we can write out the part in parenthesis as

$$\lambda_t - n_t = Rf_t - \sum_{v'} k_{v'} z_{v't} Rf_t - n_t,$$

where primes were added to the summation over $v$. Now, our equation to solve becomes

$$\sum_t z_{vt}\left(Rf_t - \sum_{v'} k_{v'} z_{v't} Rf_t - n_t\right) = 0,$$

$$\sum_t z_{vt} Rf_t - \sum_t \sum_{v'} k_{v'} z_{vt} z_{v't} Rf_t - \sum_t z_{vt} n_t = 0,$$

$$\sum_{v'} k_{v'} \sum_t z_{vt} z_{v't} Rf_t = \sum_t z_{vt}(Rf_t - n_t).$$

Now, with a few definitions to clean up the notation:

$$M_{v'v} = \sum_t z_{vt} z_{v't} Rf_t, \tag{5.29}$$

$$d_v = \sum_t z_{vt} \left( R f_t - n_t \right), \tag{5.30}$$

our equation becomes

$$\mathbf{Mk} = \mathbf{d},$$

which has the solution

$$\mathbf{k} = \mathbf{M}^{-1}\mathbf{d}.$$

Given the volume is divided up into $i$, $j$, and $k$ divisions, the extent of the covariance matrix $\mathbf{M}$ is $ijk$ by $ijk$. This can be difficult to do quickly; a 10,000 by 10,000 matrix takes about 2 minutes to invert in Matlab, and 10,000 is somewhat small for a reasonable system.

There are other considerations, too; this does not discuss material outside the volume that intersects rays, and does not go into the ray-tracing necessary to build the sums over $t$. Material outside the area will be avoided for the purposes of this study; expanding to data sets that have this issue is important for later work, but we currently have several data sets without significant surrounding material.

An example of the projection compared with the new system is given in Figure 5.7. A significant improvement in the localization of the density is clearly seen.

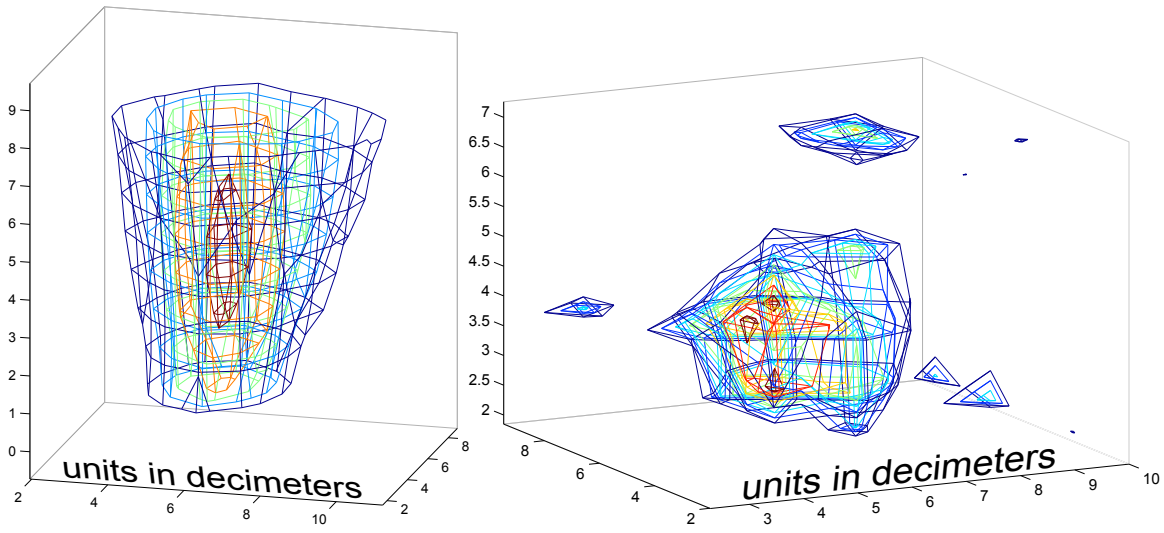


Figure 5.7: On the left, a plot of a series of stacked planes. The lines are meshes made of constant attenuation surfaces. On the right, the same data is used for a volumentric reconstruction. The data was a 20 cm lead cube directly above the detector. The volumetric reconstruction does a much better job of localizing the attenuation in the $z$ direction.

# Chapter Six: Simulation

## 6.1 Cosmic Ray Generation

To improve our understanding of how the cosmic rays interact with our detector, a Monte Carlo simulation was developed. This required several tools, including spectrum generation, a geometric description of our strips, and a data-driven model of the response of the PMT response.

### 6.1.1 Log Gaussian Distribution

Muon counting rates can be estimated from the parameters of the detector listed previously and an analytic model of the muon spectrum. The current model is based on the work of Reyna [32], and is described in Chapter 2.

To efficiently generate this spectrum for Monte Carlo, a simple and effective approximation can be used, as originally proposed in a project note [30]. If we make the substitution $y = \ln \zeta$, then the Reyna model becomes:

$$\frac{d\Phi_\mu}{dp_\mu} = \cos^2\theta \zeta I_V(\zeta), \tag{6.1}$$

and then we can approximate the product $\zeta I_V(\zeta) \approx I_0 L(\bar{y}, \sigma_y)$ by a log Gaussian distribution with median $\bar{y} = 0.9046$ and standard deviation $\sigma_y = 1.0806$. The scaling factor $I_0$ is $88.0\,\mathrm{m}^{-2}\mathrm{s}^{-1}\mathrm{sr}^{-1}$.

The tracks are most effectively generated if they fill a cylindrical space around the detector. Other Monte Carlo systems use a planar space above the detector, but this wastes a huge portion of the processing time tracking rays that are point to go through the detector (even with multiple scattering). To do this, the following procedure is used.

First, we generate the $\cos^n\theta$ spectrum by generating a random number $\mathcal{U}$ in the range $[0, 1]$, such that

$$\{\cos\theta_\mu\} = \left\{\mathcal{U}^{1/(1+n)}\right\}, \tag{6.2}$$

where in this case the power $n$ is $n = 2$, and the 1 being added is from area element $\cos\theta\, d\theta\, d\phi$.

Then generate $\zeta$ from a log Gaussian distribution with the parameters listed above. The muon momentum is then $p_\mu = \zeta / \cos\theta_\mu$.

Then, generate the azimuthal angle $\phi_\mu$ by selecting a random value in the range $[0, 2\pi]$. The direction of the momentum is then just the combined vector in terms of these angular components,

$$\hat{\mathbf{n}} = \left\langle \begin{array}{c} \sqrt{(1-\cos^2\theta_\mu)\sin\phi_\mu} \\ \sqrt{(1-\cos^2\theta_\mu)\cos\phi_\mu} \\ \cos\theta_\mu \end{array} \right\rangle . \tag{6.3}$$

The final momentum vector is then created out of the normalized direction and the magnitude previously calculated, $\mathbf{p} = p_\mu \frac{\mathbf{n}}{|n|}$.

### 6.1.2 Recovering Reyna's Spectrum

It is possible to recover an exact spectrum from this distribution using rejection sampling. If we take the original spectrum $f(x)$, in this case our log Gaussian, and our new expected spectrum $g(x)$, in this case, Reyna spectrum, we can recover the spectrum by introducing an acceptance probability:

$$\mathbb{P}\left(\frac{f(x) - g(x)}{f(x)} < U\right), \tag{6.4}$$

where $U$ is from the uniform distribution,

$$U \sim \text{Unif}(0, 1), \tag{6.5}$$

which will allow us to use rejection sampling effectively. This is subject to the condition that $f(x) > g(x)$, or it will simply become the probability distribution of $f(x)$ again. Minor violations in this condition in the large $p$ limit are acceptable.

### 6.1.3 Spacial Distribution

To generate the spacial spacing of the track, we define a rectangular plane that is perpendicular to the direction of the track. The length of the rectangle is $L'$ along the $\hat{\mathbf{y}}'$ direction, and the width of the rectangle is $2R'$ along the $\hat{\mathbf{x}}'$ direction. This gives the plane a constant area $A = 2L'R'$. Note that the rectangle includes a penumbra, where $L'$ is the length of the detector plus twice the penumbra $L' = 2p + L$ and $R'$

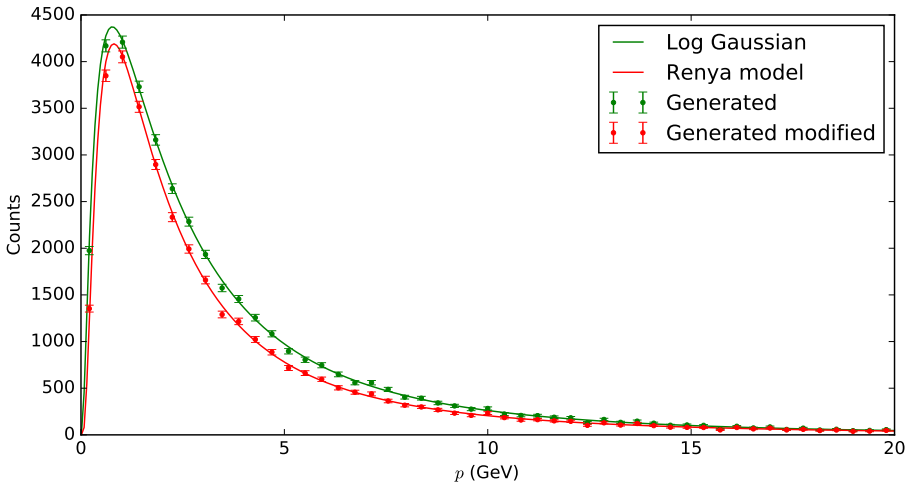


Figure 6.1: Recovering the Reyna distribution from the log Gaussian. The points are from 40,000 generated $p$.

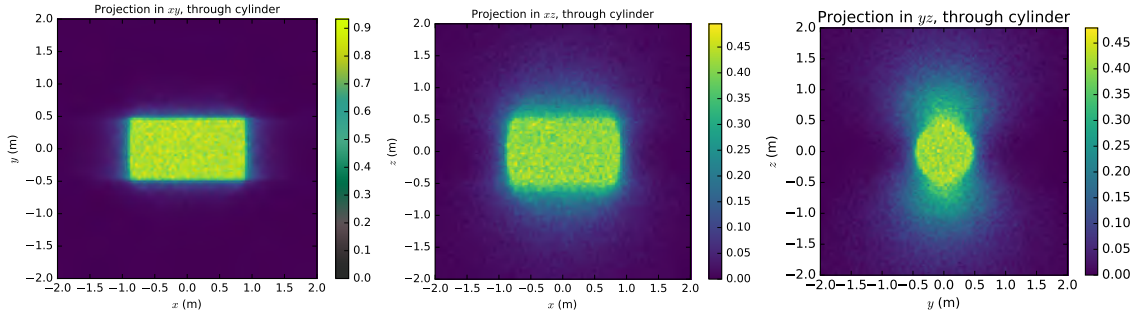


Figure 6.2: Filling space with a cylindrical distribution. The penumbra was 20 cm, and the axis was along $x$. The $z$ direction was vertical. The color values are arbitrary flux units. 1,000,000 rays were generated.

is the radius of the detector plus the penumbra $R' = R + p$. The penumbra is an extra space around the detector that is chosen based on multiple scattering and the dimensions of the target. To correctly orient the plane of generated tracks, the basis vector $\hat{\mathbf{x}}'$ should be chosen such that $\hat{\mathbf{z}}_{\text{det}} \times \hat{\mathbf{x}}' = 0$ and $\mathbf{p} \times \hat{\mathbf{x}}' = 0$. The second basis vector should also be perpendicular to the track $\mathbf{p} \times \hat{\mathbf{y}}' = 0$ and the first basis vector. This ensures that the cylindrical space around the detector is uniformly sampled (see Figure 6.2). The frequency of the generated tracks is $f = \frac{2}{3}\pi A I_0$.

Using a given spectrum, it is possible to predict an ideal counting rate for a perfectly efficient detector. Assuming sea level rates, and a minimum cutoff on detected tracks of 0.2 GeV, the expected track frequency would be:

$$\dot{n} = \int_{A_\perp} dA_\perp \int d\Omega \int_{0.2\,\mathrm{GeV}}^{\infty} dp_\mu \frac{d\Phi_\mu\left(p_\mu, \theta\right)}{dp_\mu}. \tag{6.6}$$

With the spectrum and values given above, along with the detector geometry and histogram cuts, the results from a simulation is 106 Hz for a horizontal orientation, or 60.9 Hz for a vertical orientation.

## 6.2 Handling the Strips

Two of the three layers in our detector are made of helical strips, which are not readily available in simulation toolkits and provide a few challenges in computing intersections in 3D.

### 6.2.1 Forward Calculation

Given a cylinder of length $\ell$, a layer can be described by the number of strips $n$, the radius to the center of the layer $R$, the thickness of the layer $T$, the physical width of a single strip $W$. The strips can be placed using the angle of the center of the strip with respect to the detector $x$ axis $\phi$, and the wrap angle $\Omega$. The $i$ subscript has been dropped for clarity, it is implied for the current layer.

The coordinates are chosen so that the center of the detector is at the coordinate origin, and the axis of the detector is along the $z$-axis. The angle of the strips is measured from the $x$ axis. See Figure 6.3.

Given a pair of vectors describing a line, $\mathbf{X} + t'\mathbf{D}$, we want to construct the strips hit by that line. We can redefine these vectors using the closest approach

$$\mathbf{X}_{\mathrm{ca}} = \mathbf{X} - \left(\frac{X_x D_x + X_y D_y}{D_x^2 + D_y^2}\right)\mathbf{D} \tag{6.7}$$

and the unit direction vector, $\hat{\mathbf{D}} = \frac{\mathbf{D}}{\sqrt{\mathbf{D}\cdot\mathbf{D}}}$ . We can further require that the $z$ component of the unit direction vector be negative, so we always have a downward traversing ray, without losing any generality. We can write our line in the simpler form

$$\mathbf{X}(t) = \mathbf{X}_{\mathrm{ca}} + t\hat{\mathbf{D}} \tag{6.8}$$

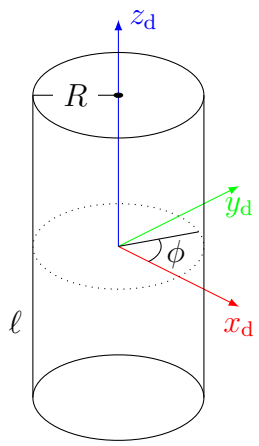


Figure 6.3: Cylindrical detector coordinate vectors.

#### 6.2.1.1 Infinite Cylinder and Line Intersection

If the line intersects an infinite cylinder with a finite width, we can call the entry and exit points $t_{\mathrm{outer},1}$, $t_{\mathrm{inner},1}$, $t_{\mathrm{inner},2}$, and $t_{\mathrm{outer},2}$ (see Figure 6.4). The cylinder is centered at the origin, and aligned with the $z$-axis, so, by symmetry, we can write $t_{\mathrm{outer},2} = -t_{\mathrm{outer},1} = t_{\mathrm{outer}}$ and $t_{\mathrm{inner},2} = -t_{\mathrm{inner},1} = t_{\mathrm{inner}}$.

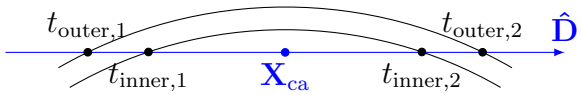


Figure 6.4: Line intersection with cylinder.

The radii of the two cylinders that are intersected are $r_{\mathrm{inner}} = R - \frac{T}{2}$ and $r_{\mathrm{outer}} = R + \frac{T}{2}$.

In the first two dimensions, this is simply a circle intersection. So, to find the values of $t$, we can use

$$(t_i)_{xy} = \sqrt{r_i^2 - (X_{\mathrm{ca}})_{xy}^2} = \sqrt{r_i^2 - (\mathbf{X}_{\mathrm{ca}} \cdot \hat{\mathbf{x}}_{\mathrm{d}})^2 - (\mathbf{X}_{\mathrm{ca}} \cdot \hat{\mathbf{y}}_{\mathrm{d}})^2} \tag{6.9}$$

where $i$ is inner, outer, and $xy$ indicates that this is a two dimensional vector. We will require the part inside the square root to be positive; this will remove rays that miss the cylinder entirely.

We have to convert $t$ back to use it for our three dimensional vectors, so we take

$$t_i = \frac{(t_i)_{xy}}{\sqrt{\left(\hat{\mathbf{D}} \cdot \hat{\mathbf{x}}_{\mathrm{d}}\right)^2 + \left(\hat{\mathbf{D}} \cdot \hat{\mathbf{y}}_{\mathrm{d}}\right)^2}} \tag{6.10}$$

Now we have the active portions of the line in the cylinder between $t_{\mathrm{inner}}$ and $t_{\mathrm{outer}}$. The following will split the active portion and look at each part separately, from $t_1$ to $t_2$.

Notice that if the line is parallel to the $z$-axis, there will not be a cylinder intersection; however, we are only interested in tracks that can reconstruct or nearly reconstruct, and that requires a significant $x$ or $y$ component to satisfy the $\cot\theta$ cut.

#### 6.2.1.2 Endcaps

The endcaps of the cylinder can be described as an infinite plane; the $t$ value of the intersections can be found as

$$t_{\pm} = \frac{z_{\pm} - \mathbf{X}_{\mathrm{ca}} \cdot \hat{\mathbf{z}}_{\mathrm{d}}}{\hat{\mathbf{d}} \cdot \hat{\mathbf{z}}_{\mathrm{d}}} \tag{6.11}$$

where $z_{\pm} = \pm\frac{\ell}{2}$, and $t_{\pm}$ refer to the $t$ intersection value for the upper and lower plane, respectively. This can be used to reduce the range of interest $[t_1, t_2]$ to $[t_1, t_2] \cap [t_+, t_-]$. If this intersection is zero, the line missed the strips active area for this range of $t$. If there is a nonzero intersection, that will now be referred to as $[t_1, t_2]$.

#### 6.2.1.3 Strips

To calculate strips hit and path lengths in the strips, we will make the following simplification. We will assume that the strips have a curved shape that conforms with the cylinder, and that the width of the strips is defined by the width along the curvature of the cylinder. Since $R \gg W/2$, this is close to the actual width. See Figure 6.5 for an example.

Now, we will make a change of coordinates. Given any point described by Equation 6.8, we can find the distance to the $z$-axis as $r = \left|(\mathbf{X}(t))_{xy}\right|$. Given the center of a strip at height $z$,

$$\phi(z) = \phi + \frac{z\Omega}{\ell} \tag{6.12}$$

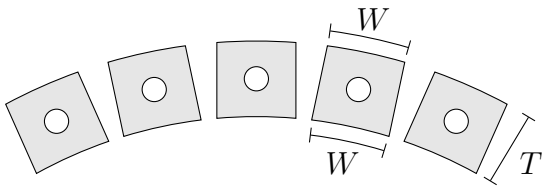


Figure 6.5: Strip dimensions.

we can take the distance from the center of the strip to the point around the circumference of a cylinder at radius $r$. The angular distance is, taking care to use the arctangent carefully for $x < 0$ and wrap around,

$$\Delta\theta = \tan^{-1}\left(\frac{\mathbf{X}(t)\cdot\hat{\mathbf{y}}_{\mathrm{d}}}{\mathbf{X}(t)\cdot\hat{\mathbf{x}}_{\mathrm{d}}}\right) - \phi\left(\mathbf{X}(t)\cdot\hat{\mathbf{z}}_{\mathrm{d}}\right) \tag{6.13}$$

and the corresponding distance along the circumference of the cylinder is

$$w = r\Delta\theta \tag{6.14}$$

This can be computed for both points, $t_1$ and $t_2$ to give $w_1$ and $w_2$. Assuming the line forms a nearly straight line in these coordinates, that is, $\frac{d\theta}{dt}$ is nearly constant over the range allowed for $t$, we can find the total distance traversed as $\Delta w_{\mathrm{total}} = w_2 - w_1$, as well as the length of the portion of the line traversed in the strip $[w_1, w_2]\cap[-W/2, W/2]$ and calling that $\Delta w_{\mathrm{strip}}$, we can write the path-length in the strip as

$$t_p = \frac{\Delta w_{\mathrm{strip}}}{\Delta w_{\mathrm{total}}}\left(t_2 - t_1\right) \tag{6.15}$$

This assumption is reasonable for the ranges of direction vectors allowed, and the thin strip layers.

The distance to the photomultiplier tubes (PMTs), $\zeta$, since the readout is on the positive $z$ end of the detector, is

$$\zeta = (1.1)\,\frac{L}{2} - z \tag{6.16}$$

where $z$ is the average $z$ value in the strip. The factor here accounts for the extra length to the PMTs from the strip end.

### 6.2.2 Segmented Strips

The inner and outer layer of helical strips can be approximated as a segmented polygonal structure. The vertices of this structure are along the actual strip edges,

with the segments in-between being linear triangular surfaces. At some distance $z$ from the end, the four strip corners can be described using

$$\phi_{s,i}(z) = \phi_s, 0 + i \cdot \Delta\phi_s + \frac{z}{L}\omega_s \pm \Delta\phi_s, \tag{6.17}$$

$$r_{s,i} = R_s \pm \frac{T}{2}. \tag{6.18}$$

The distance $z$ is split into twenty even divisions along the strip, and then the faces are built using carefully selected counter-clockwise sets of strips.[1] The top and bottom face are planar, but the side faces are not, which is a requirement for four-vertex faces (often called quads) in some ray tracing systems like the one in Geant4 [49]. To make three-vertex faces, the counter-clockwise loop of vertices labeled $1, 2, 3, 4$ can be split into two sub-loops, $1, 2, 3$ and $2, 3, 4$.

This process can be extended to add a small square hole in the interior of the faces, using the same machinery with a smaller strip thickness and the opposite direction in the vertex loops. The end-caps become four separate planer faces connecting the outer faces with the hole. This hole approximates the reduced scintillation efficiency of the fiber and air running down the center of the strip.

## 6.3 Attenuation in the Fibers

The attenuation from the strips, seen in the data in Figure 6.6, can be modeled using a simple exponential. Given the path-length in the strip, $t_p$, and the distance to the end of the strip $\zeta$, we can define the attenuation constants as $a_{s0}$, $a_\ell$, $a_b$, and $a_t$, and then the intensity at the end of the strip, $I$, is

$$I = t_p a_{s0} e^{-\frac{\zeta}{a_\ell}} \tag{6.19}$$

This intensity can be used to find

$$\sigma = a_{s0}\sqrt{1 + \frac{I}{a_b}} \tag{6.20}$$

We can compute the trigger efficiency $T$ as

$$T = \frac{1}{2}\text{erfc}\left(\frac{a_t - I}{\sqrt{2}\sigma}\right) \tag{6.21}$$

[1] The direction faces are build in ray-tracing software usually controls the direction of the normal to the face, which should face outward from the object.

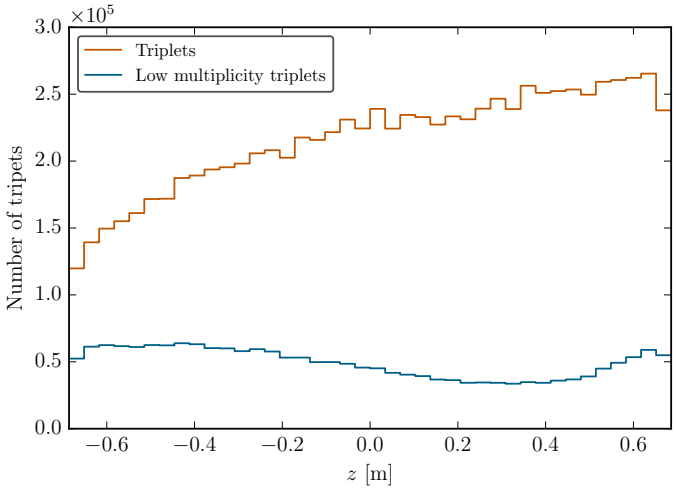


Figure 6.6: Number of triplets over 40 bins along detector $z$ before full reconstruction. The $z$ coordinate of each triplet is used. The low multiplicity triplets are from triplets with less than 10 strips involved.

To test this, we can compute the comparison between the $z$ and $b$ bins (summing over the other two dimensions).

## 6.4 Digital Electronics Simulation

To calculate the probability of a strip hit registering a PMT hit, the following procedure can be used. The energy deposited in a strip, $E_0$, is attenuated through the simple model to the energy observed at the PMT, $E = E_0 e^{-z_{\text{eff}}/\ell}$, where the effective attenuation length $\ell = 2.7\,\text{m}$ is a characteristic of the strips, and the effective distance down the strip, $z_{\text{eff}}$, is the actual distance along the strip to the PMT, and is related to the $z$ location of the hit through the layer's helicity. At the PMTs, the light in the strip may trigger a hit with a probability:

$$P = \frac{1}{2}\text{erfc}\left(\frac{A - B\,E}{s\sqrt{2}}\right), \tag{6.22}$$

where $s$ is the signal, $\sqrt{1 + B\,E/C}$. The three constants $A = 24$, $B = 35$, and $C = 0.15\,\text{MeV}$ were chosen to provide a response in the $b$-$z$ plane that provided the best fit to the data.

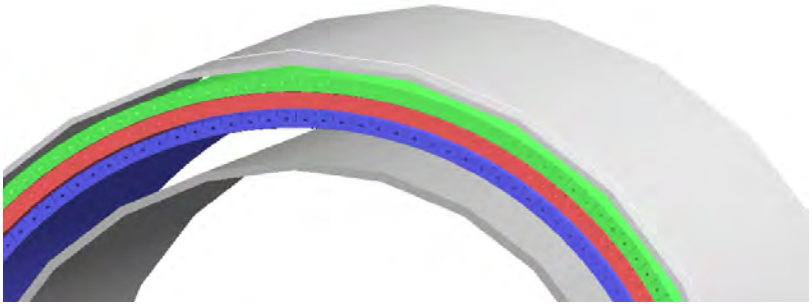

Figure 6.7: Model of detector components used in simulations. The inner piece is there to approximate the internal components of the detector.

For each channel on the PMTs, a portion of the signal is collected on the neighboring channels, constituting cross-talk. When measured with similar 1.2 mm fibers for the MINOS experiment by Lang [50], there was 5% signal sharing on nearest neighbor channels that share an edge, and less than 1% signal on the diagonal neighbors.

To include cross-talk between PMTs in the simulation, after the probability is calculated above, a hit cell has 20% of its probability applied to channels with which it shares an edge, and 2% applied to channels that share a corner. To fully model the reconstruction system, there is also a contribution to the probability from random events. The random trigger rate was 0.6% on FEBs that contained one or more hits, and 0% for FEBs that did contain a real hit. These probabilities $p$ are added to the strip trigger probability $P$ calculated from the attenuated strip energy deposition from the tracks in the scintillator using $P' = p(1 - P)$.

These fits were arrived at by carefully matching the behavior of a real detector, such as the strip groupings listed in Section 4.6. The histograms for each of the parameters, as well as the correlations visible in the $bz$ histogram, all had to match the actual data collected in both horizontal and vertical orientations. For these comparisons, the log Gaussian distribution was used with no targets present.

## 6.5 Geant4 Monte Carlo Simulation

A simulation was built using the above methods and parameters. The system was built using the Geant4 toolkit [51], [52], version 10.2, and links to the analysis package for the strip reconstruction. The system was both multithreaded and MPI enabled,

allowing massive parallelization to be applied. The helical strips were modeled by dividing them into 20 divisions, and modeling each as four nearly rectangular external faces and four nearly rectangular internal faces. The external covering was a 4 mm thick aluminum cylindrical shell just outside the outer strip layer. The internal components of the detector were approximated by a 6 mm thick hollow cylinder placed inside the detector; this was chosen to match the mass of the internal components. See Figure 6.7.

### 6.5.1 Organization

The structure of the program can be seen in Figure 6.5.1. The main function sets up the physics lists and the detector construction, which are used by all threads. The action initialization class sets up runs, with a primary generator (muon gun) and event action (printing status per event). The run class handles several of the per-event codes, such as energy deposition and tracking.

Options are handled through Boost's program options library [53], and are read in from an `ini` file. A `gdml` file, in Geant's geometry description markup language, is read in for custom geometries, so that different targets and orientations can be simulated without recompiling the program.

Separate executables are created by CMake [54] from the one `MuSim.cc` file. The sequential version MuSimSeq runs without threads. The standard MuSim will run with threading enabled. The MuSimMPI executable should be run with MPI. MuSimGUI will present a graphical user interface and will provide visual feedback for the model and simulation. Note that CMake will not produce some of these if your system does not have the prerequisites for their creation.

### 6.5.2 Options

The simulation supports a variety of options through the `ini`-file configuration. All of these options can also be passed in through the command-line, as well, where they will override the option in the `ini`-file. The parameters are automatically generated from a space separated file using a python script. The script updates the header file, source file, and default `ini` file automatically. The simulation stores all it's current parameters, as well as the current geometry, in both the `root` and `hdf5` output files.

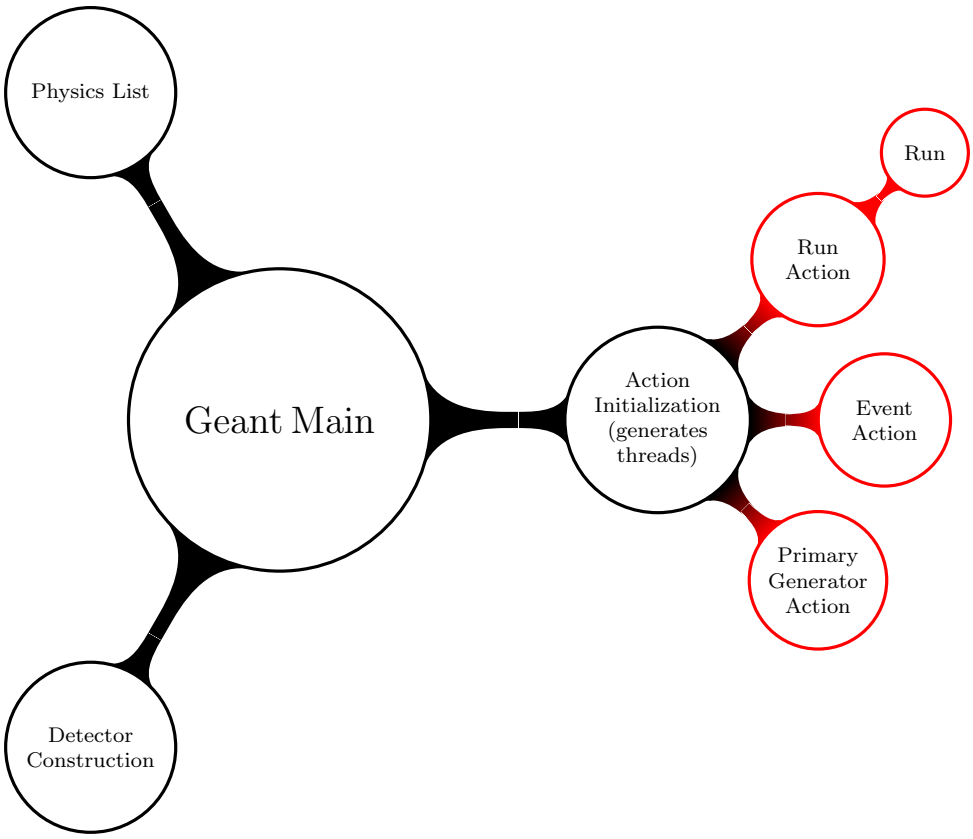


Figure 6.8: Primary Geant classes and their relationships.

### 6.5.3 Uses

This simulation has provided a deeper understanding of our detector and its interaction with cosmic rays. Results from this simulation have given us a prediction of the threshold momentum seen in Chapter 4. These results have also enabled an absolute measurement of the spectrum with the efficiency estimation seen in Section 10.4.

# Chapter Seven: Tracking Code

UDAQ is a C++11 library made of a collection of classes in the `Mu::` namespace, along with several helper functions and SWIG generated bindings [55] for Python. The primary purpose of this chapter is to outline the code that is used in the tracking algorithms.

Most of the classes support conversion to a string, either through a `to_string` method or through left shifting into a stream. If the HDF5 C++ library [43] is found, several of the classes gain support for saving and loading from a HDF5 file or a filename. Each of the classes saves to a different HDF5 group, so one file supports multiple saved objects.[1]

## 7.1 Data Collection

Data collection from the FEBs is done by a series of classes, each representing a higher level of abstraction from the underlying LibUSB library. These will be discussed in order, starting with `Async`, then `FEB`, then `FEBMap`. The user will primarily interact with the `FEBMap` class.

### 7.1.1 Async

The `USB::Async` class provides an object oriented abstraction on a portion of the LibUSB backend [56]. The `user_data` structure holds information that will be available to the C style callback function that LibUSB requires. In C fashion, a pointer to this structure will be available as a void pointer that must forcibly be cast to this structure. It contains a 512 byte vector of buffers that it can use to collect from the USB device. It has a mutex, along with a pointer to an atomic counter that keeps track of the live connections. It holds a pointer to the USB context, and has a boolean toggle that signifies the end of the execution for a callback.

[1] Only the `Histogram` class supports saving multiple instances of itself in a file, through a changeable group name parameter.

The actual `Async` class provides the user facing interface. You can start and end transfers, and you can get data that has occurred. Note that data will not be transferred unless you are polling the USBs (generally in a dedicated thread); just calling `start_transfer` only registers the callback with LibUSB (and, likewise, stop transfer requests a stop). This class holds a pointer to the LibUSB transfer structure.

Your polling thread should continually poll `libusb_handle_events_timeout`, while monitoring the number of "`live_threads`" (live transfer requests), and should finish when that number becomes 0. A convenience function as been provided to do this for you, `USB::atomic_event_thread_func`.

General code that uses this is given is Listing 7.1. Note that this is a low level interface that is used by FEB and FEBMap, and is used by the other classes.

C++11

```
std::atomic_int live_threads = 0;

// For each device:
USB::Async async_device(usb_handle, context, &live_threads);
async_device.start_transfer();

// Inside polling thread:
USB::atomic_event_thread_func(context, &live_threads);
// Blocks till done
```

Listing 7.1: It is assumed that LibUSB has been used to create a context and device handles have been collected.

### 7.1.2 RawPacket

The `RawPacket` class represents data from a packet sent from the FEBs. The `RawPacket` class compiles differently for the old and new systems, but provides the same interface for both.

Generally, a `RawPacket` instance will be constructed with a 512 byte binary packet, though the `fill_packet` method can also be used on an empty packet. On construction, it will interpret and store the details from the packet. If the packed is ill-formed, a `RawPacket::AlignmentError` exception is thrown.

The `get_hits` method will access a vector of hits from the packet, and `add_hits` will add hits to the packet. A hit is a structure with timestamp and daq. This class,

like most of the library, supports intelligent output to a string.

You can keep adding hits from packets to `HitVector`, and it can be saved to both compressed HDF5 and uncompressed binary formats. This is used to make the "raw samples", which are small roughly 10 second collections of raw tracks that can be analyzed later for detector performance and troubleshooting.

### 7.1.3 ConfigPacket

The two classes, `ConfigASDPacket` and `ConfigPacket`, are designed to build configurations and sending them to the ASDs. The `ConfigPacket` holds and formats four instances of `ConfigASDPacket`, which in turn hold the configuration details of each ASD (see Table 3.1). The binary packets thus created can be sent directly to the FEBs.

The class `FEBSettings` holds a collection of settings for each FEB. It supports saving and loading, and can read in a space separated list of ASD thresholds from a text file, allowing for simple on-detector threshold settings.

### 7.1.4 FEB

The FEBs are more completely encapsulated by the `FEB` class. While the Async primarily abstracts the asynchronous portion of FEB communication, and only is specialized for our FEBs in the size of the raw packets, FEB represents the boards fully. Generally, an `FEB` is created by passing a `libusb_device` to the `FEB` constructor; the context and an active threads atomic can also be passed as pointers. The `FEB` instances are non-copyable, since there can only be one instance per `FEB`.

Upon instantiation, `FEB` opens and claims the LibUSB device. An Async instance is prepared, and `FEB` initializes several counters and histograms to 0. On destruction, `FEB` will release the devices and close them out.

The static method `FEB::read_all` will go through all your devices and pick out the FEBs, and return a vector of instances of `FEB`s. The FEBs are not numbered at this point; no reads have been made.

The `initial_read` method will identify the FEBs. On the new system, this simply reads a packet. On the old system, it identifies the packet as a normal pack or the first one, and then interprets that.

The `configure` method sends a configuration number or packet to the board. Soon, it will also do a 4 reads to clear the queue, and then read to see if the configuration took. It will return true if it did or try again a number of times.

The `read_events` method allows you to get an event without the async framework; `async_start_transfer` and `async_cancel` start and stop the `Async` system, and `async_process` will read in the packets stored in the `Async system` into the FEB, converting them to `RawPackets`. Another method, `put_events_in_queue`, can take a queue and put the events (in timestamp order) into it (called by `async_process` if the `queue` parameter is `true`).

An example of the use of this class is given in Listing 7.2.

C++11

```
auto feb_list = FEB::read_all(context);
for(auto feb : feb_list) {
    feb.inital_read();
    feb.async_start_transfer();
}

// Start a collection thread, polling LibUSB
std::thread poller(
    USB::atomic_event_thread_func, context, &live_threads);

// Outside polling thread
while(true)
    for(auto feb : feb_list)
        int num_packets_read = feb.process();
```

Listing 7.2: Example of `FEB` usage. A list of `FEB`s is created, and each one is read from and prepared for polling. The polling thread is started manually. Now that LibUSB is being polled, we can read the number of packets collected each time from each `FEB`. This program will never end.

### 7.1.5 FEBMap

The `FEBMap` is the normal entry point into the system. It handles finding FEBs, threading, and most processes on `FEB`s. An example of the use of this class is given in Listing 7.3.

C++14

```
FEBMap febmap;
febmap.find_all();

febmap.initial_read();
febmap.async_start_transfer(); // Starts poll thread

while(some_condition) {
    auto vector_of_hits = febmap.queue_grab_hits();
    std::this_thread::sleep_for(1s);
}
febmap.async_cancel();
```

Listing 7.3: Example of `FEBMap` usage. This included timeouts to ensure that the FEBs collect data before being harvested.

## 7.2 Data Processing

The processing in UDAQ is done though several classes. The `Detector` holds all the parameters of a detector and can perform actions that require that information, such as forward and reverse tracking. Once tracking has been done, the `Histogram` class can store the four-dimensional histogram and related information representing the data run. The `Processor` class ties these together, and collects extra information, like track rate and histograms of channels and triplet information.

### 7.2.1 Detector

The detector is described through several classes that build on each other. The `DetectorDataStruct` holds the basic properties of the detector, of the three layers, and of each of the nearly four hundred strips. The `DetectorData` class inherits these as protected members, and adds a variety of methods to save, load, and do basic conversions from and to DAQ numbers. It, however, is not intended to do intensive calculations. That is reserved for the final subclass, `Detector`. As a user, every interaction will appear to be with `Detector`. These divisions are only made to keep the code organized.

Since loading a detector parameter set is such an important task for the programs in UDAQ, a convenience constructor is supplied to make loading a standard file easy. The detector parameter files are stored in a directory with a location recorded by

| Name | Format | Notes |
|---|---|---|
| DAQ number | 448 values | Returned from "from" methods and given to "to". |
| Layer, strip | 3 sets of ~100 values | Natural ordering for strips, easy to see strip adjacency. |
| Laystrip | $1000 \times \text{layer} + \text{strip}$ | Used as a way to combine layer and strip in one number. |
| PMT, channel | 7 sets of 64 values | Ordering on the face of the PMT, useful in studying crosstalk |

Table 7.1: Different strip representations used by the reconstruction and handled by UDAQ.

CMake in `Config.h`, and simply passing an integer number to Detector will load that parameter file from the parameter directory.

A second parameter allows you to enable (default) or disable the triplet table cashing; the triplet table takes a second or two to calculate, but improves the processing speed once it is calculated. This will loop over all of the possible triplets and will calculate $\chi^2$, $\phi$, and $z$ values according to the discussion in Chapter 4, and storing the results in a three dimensional matrix indexed by the strip numbers $n_-$, $n_0$, and $n_+$. A $\chi^2$ value larger than a maximum value (100) will not complete the calculation, but immediately store the max $\chi^2$.[2]

The `initialize` method should be called if not using a constructor with a number or filename; this method will perform the necessary calculations for accessing the inverse lookups on detector strips. An idea of all of the ways to name a strip are given in Table 7.2.1.

Reconstruction can be done using the `process` methods, which take a list of DAQ values and find the best reconstructed ray, returned as the second parameter, a `recon_t` structure with the four parameter line description, and other useful information, such as the two triplets used and $\chi^2$ value. This can also take a list with a start and an end iterator, allowing portions of a larger list to be processed at a time without copying.[3] You can also access the triplets by adding another parameter for

[2] A future speedup would be to limit the loops over strip numbers to only the ones that are going to provide a small $\chi^2$ value.

[3] C++17's planned ranges feature would be a cleaner way to implement this.

output.

This internally uses `calc_triplet` to get triplet parameters from a set of three strips, and then `calc_thickness_correction` on copies of pairs of those triplets to modify them with the thickness corrections and get a new combined $\chi^2$. After looping through all possible pairs, the best $\chi^2$ pair is chosen and the reconstruction information is created through `calc_reconstruction` on the two selected triplets. The utility `process_one` streamlines this process for a single triplet pair, performing thickness correction and reconstruction, but is not used in the processing loop since the reconstruction step is wasted on triplets that fail the $\chi^2$ test.

The forward calculation, the inverse of the reconstruction process, is also implemented as `process_to_strips`, and can take two vectors describing a ray and predict the strips hit by that ray. It can do nearest reconstruction (which can't miss a strip), or physical width reconstruction.

As a test of the system, a collection of rays can be generated. For each $p$ and $x$, a set of strip numbers can be calculated using the forward calculation. This set of hit strips can then be fed into the reconstruction system, producing a set of reconstruction parameters. The before and after values are shown in the histogram in Figure 7.1.

The code that implements this algorithm to obtain the results shown in Figure 7.1 is given in Listing 7.4. In this example, a detector is loaded and a uniform distribution is prepared. An empty set of differences is created, to be filled in with the loop that starts on line 8. A ray is generated, then the original 4-parameters are computed. The generated ray is put through the forward calculation, creating a list of strips. That list is converted to a list of DAQ numbers, and the resulting lists is processed through the reconstruction. The `recon_t` structure is created and passed in for the output. If the reconstruction was successful, the differences between the 4-parameters are stored.

### 7.2.2 Histogram

The `Histogram` class holds the four dimensional histogram collected during data runs. The dimensions of the histogram, stored internally as a `boost::multi_array`, are compiled in as a setting from `Globals`, though only minor work would be required to make this a run-time setting. A histogram is usually constructed with an instance of a `Detector`, since the detector parameters are required to set the limits on the

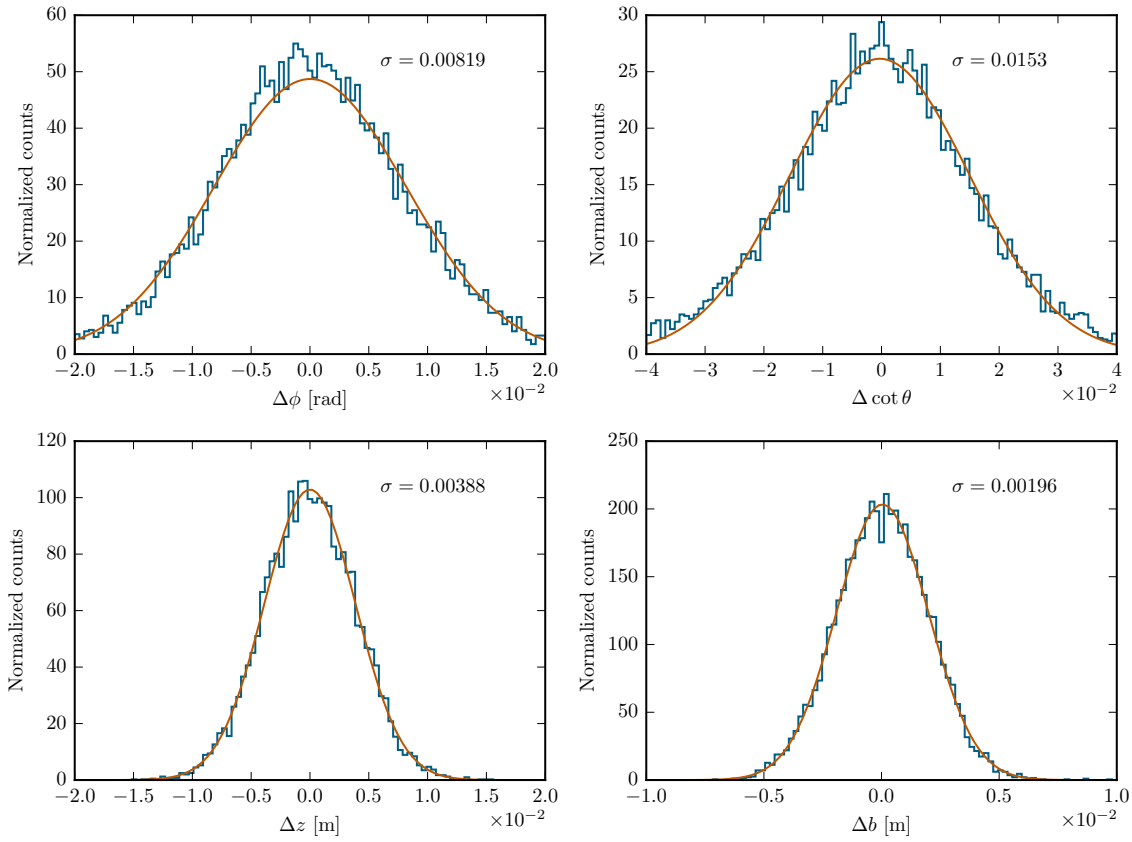


Figure 7.1: Test of tracking code. Differences in the four parameters before and after going through the forward calculation, and the strip reconstruction. This does not include scattering, but does include full details of the strip geometry. The widths of these distributions are close to the Geant simulation which does include scattering, in Figure 4.5.

```python
import udaq

d3 = udaq.Detector(3)
dist = udaq.UniformDistribution()
dist.set_detector(d3.get_length(), d3.get_radius(1), (0,0,0), (0,0,1))

diff_list = np.empty([10000,4], np.double)
i=0
while i < range(hist.shape[0]):
    num, x, p, charge = dist.run()
    orig_p = udaq.compute_four_param(udaq.ThreeVector(x),
                                     udaq.ThreeVector(p),
                                     udaq.ThreeVector([1,0,0]),
                                     udaq.ThreeVector([0,1,0]),
                                     udaq.ThreeVector([0,0,1]))

    hits = d3.process_to_strips(udaq.ThreeVector(p),udaq.ThreeVector(x))
    daqs = d3.from_laystriplist(hits)
    new_p = udaq.recon_t()
    if(d3.process(daqs, new_p)):
        diff_list[i] = (udaq.SignedAngSepPi2(orig_p.phi, new_p.phi),
              orig_p.cot-new_p.cot, orig_p.z-new_p.z, orig_p.b-new_p.b)
        i+=1
```

Listing 7.4: Example of UDAQ Python bindings to measure differences in reconstructed vs. original tracks.

histogram. After construction, the `init_detector` method is available.

There is a `read_meta` method, which allows a meta-file to be read in from a text file. The parameters in this file, translation, rotation, detector id, run number, run date, and location string are all accessible programmatically using the `set_meta_info`.

To add a hit to the histogram, `add_hit` is available, with either integer bin numbers or floating point four-coordinate parameters, or a `recon_t` structure. A count of the bins at a given set of integer values is available as `get_hit`. Utilities to convert floating points to integer bin numbers, given the detector parameters, are provided with `to_int`.

The first time `notice_time` is called, the given timestamp is recorded. On every

subsequent call, the end timestamp is updated, allowing the `Histogram` to keep a record of the total running time.

The `Histograms` support adding and equality. They also support a `set_hdf_name` method, which changes the name of the branch to something other than "DataCube", for storing multiple histograms in a single file.

### 7.2.3 Processor

The most important tool that incorporates much of the above is the `Processor` class. An instance of this class, called with a Detector to initialize it, handles the reconstruction of a stream of data. This instance holds a histogram and can collect a variety of data during a run.

To process a set of hits, the `process_hits` method is used. It can be supplied a list of hits, or a list of DAQ numbers and a time. Without arguments, it will process all stored hits. The `process_raw_hits_live` method will allow an incomplete or randomly truncated list of DAQs to be processed, with the incomplete portions stored for the next call. Finally, `process_binary` allows a filename to be passed in for reading in from a traditional binary file.

The processor keeps a running collection of information about the run that it can save to a file. The statistics stored are the number of strips hit, the number of events processed, the number of events that have at least six strips, the number of reconstructed tracks, and the number of tracks that pass the required cuts to be put in the histogram. A set of information is stored over the triplets, as well, with the number of triplets, reduced triplets, and low multiplicity triplets.

A set of histograms is also created over the FEBs, keeping track of hits, hits contributing to events, hits contributing to low multiplicity triplets, and hits contributing to tracks, with one channel per FEB channel per FEB. A histogram is also created for the $\chi^2$ values, for the event multiplicity values, and for the $z$ triplets and $z$ low multiplicity triplets. A variable size list is stored with the five minute tracking rate, as well.

The Processor can also be set to store a small sample of raw data from the beginning of the run. The number of values in this sample is adjustable through the standard options.

## 7.3 Simulation

The main UDAQ library provides a set of tools that primarily is used in the simulation software, but is available separately for use from C++ or Python.

### 7.3.1 Distribution

This is a collection of distribution generators that provide tracks from a specific distribution, filling a cylindrical space around the detector. It has a unique sub-classed design, with each aspect of the distribution being represented as subclass on the chain.

The `BaseDistribution` provides the core aspects of the distributions, and can generate the appropriate charge ratio of $N_{\mu^+}/N_{\mu^-} = 1.3$ of positive to negative muons [57], [58] and the appropriate $\cos\theta$ dependence. This also handles setup and backward projection to a world surface, needed for Geant (since Geant places the primary vertex at the location you request, and does not work well with vertices outside the world volume). This also handles cuts on the angular components of the distribution.

The `CylindricalDistribution` provides the cylindrical generation capabilities for the $\mathbf{X}$ vector. The responsibility of correctly filling space given a $\mathbf{P}$ vector is in this class.

The `LogDistribution`, `UniformDistribution` and other distributions build on this class, providing a $\mathbf{P}$ vector and handling the parameters specific to that model.

### 7.3.2 Random

This is a wrapper around the C++11 standard library random number tools that is used in creating distributions. It can easily be sub-classed to provide a different random number generator, such as the one in Geant, and that subclass can be registered with a distribution. This allows the distribution to benefit from using a single random number engine and seed from the Geant simulation, and ensures thread and MPI safety. The simulation package implements a new subclass of `BaseRandGenerator`. The default C++11 generator is `StdRandGenerator`. Currently, three random distributions are supported: uniform, normal, and lognormal.

| | |
|---|---|
| `Program` | A tool, wrapping the `boost::program_options` library, allowing structured access to command line options as well as initialization of Globals and Logging. |
| `Log` | Access to `boost::log`, with a `#ifdef` statement for removing the logging requirement. |
| `SignalHandeler` | A clean C++ way to setup Ctrl-C and other signals. |
| `Socket` | An easy way to add asynchronous sockets and a thread to handle them, for two way communication |
| `Config` | Configuration values from CMake. |
| `Vector` | A set of vector utilities, somewhat mimicking CLHEP. |
| `ExceptionDefs` | Easy macros for Python-like definitions of exceptions. |
| `Globals` | A static class that loads and saves an ini file with options available anywhere. |
| `MathUtil` | Math tools, for angular wraparound and other problems. |

Table 7.2: The minor utilities in UDAQ.

### 7.3.3 Model

The `Model` class provides a response model for the conversion of a signal from energy deposited in a strip to a trigger probability. It was developed to match the known detector signatures. The results from this comparison are given in Section 6.4.

### 7.3.4 Minor Utilities

There are several useful utilities in the library that make setting up even complex data collection programs simple and structured. Most of these utilities are meant to be general enough to be used in different programs. They are briefly summarized in Table 7.2.

## 7.4 Reconstruction

The UDAQ system is currently separate from the processing system (Python's `muview` and the C library CTools), but at some point these could be combined. The separate library is still slightly easier to compile[4], and is sufficient for the moment. Using

[4]CTools is build by python's own build system automatically when `muview` is installed, avoiding CMake entirely.

C++11 instead of C would make the code much easier to change and extend for new analysis. A basic plan for this reconstruction is in the incomplete `Shape` class using the Armadillo C++ matrix library [59].

The reconstruction code is available in two places, `muview` for Python, and HFunction for Matlab. Both of them use the same[5] CTools reconstruction algorithms in C with a Cython binding [60].

Python

```
from muview.all import *
data = DataCube(datafiles / "det2_data.hdf5")
back = DataCube(datafiles / "det2_ff.hdf5")

# 20 × 15 m, 5/2^6 m bins, 2 m above the detector
pln = Plane((20,15), 5/2**6, (0,0,2))

# Project, then apply variable binning
pln = pln.project(data, back).constant_unc(.01)

# Make a plot, add colorbar
pln.plot().colorbar()
```

Listing 7.5: Example of `muview` usage. The default projection algorithm is used to project a set of data to a plane. If this was in IPython [61], the Matplotlib library [62] needs to be initialized.

Both sets of tools are self documented, and some details are covered briefly in an appendix.

[5] CTools is a git submodule for both packages.

# Chapter Eight: Attenuation Discrepancy

A serious discrepancy between measured and predicted fluxes has prompted careful study of the lower portion of the spectrum. The following experiments highlight the difference we are seeing.

## 8.1 Brick Strip Study

An experiment was performed to test the observed attenuation using a long strip of lead bricks placed above a detector. (See Figure 8.2) The bricks were 2 inch by 4 inch by 8 inch bricks, placed directly above the detector to create a 60 inch by 4 inch target, 2 inches thick.

A sample image of this constant thickness target is given in Figure 8.1. The expected attenuation, $a$, can be calculated from Reyna's model by computing the integral

$$a(E) = -\ln \frac{\int_E^\infty \Phi(E')\, dE'}{\int_c^\infty \Phi(E')\, dE'} \tag{8.1}$$

where $c$ is the cutoff energy of the detector, and $E$ is the energy in question. This integral is nearly equal to the line $a(E) = E/3.2\,\mathrm{GeV}$, which gives the simple rule of thumb that one unit of attenuation is obtained for every 16 meters of water. Using this approximation, 2 inches (5 cm) of lead should provide 0.02 units of attenuation. Computing the full integral only provides a minor correction to this value. The observed attenuation was 0.19 units of attenuation in the vertical direction, going down to 0.05 units at 60°. This is close to ten times larger than the expected value of 0.02 units.

To include multiple scattering and intrinsic effects of the detector design, we ran a Geant4 simulation of this experiment. A similar setup was prepared, and the 11 days of simulated flat field and run time were performed on Texas Advanced Computing Center's new Lonestar 5 system [63]. The results of this are shown in Figure 8.3. This did not make a significant improvement on the predicted value, leading us to the conclusion that the spectrum at very low energies is inaccurate.

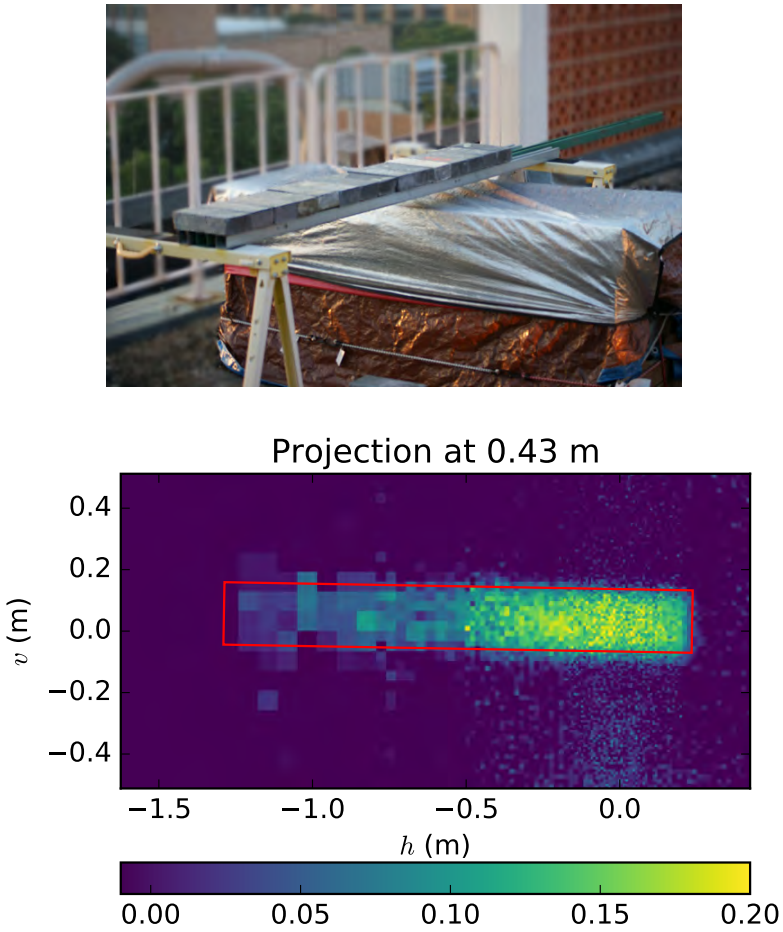


Figure 8.1: Projection of a strip of lead bricks, two inches thick, in a single layer. The brick strip was eight inches wide and was made of 15 bricks for a length of 60 inches. Data was collected for 11 days. Bin size is variable, with nearly constant error per bin in the attenuation of $\pm 0.02$. The image (above) shows the setup, with the bricks directly above the detector. The length of the bar can be estimated from the plot to be $59 \pm 5$in.

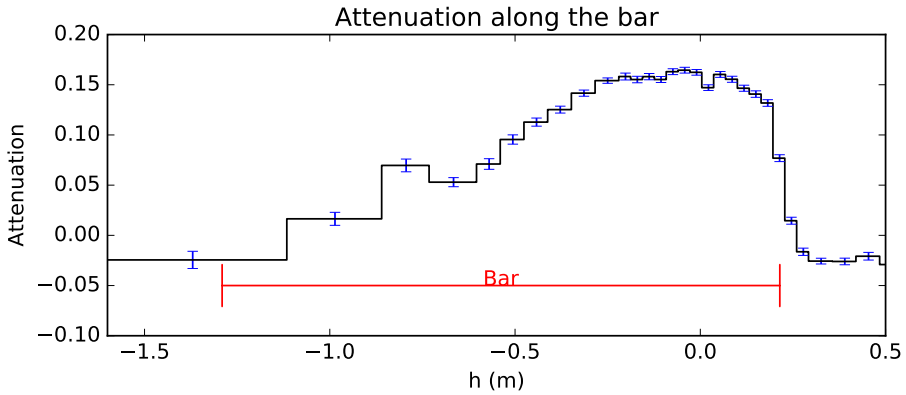


Figure 8.2: Attenuation along $h$, integrated over a 3 inch strip centered on the lead target in $v$. The image was rotated 1 degree counter clockwise relative to Figure 8.1 to account for the slight rotation of the bar. The attenuation for the nearly vertical muons was over 0.20 out to 45 degrees, which occurs roughly at $h = -0.43\,\mathrm{m}$.

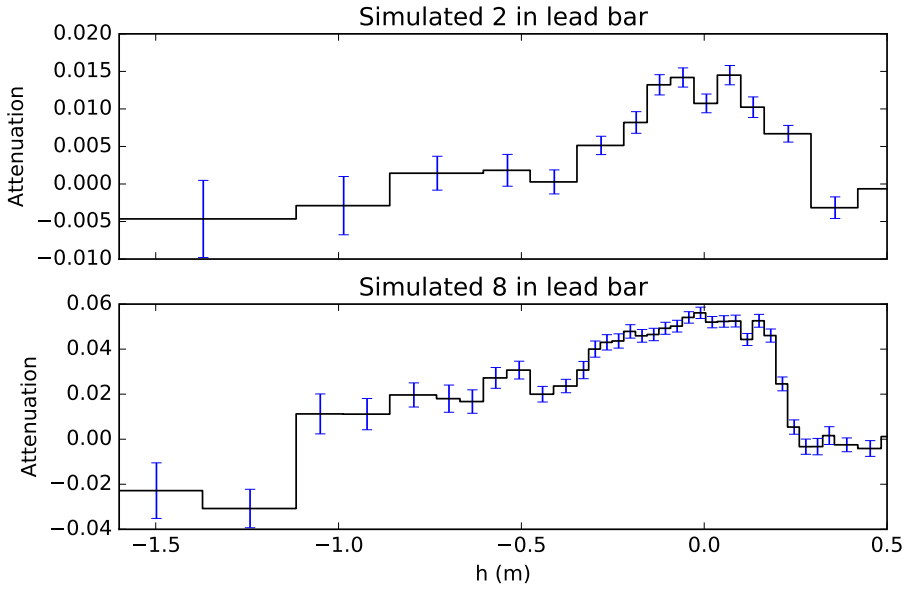


Figure 8.3: Attenuation along $h$, integrated over the width of the lead target in $v$, taken from a simulation of the same experiment (above) as 8.2. The target is distinguishable near the center of the detector at 0 m at several $\sigma$, but is less than 10% of the attenuation seen in data, and is close to the expected value using the given muon spectrum. An eight inch thick bar (below) was also simulated, showing the same character as data, but still less than the two inch bar in data.

## 8.2 ARL Object Runs

One of our detectors was placed at Applied Research Laboratories (ARL) and was put through a series of tests with different objects. These runs provide a variety of different materials and thicknesses. A student working at ARL, Minh Van-Dinh, set up the objects and recorded the physical parameters of each setup.

All runs were made by placing objects above the detector on a plywood base 51.36 cm above the detector center. Unless otherwise noted, all objects were placed directly above the central axis of the detector. All measurements noted will be from the center of the detector, on the surface of the wood, to the center of each of the objects. The $x$ coordinate is along the axis of the detector.

The flat-field was made using 494 hours of runtime from runs 6 and 21 in the ARL workshop, in the same location as the tests. The details of the roof are removed by this flat field; see Figure 8.4 for a image made with this "flat-field" as data against an outdoor flat-field run.

Attenuation was measured by setting the projection plane directly through the center of the object being measured, and averaging over the constant attenuation in the center of the object.

Expected attenuation was calculated using the minimum ionizing energy and density from PDG, and the ionization rate for muons of 3.2 $^{\mathrm{GeV}}/_{\text{unit atten}}$. Geant4 was used to simulate the targets and the same procedure was used to measure the attenuation from the resulting images. An example of a simulated image is shown in Figure 8.5.

In the next few pages, I will present our results from this study. Notice especially the differences between the attenuations listed. For small targets, we are still seeing a marked difference between the values.

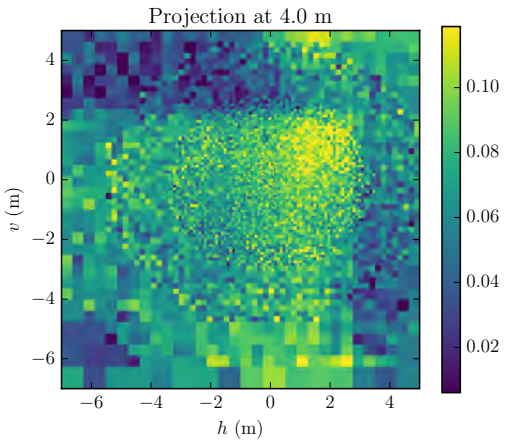


Figure 8.4: An image of the roof in the ARL lab. The detector was at $h = 0\,\text{m}$, $v = 0\,\text{m}$. The edges of the building are visible at $v = 2\,\text{m}$ and $h = 2.2\,\text{m}$. The walls provide less attenuation than the roof, making the transition stand out.

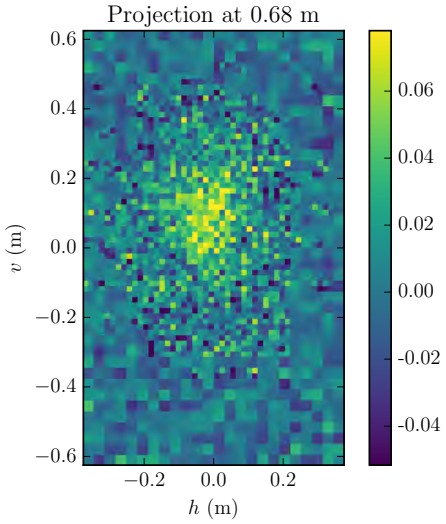


Figure 8.5: An example of the Geant4 simulation, in this case of the tall aluminum block shown in Figure 8.6.

### 8.2.1 Tall Aluminum (Runs 24–28)

| Name | Block 6063 |
|---|---|
| Material | Aluminum |
| Size [cm] | $[14.82, 21.37, 36.12]$ |
| Density [$g/cm^3$] | 2.589 |
| Expected attenuation | 0.0472 |
| Geant simulated attenuation | 0.0677 |
| Measured attenuation | 0.141 |

Table 8.1: Theoretical track rates.

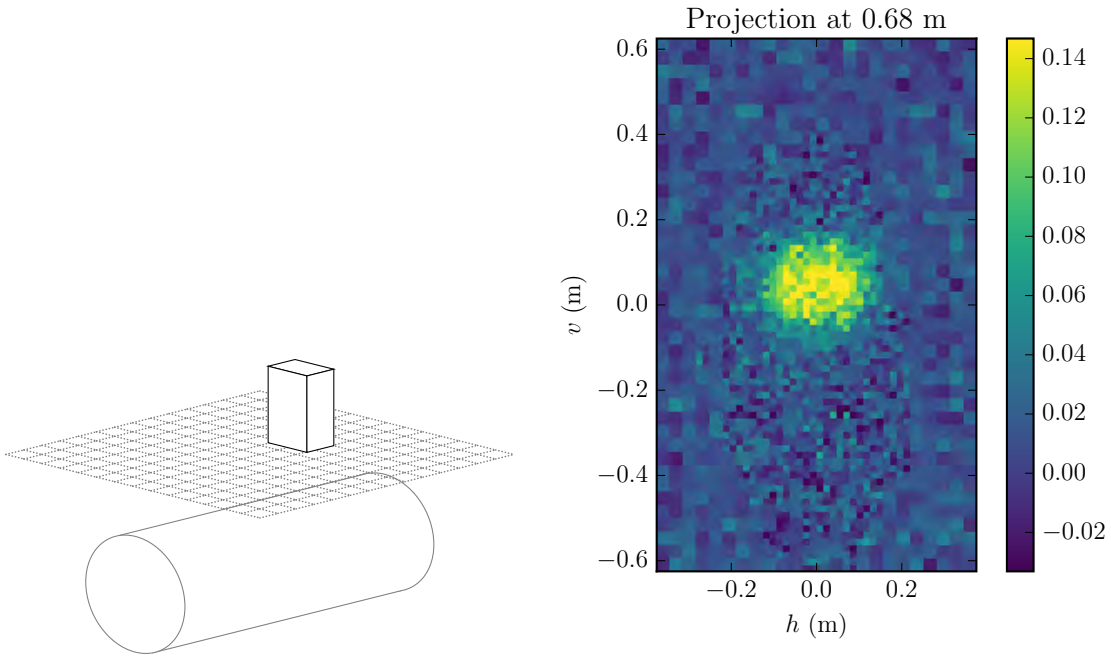


(a) Illustration of setup.

(b) Resulting image.

Figure 8.6: A tall aluminum block was placed vertically over the detector. The attenuation is roughly a factor of three off for both simulation and calculation.

### 8.2.2 Cement and Titanium (Runs 31–37)

| Name | Cement Block | Titanium Cylinder |
|---|---|---|
| Material | Cement | Titanium |
| Size (cm) | $[20.40, 40.70, 10.13]$ | $r = 5.58, h = 15.19$ |
| Density ($g/cm^3$) | 2.207 | 4.545 |
| Expected attenuation | 0.0120 | 0.0319 |
| Geant simulated attenuation | 0.028 | 0.049 |
| Measured attenuation | 0.0662 | 0.104 |

Table 8.2: Theoretical track rates.

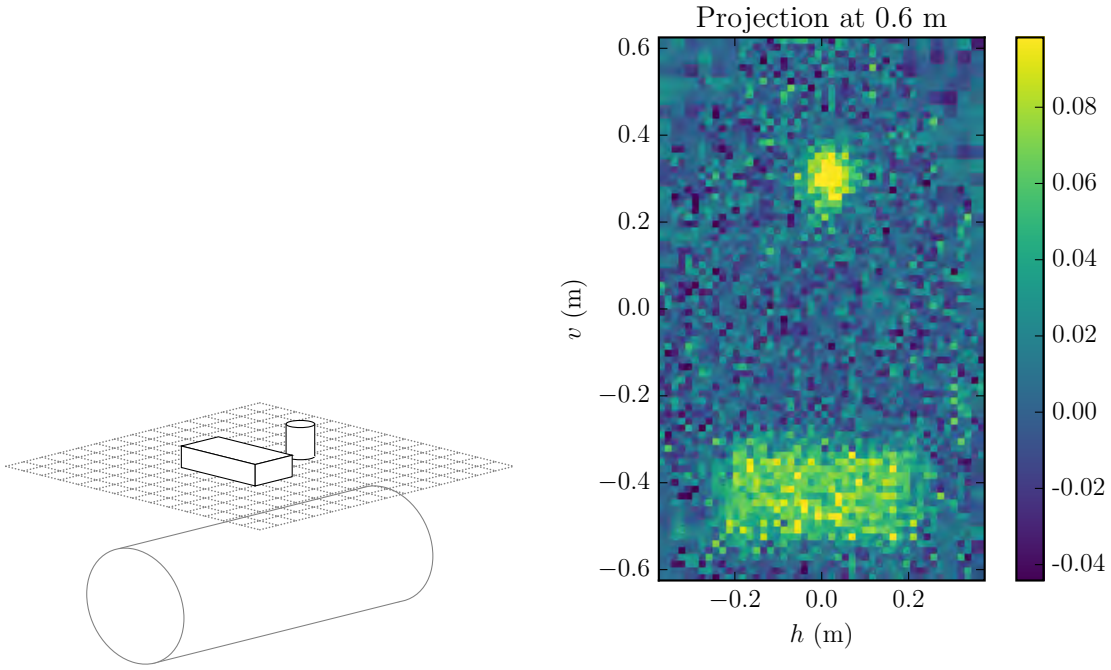


(a) Illustration of setup.

(b) Resulting image.

Figure 8.7: A cement block and titanium cylinder were placed above the detector. The attenuation is much higher than expected or simulated.

### 8.2.3 Aluminum and Steel (Runs 43–49)

| Name | Block 6063 | Cylinder |
|---|---|---|
| Material | Aluminum | Steel |
| Size (cm) | $[14.82, 36.12, 21.37]$ | $r = 7.66, h = 7.45$ |
| Density ($g/cm^3$) | 2.589 | 8.080 |
| Expected attenuation | 0.0279 | 0.0273 |
| Geant simulated attenuation | 0.0390 | 0.03078 |
| Measured attenuation | 0.0988 | 0.125 |

Table 8.3: Theoretical track rates.

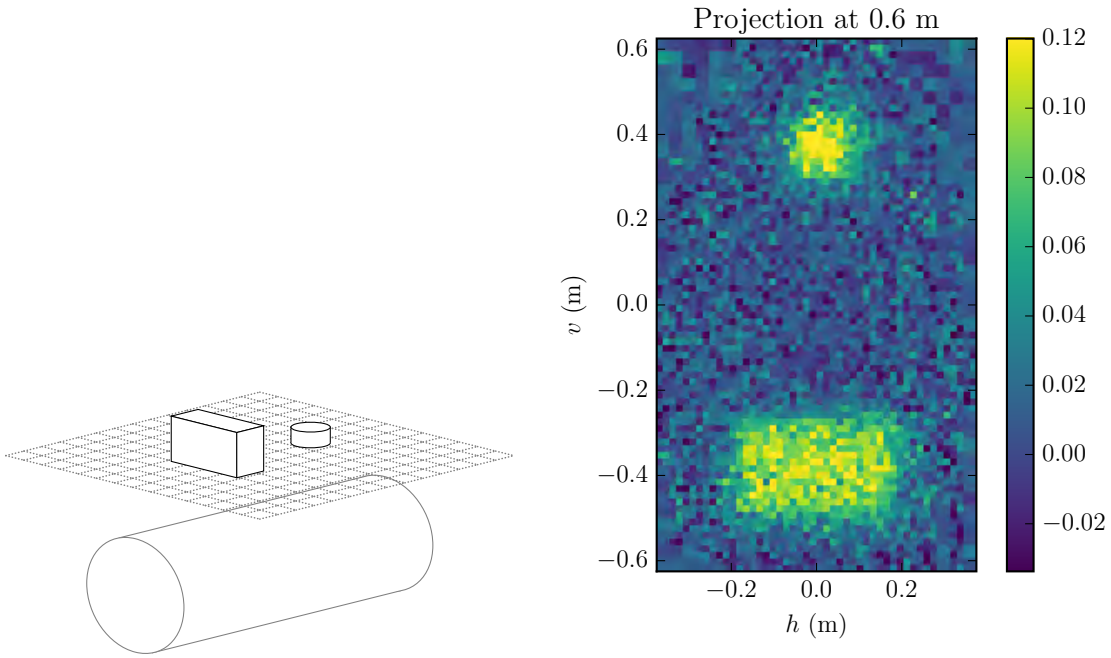


(a) Illustration of setup.

(b) Resulting image.

Figure 8.8: An aluminum block and a steel cylinder were placed above the detector. Both objects provide much more attenuation than expected.

### 8.2.4 Aquarium (Runs 51–57)

| Name | Aquarium |
|---|---|
| Material | Water |
| Size (cm) | $[51.1175, 25.7175, 30.7975]$ |
| Density ($g/cm^3$) | 1 |
| Expected attenuation | 0.0191 |
| Simulated attenuation | 0.0415 |
| Measured attenuation | 0.0793 |

Table 8.4: Theoretical track rates.

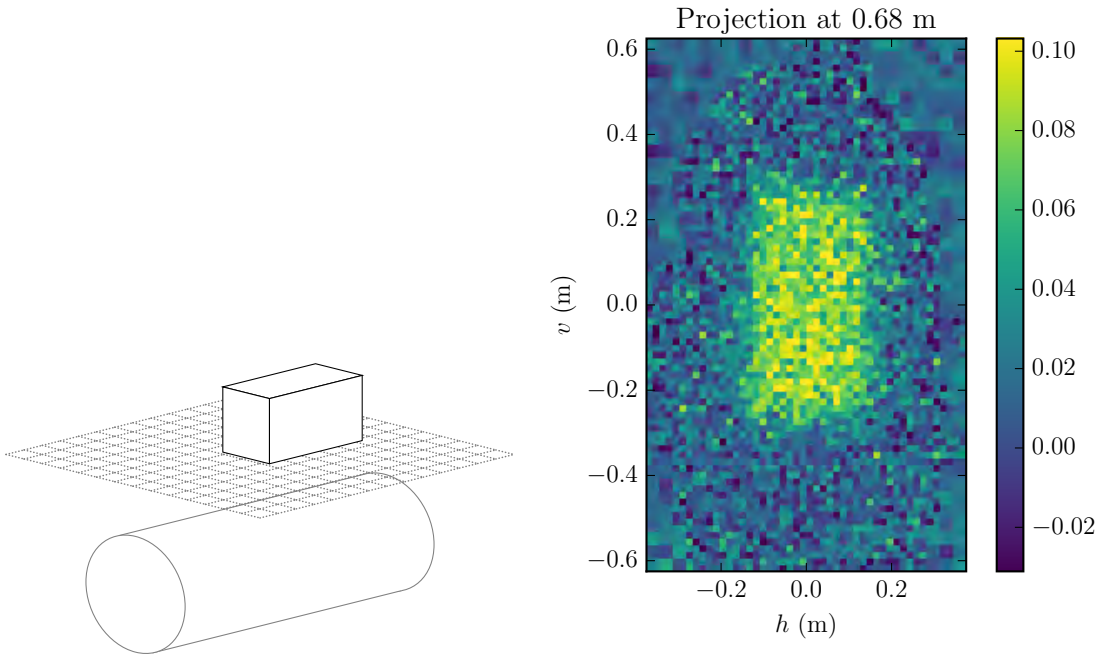


(a) Illustration of setup.

(b) Resulting image.

Figure 8.9: A water filled aquarium was placed above the detector. The simulated attenuation is still a factor of two off from expectations, but better than the previous targets.

## 8.3 Underground Runs

Underground placements of the detectors provide a vast array of applications, primary involving tunnel and chamber detection. Computing the average muon flux through the detector is crucial in these applications, to allow accurate calculations of the time needed to take a usable image. The high energy muon spectrum is well understood, so accurate predictions of muon attenuation are easily possible using simulations, such as Geant4.

### 8.3.1 Prediction

For these tests, we will assume that we have standard rock, with an average atomic number of 11 and an average density of $2.65\,{}^{\mathrm{g}}/_{\mathrm{cm}^3}$ . The radiation length is then $X_0 = 26.5\,\mathrm{g\ cm^{-2}}$, or $X_0 = 10.0\,\mathrm{cm}$, and the minimum ionization energy is $0.447\,\mathrm{GeV\ m^{-1}}$ [25]. This corresponds to an attenuation of $7.15\,{}^{\mathrm{m}}/_{\text{unit atten.}}$

The rms plane angle is described by

$$\theta_0 = \frac{10.6\,\mathrm{MeV}}{\beta cp} z \sqrt{\frac{x}{X_0}} \left[1 + 0.038 \ln\left(\frac{x}{X_0}\right)\right]. \tag{8.2}$$

Given the minimum energy that can reach the detector, we can calculate the expected angle for that energy, and find the traverse distance the particle may travel as $y_{\text{plane}}^{\text{rms}} = \frac{1}{\sqrt{3}}\theta_0 d$, where $d$ is the depth underground. This will provide a crude estimate of the minimum required penumbra around the detector for scattered muons to be mostly accounted for. This estimate should be within 11% at 20 m [25].

The expected track rate comes from using a base track rate of 25.0 Hz and using the attenuation to calculate an expected track rate. The track rates calculated in Table 8.5 are close, though slightly lower, than the measured rates in the experiment (around 8 Hz for roughly 10 m).

### 8.3.2 Setup

In the simulation, the detector is placed in a thick walled tube (see Figure 8.10). The inner diameter of the tube is just larger than the detector, and the outer radius is set based on the depth of the detector underground.

| Depth | Attenuation | Min. energy | $\theta_0$ | $y_{\text{plane}}^{\text{rms}}$ | Track rate |
|---|---|---|---|---|---|
| 0 m | — | — | — | — | 25.0 Hz |
| 10 m | 1.40 | 4.47 GeV | 0.0278 | 0.161 m | 6.18 Hz |
| 20 m | 2.80 | 8.95 GeV | 0.0201 | 0.232 m | 1.53 Hz |
| 30 m | 4.19 | 13.4 GeV | 0.0166 | 0.288 m | 0.377 Hz |
| 40 m | 5.59 | 17.9 GeV | 0.0145 | 0.336 m | 0.0932 Hz |

Table 8.5: Theoretical track rates.

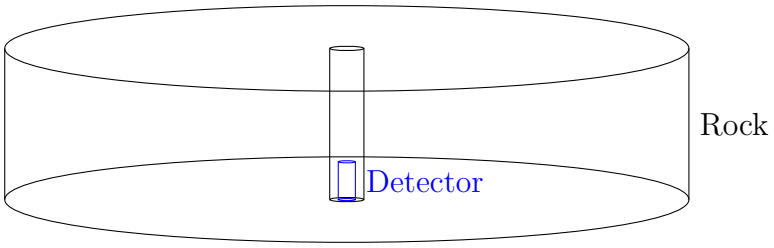


Figure 8.10: Underground simulation

Results of the Geant4 simulation are listed in Table 8.6. The width is the outer radius of the rock, and the normalized track rate was adjusted to the 25 Hz track rate after the simulation was completed.

| Depth | Width | Penumbra | Simulated runtime | Track rate | Attenuation |
|---|---|---|---|---|---|
| 0 m | — | 3 m | 0.75 hours | 25.0 Hz | 0 |
| 10 m | 60 m | 3 m | 0.75 hours | 7.42 Hz | 1.21 |
| 20 m | 60 m | 3 m | 0.75 hours | 2.42 Hz | 2.33 |
| 30 m | 125 m | 3 m | 2.08 hours | 1.03 Hz | 3.18 |
| 40 m | 125 m | 3 m | 2.08 hours | 0.503 Hz | 3.91 |

Table 8.6: Simulated track rates.

### 8.3.3 Measurement

A measurement was made underground in a vertical shaft similar to the one simulated above. The shaft diameter was slightly larger than the diameter of a detector, and was lined with corrugated pipe. There were two detectors in the shaft. The center of

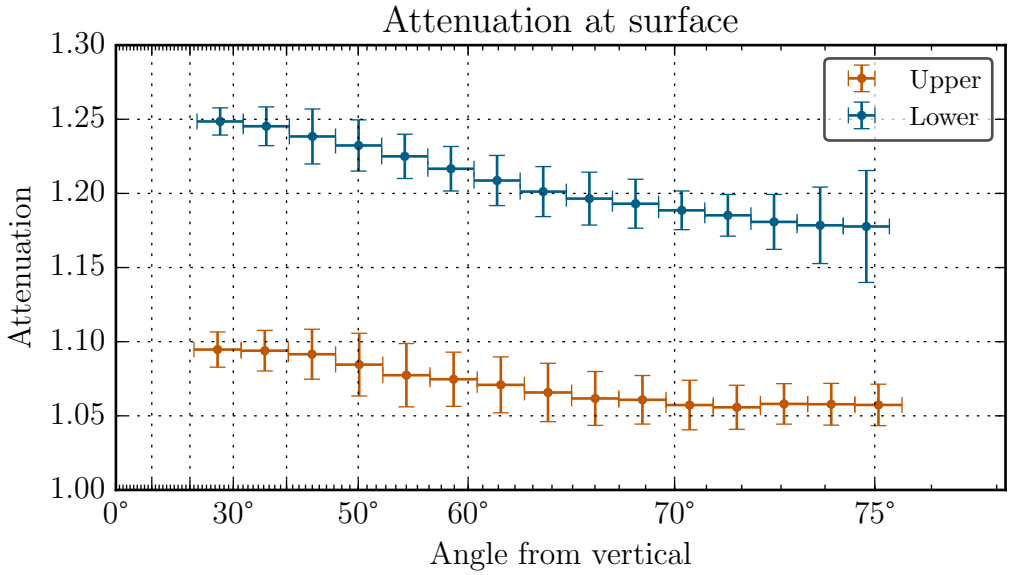


Figure 8.11: Attenuation integrated in a circle at constant radius from the center of the detector over a plane at the surface. The error is from the standard deviation across the integrated bins.

the upper detector was 8 m below the surface of the ground. The center of the lower detector was located 1.65 m below the center of the upper detector.

The vertical orientation of the detectors was not well aligned, so a linear plane of the form $ax_i + by_j + c$ was fit using least squares to the projected data.[1] The zero-centered solution, $ax_i + by_j - a\bar{x} + b\bar{y}$ was subtracted from the attenuation. This leaves the average attenuation constant, but removes the overall slope that was seen due to the mismatched flat field and detector spectrum orientations. This technique works well for recovering from small variations in orientation. In Chapter 10, a similar orientation difference between datasets will be encountered, and will be solved by transforming the data through a rotation, but will not keep the same fidelity required here in the reconstruction images due to detector strip aliasing.

The resulting attenuation is close to the expected value, with an observed overall attenuation in the upper detector of 1.08, and 1.23 for the lower detector. The combined data, projected at the surface, is shown in Figure 8.3.3. The attenuation

[1] This is provided in MuView as the `.flattattenuation` property on `Plane` instances, utilizing `muview.tools.num.fit_to_plane`.

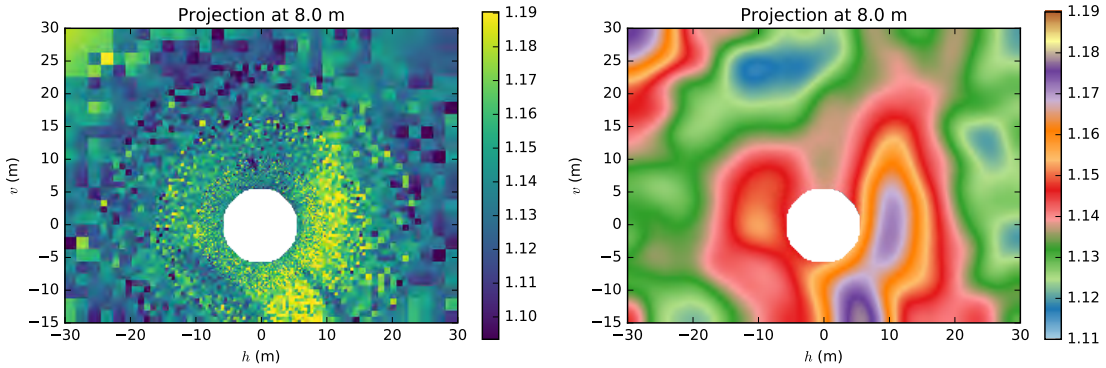


(a) A standard variable bin plot.

(b) A Gaussian low-pass filter has been applied, and a striated color map was used to highlight the attenuation behavior.

Figure 8.12: Projection at ground level of underground run. Two tunnels, discovered through a blind study, are visible but currently out of focus. The overall attention remains relatively constant.

remains constant even out to 75° from vertical, with less than 7% variation across the range. Angles greater than 75° were not included, since nearby structures began to interfere with the data at that point. See Figure 8.3.3.

Note that the path length $l$ across this figure is changing with respect to angle, however, the component $\hat{\mathbf{z}} \cdot \mathbf{l}$ is a constant. This property of attenuation is why Reyna's $\zeta = p \cos\theta$ is so important.

This measurement was conducted as a blind search for structures in the surrounding soil. Two identified structures can be seen in Figure 8.3.3, in the lower portion of the projection. The straight structure on the lower left is a long linear void, or tunnel, roughly 0.5 m to 1.0 m in diameter, oriented at 118°, approaching the detector with a distance of closest approach of 7.8 m. The structure extends at least 15 m and appears to have a northern end just after passing the detector. The attenuation difference compared to the surrounding overburden was 0.04, which would correspond to 0.4 m of soil. The attenuation was spread over a width of 1 to 2 m in all projections. Due to the "shadowing" effect, these two values were combined to give the predicted tunnel dimensions. This structure was discovered by looking at projections after only 44 hours of run time, though the displayed projections and measurement use the total integrated run time of over 500 hours.

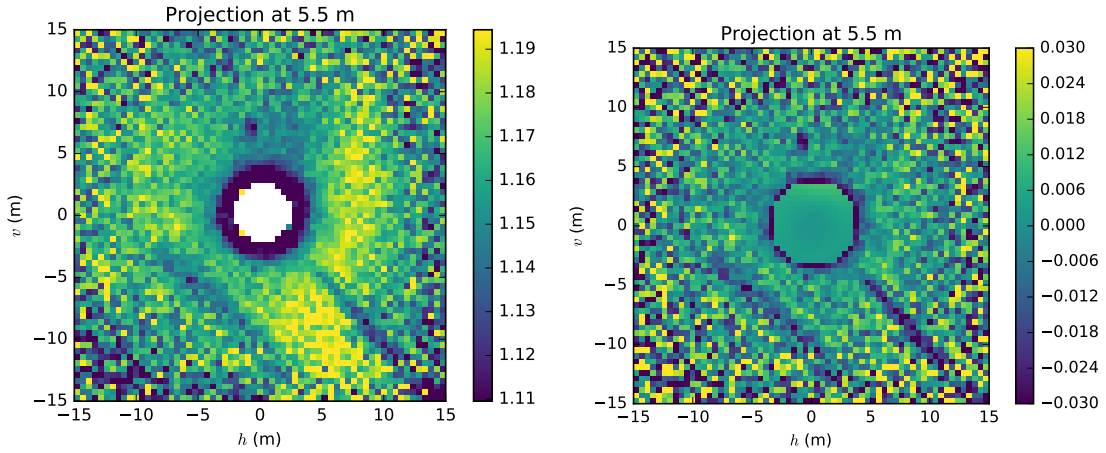


(a) A standard map-view projection, with constant bins.

(b) A Gaussian high-pass filter has been applied, removing surface details but leaving the tunnel structures intact.

Figure 8.13: Projection 2.5 m below the surface, directly through the tunnel structures.

The second structure is a radial linear void, with a heading of 116° and similar shape and height. This one took longer to identify only because there was originally a fear that it was an artifact of the projection. A small 2° variation was discovered between the two nearly parallel tunnels, which proved to be correct.

A fiducial tunnel was drilled at an angle directly toward the upper detector and left hollow. This is seen as a round point of reduced attenuation 7 m away from the shaft center in the 100° direction in Figure 8.3.3.

## 8.4 Conclusion

These underground measurements indicate that we do understand the muon spectrum and interactions quite well for higher energy muons. The experiments with thinner targets, however, pose a problem. In the next chapters, we will go into an experiment to measure the low energy muon spectrum in an attempt to solve this inconsistency.

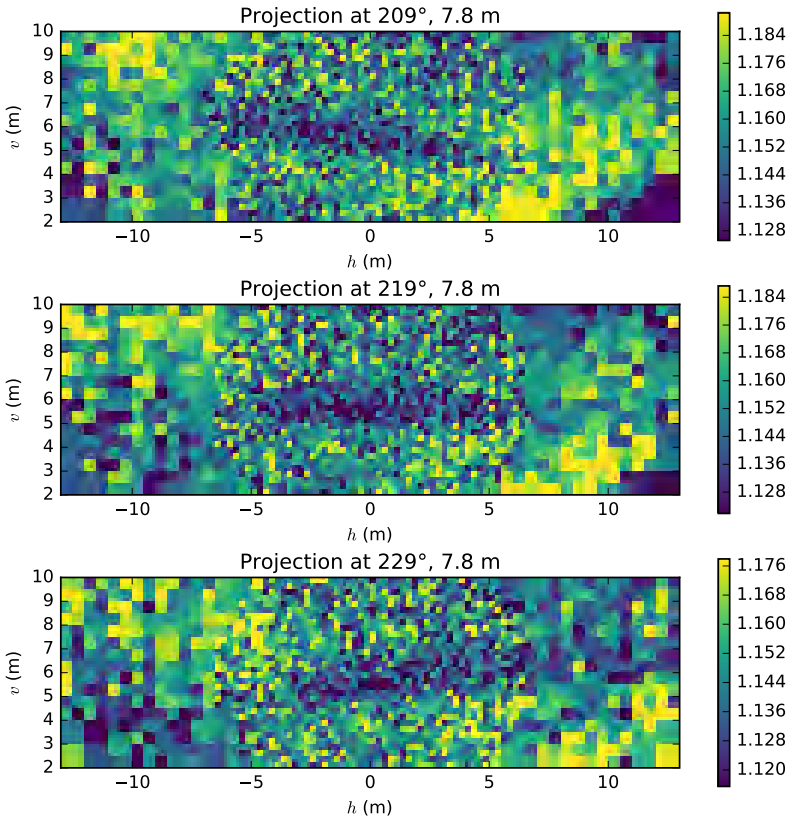


Figure 8.14: Vertical projection planes, perpendicular to a vector at $219° \pm 10°$, 7.8 m away from the axis of the detector. The three different projections show a plane parallel and through the center of the tunnel, along with one on either side, making the tunnel appear to change depths over the $h$-axis due to the shadowing effect discussed previously.

# Chapter Nine: Design for the Low Momentum Measurement

In the previous chapters, the images of small targets have consistently shown that the predicted attenuation is significantly smaller than we expected from our knowledge of the detector and the cosmic ray spectrum. For targets with several GeV of muon energy loss, the image attenuation is close to the predicted values. The measurements that are not following our prediction are most sensitive to the very lowest portion of the cosmic ray spectrum, near and under 1 GeV.

Previous work has taken precise measurements of the higher energy spectrum, due to the importance of well defined backgrounds for shielded high energy experiments, but does not cover the lower portion of the spectrum with equal precision. The low energy muon spectrum was measured down to a mean momentum of 0.34 GeV/c by Allkofer, Carstensen, and Dau [64], but with a coarse momentum resolution, few recorded events, and no angular dependence. Bellotti *et al.* [65] measured down to a similar limit over a wide range of depths using balloon flights, but only measured negative muons flux, making the comparison difficult, due to the need of muon charge ratio measurements in $< 1$ GeV portion of the spectrum, as it depends on momentum and geographical location. The Rastin model [66] that is used to support the CRY cosmic ray generator [67], was predicted from a small data set that included only vertical measurements [31], which have been included here.

Our detectors collect data with high angular resolution and over a large solid angle, making them an ideal tool for a spectrum measurement. The measurement is over the integral spectrum, $\Phi = \int_{p_{\min}}^{\infty} \frac{d\Phi}{dp} dp$, where $p_{\min}$ is the lowest momentum muon detectable. This value is a function of the material in the detector, and was predicted from simulation to be 110 MeV (See Section 4.4.3).

By placing an absorber between the detector and the sky, we effectively change this lower bound by the attenuation in the absorber, such that $\Phi = \int_{p_{\min}+p_a}^{\infty} \frac{d\Phi}{dp} dp$, where $p_a$ is the momentum lost passing through the material. By varying the thickness of this absorber, the original muon spectrum $\frac{d\Phi}{dp}$ can be recovered from $\Phi(p_a, \theta)$.

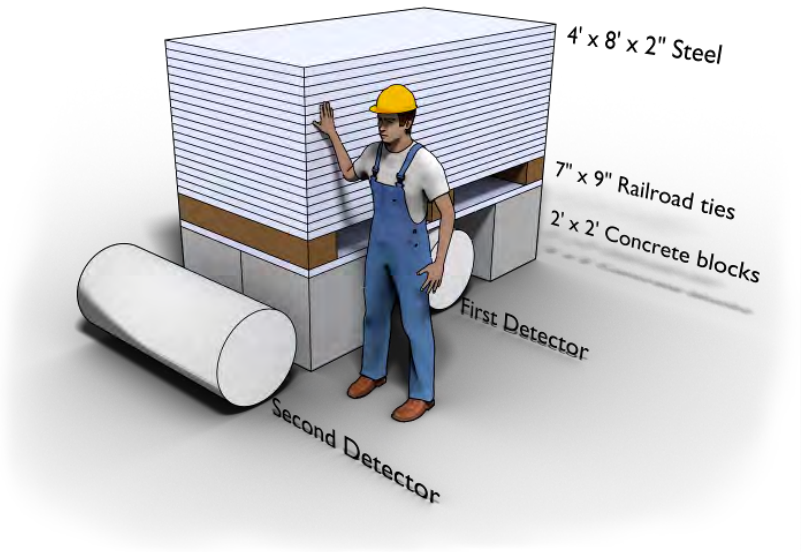


Figure 9.1: An original sketch of the design of the originally planned experiment to measure the low momentum muon spectrum. A gap was left at the bottom to add extra targets below the stack. Two detectors would be used to cover a larger portion of the angular spectrum. A person is shown for scale.

## 9.1 First Design

Following basic principles of the design by Allkofer, Carstensen, and Dau [64], an original proposal, illustrated in Figure 9.1, was written. Although this proposal was quickly changed to one that was both more practical and better in several ways, the original plan is briefly presented here.

Steel was selected as the absorber material for this measurement. In order to have 1 GeV of attenuation, we would require a thickness of 85 cm of steel. We would like to have at least 10 to 20 steps in this range, so we would use commercially available steel plates 1.5 to 3 inches thick. In order to measure the attenuation at different angles, the stack should be wide enough to accommodate 45°-60° measurements. By placing a second detector next to the stack, run time and stack size would be reduced, while retaining the large angle measurement capability. With these requirements, this could be done with 4 by 8 foot steel plates with a standard thickness of 2 inches.

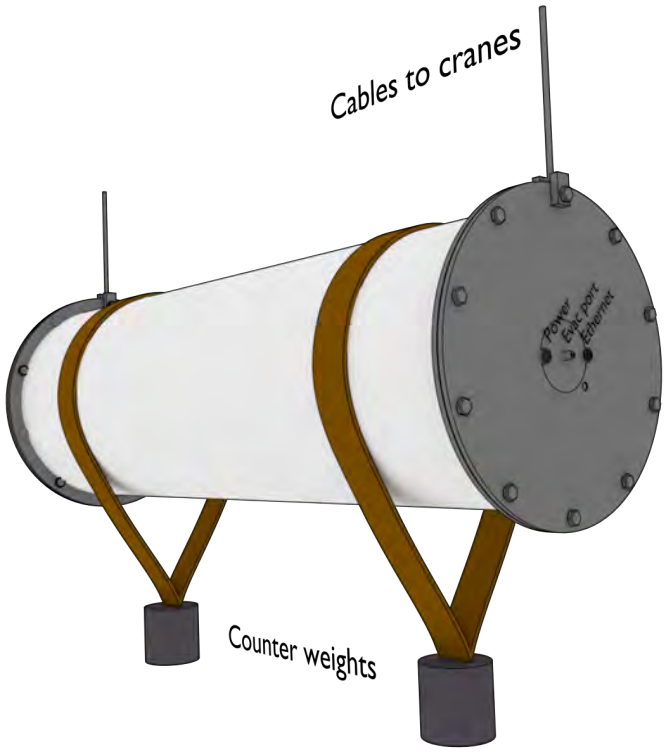


Figure 9.2: A sketch of the second proposal for the ARL experiment. The detector is encased in an enclosure used to make the measurements underwater. The entire device is positively buoyant, so counterweights need to be added.

## 9.2 Redesign

Upon discussion over this experiment at Applied Research Laboratories, a slightly different method of measurement (see Figure 9.2) was proposed that offered several advantages. An underwater enclosure could be created for the detector, and lowered into a lake. This would allow measurement out to shallow angles with a single detector, freedom to select any depth to vary the amount of absorber, and the ability to measure a larger momentum range than the previous plan.

The underwater enclosure was fashioned from a 24 inch outer-diameter PVC pipe. The pipe was cut to a length of 6 feet. The ends were made from two sheets of plastic, one cut to a ring shape and glued to the PVC pipe, and the other bolted on with 10 bolts and an o-ring seal. One end had a power connector, an Ethernet feed-through, and a vacuum evac port.

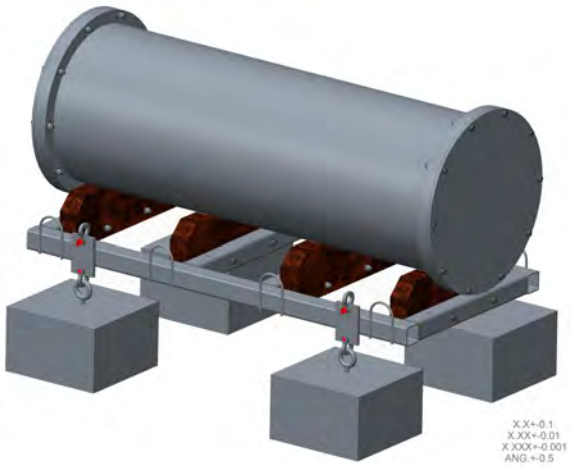

Figure 9.3: Final design of the detector enclosure, created by Richard D. Lenhart. The chains supporting the device connect via carabiners directly above the four weights. Straps (not shown) hold the detector in place. Image provided in private communication with Martin Barlett.

The enclosure was strapped down to a frame through a series of metal hoops soldered to it. The frame had four plates with metal eye loops both above and below. The lower eye loop was for attaching counterweights, pictured in Figure 9.3 as rectangular masses. They were actually attached via short chains and carabiners, to facilitate deployment.

The cables supporting the detector were attached to electronic hoists on davits attached to the side of a barge. The maximum clearance was just about a meter above the water, not enough to hang the weights on the detector. The chains on the counterweights allowed the weights to be attached first, then lowered into the water one at a time.

## 9.3 Flux Prediction

The expected flux for the depth range from $d_{\text{det}} = 0\,\text{m}$ to $d_{\text{det}} = 35\,\text{m}$ can be easily predicted using the previous discussions. Given the log Gaussian model that was developed in Section 6.1.1, we have a flat field rate of

$$FF_{\text{rate}} = \frac{1}{2} I_0 \left(1 - \text{erf}\left(\frac{\ln(p_0) - \bar{y})}{\sqrt{2} y_{\text{rms}}}\right)\right). \tag{9.1}$$

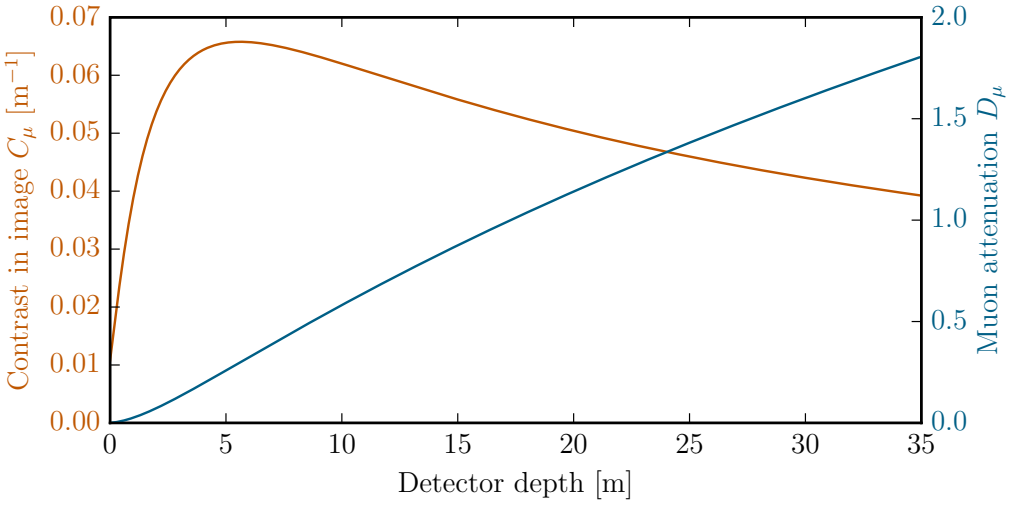


Figure 9.4: Predicted attenuation and contrast for the depth of the detector under water, using log Gaussian model. The sudden dive at shallow depths is characteristic of the current models.

The muon rate at the expected depth is then, using a constant value of $\frac{dE}{dx} = 200\,\mathrm{MeV/m}$,

$$D_{\mathrm{rate}} = \frac{1}{2} I_0 \left( 1 - \mathrm{erf} \left( \frac{\ln(p_0 + d_{\mathrm{det}} \frac{dE}{dx}) - \bar{y})}{\sqrt{2} y_{\mathrm{rms}}} \right) \right). \tag{9.2}$$

The expected attenuation is simply

$$D_\mu = -\ln \left( \frac{D_{\mathrm{rate}}}{FF_{\mathrm{rate}}} \right). \tag{9.3}$$

We can calculate the contrast in an image, the change in attenuation per meter of water, by approximating $C_\mu = \frac{dD_\mu}{dd_z}$ using a finite $d_z$,

$$C_\mu = \frac{1}{d_z} \left[ 1 - \frac{I_0}{2 D_{\mathrm{rate}}} \left( 1 - \mathrm{erf} \frac{\ln\left(p_0 + [d_{\mathrm{det}} + d_z] \frac{dE}{dx}\right) - \bar{y}}{\sqrt{2} y_{\mathrm{rms}}} \right) \right]. \tag{9.4}$$

The result of this prediction is shown in Figure 9.4. The sudden drop in contrast at about 5 m is due to the roll over in the differential spectrum in the Reyna model.

The measurement results will be presented in the next two chapters, supplying a new contrast prediction from measurements that will be compared to this result.

# Chapter Ten: Results

## 10.1 Data Collection

Data was taken in Lake Travis, Austin Texas at 670 ft (204 m) above sea level, during the period from June to August, 2015. The detector was submersed up to 12 m in the water using cranes (see Figure 10.1). Measurements were recorded to within 0.125 in using a tape measure attached to each crane, corresponding to $57\,{}^{\mathrm{MeV}}/_{c}$ of attenuation. The initial depth on each crane was calibrated by adjusting the heights until the surface of the water was flush across the top of the detector. Data was collected at each depth in several runs, with a maximum of 24 hours for a indevidiual run.

Shallow runs were collected during the week, with roughly two days per depth. The deeper runs were made during the weekend, due to the lower muon flux at deeper depths requiring a longer collection period. This also kept the detector away from the surface during the increased activity on the weekends, reducing the effect of surface turbulence from recreational motorboats on the lake.

The detector was not secured to the interior of the cylindrical enclosure, but was free to rotate around its $z$ axis during the run. Small rubber wedges were intended to minimize this movement, but failed to eliminate rotation during the course of the project.

As a result of this freedom, rotation around the detector axis was observed in the data during the run. The detector was originally leveled and wedged into the enclosure with small rubber strips. By the time the detector returned from the lake and the enclosure was opened, the detector orientation was a little over 5° off. The data from the running indicates a clear progression of rotation at several points during the experiment.

An accelerometer was installed inside the detector to monitor the orientation during the run, and originally intended to be used to monitoring the detector for turbulence. An initial test, seen in Figure 10.2, demonstrates the effect on the accelerometer of tilting the detector using one of the cables.

A slow continuous change, seen only in the accelerometer and not in the detector

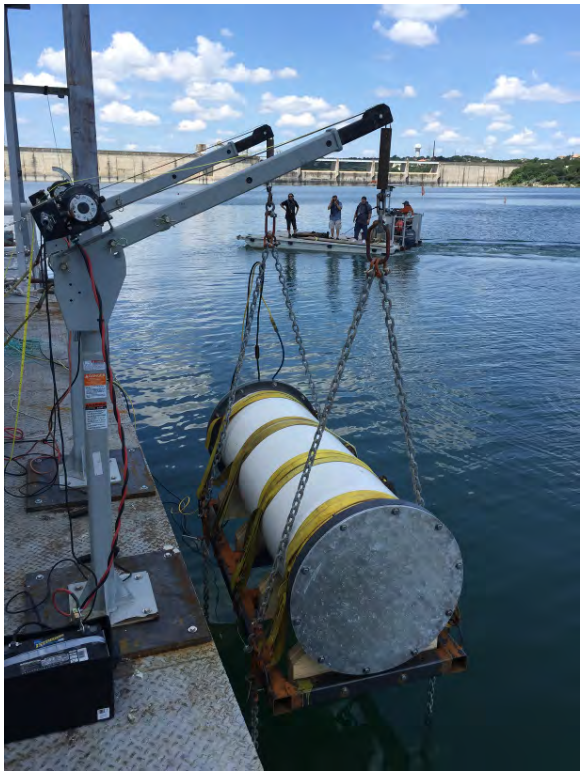

Figure 10.1: Image of detector over water suspended from a barge, about to be submersed. Cables on either side allow adjustments in the tilt of the detector.

flux during the first period, makes the data, shown in Figure 10.4, questionable at best. During the run in late June, the supply cords were left secured during one of the depth changes, causing the enclosure to swing to one side before the Ethernet cord snapped off. At this event, we lost a period of the accelerometer data, though data collection continued while the detector sat half submerged at the surface over the weekend. The next week, we cycled the partial vacuum in the enclosure to ensure that it was still waterproof, and repaired the cable. After this point, the accelerometer data stopped drifting.

## 10.2 Rotation Corrections

The best orientation measure available to us is the muon spectrum itself. Even at an early stage during the data collection, the symmetry in the data indicated a similar

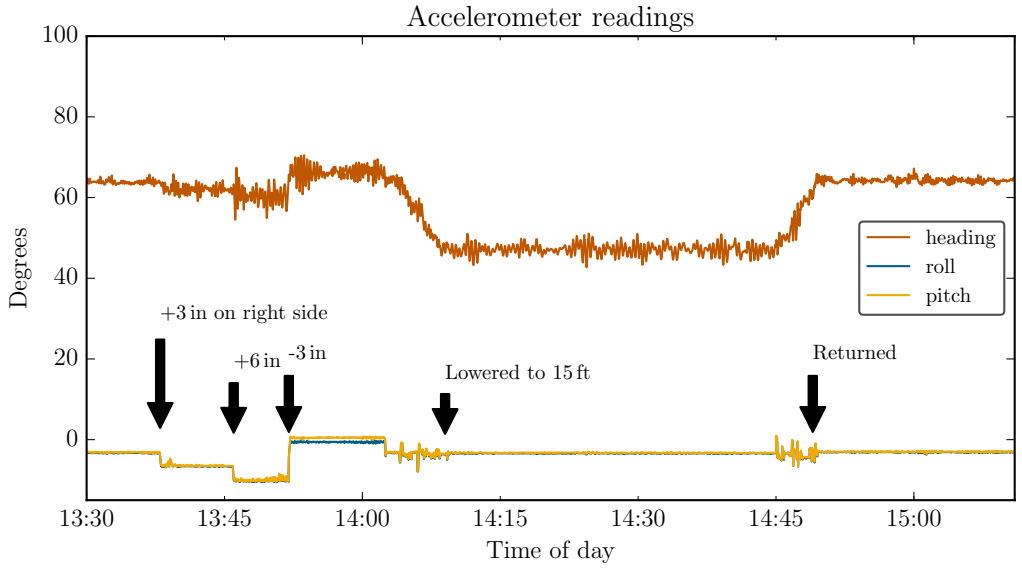


Figure 10.2: A close look at data from the accelerometer for several moves. Several events are seen and annotated on the graph. One side of the detector was raised and lowered to test the effect of a tilt. The periods where the detector was being lowered and raised are visible, in the pitch and roll.

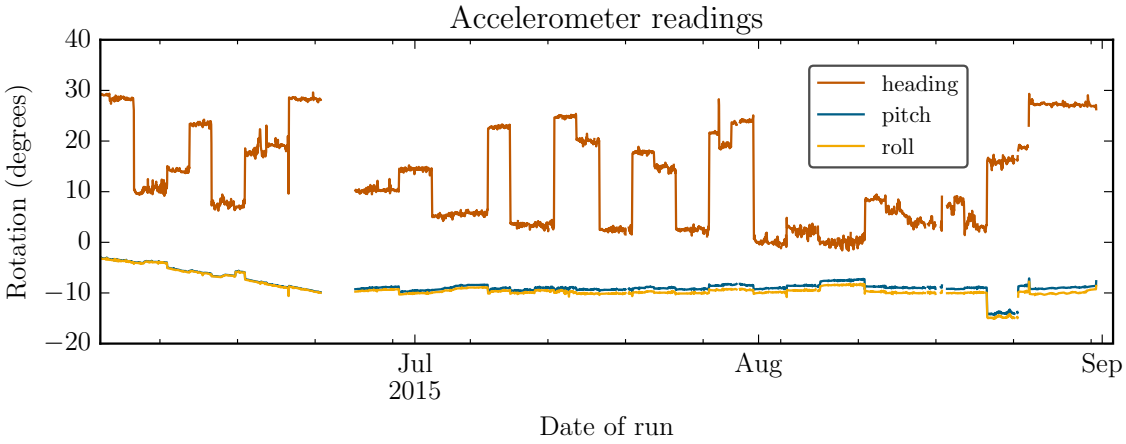


Figure 10.3: The complete set of data from the accelerometer. The heading appears to be a function of depth, probably due to the metallic barge next to the detector. Note the continuous change during the first period. The gap visible near the end of June is the "event". 35° has been subtracted from the heading.

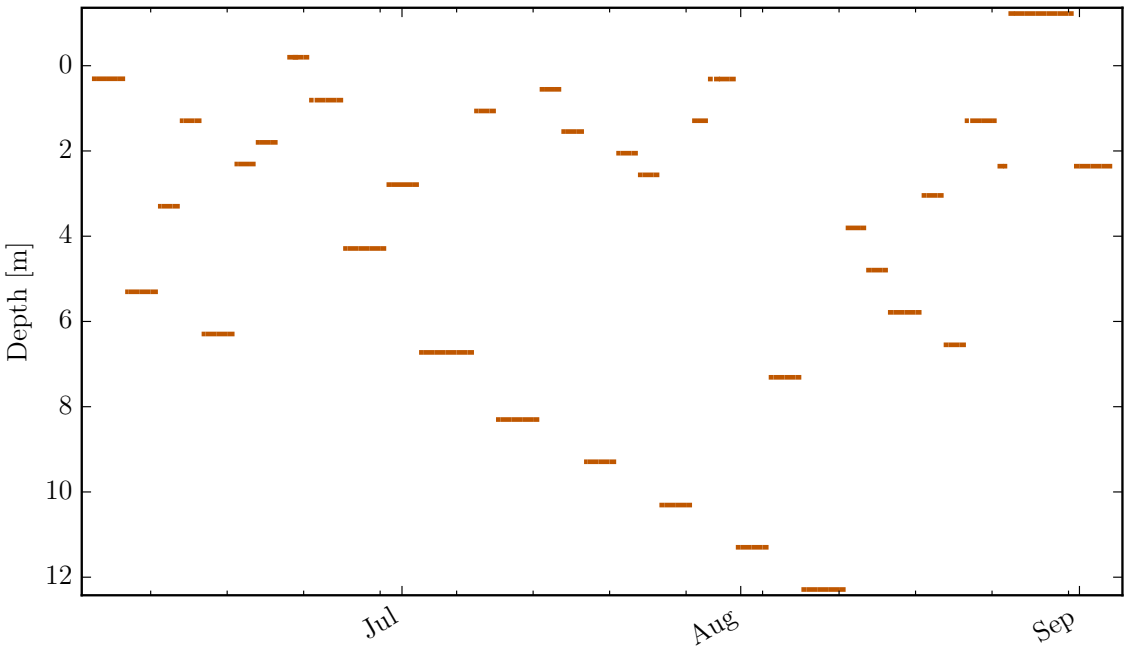


Figure 10.4: The depth to the center of the detector during the course of the experiment. The length of each line indicates the total runtime. The last four depths are not part of the data set, but were several test runs, such as an above water run, a rotated run, and a tilted run.

and nearly level orientation in the original data, and a significant asymmetry was visible data after the event. I began to work on building a set of fits that would recover the original vertical from the data.

Two different methods were performed to fit the recorded distribution to measure the orientation of the detector from the data. The first method was fit using a distribution $A\cos^2(\theta)$ generated from $\theta\,(\phi_d,\,\theta_d)$, where $\theta_d$ and $\phi_d$ are the roll and tilt offset of the detector. The data histogram was summed over the spacial parameters, and the bin center directional vectors were used on the remaining two parameters. Due to the changing solid angle over the $\cot\theta$ bins, it is important to include the solid angle weights from Equation 4.35.

Fits were made using a trust region reflective algorithm on the least squares method to minimize to a $\cos^2\theta$ distribution for each of the three parameters. This fit was made twice, once with $\sigma$ weights based on the counts in each cell, and once

without weights, where $\sigma_i = 1$ for all $i$. The quantity being minimized is

$$\sum_i \left( \frac{A \cos^2(\theta\,(\phi_d,\, \theta_d)) - y_i}{\sigma_i} \right)^2 \tag{10.1}$$

The second method was to put the $\phi_d$ histogram through a Fourier transform, and then the phase of the third component in the transform represents the rotation of the detector. This only provides a single parameter, but provides a different measure of the process.

A 1D dimensional variant of the first method, only fitting $\phi_d$ and summing the $\cot\theta$ bins, as well as the above FFT method, is shown in Figure 10.5. This run had a rotation of $5 \pm 1$ degrees. This was the final run before the enclosure was opened, and was after the detector was transported back to a location where it could be opened. The detector appeared to have gone through an additional rotation during the transport process. After opening the detector, the detector was rotated $-5°$, and the subsequent measurements appeared level.

The final fit values are shown in Figure 10.6. The runs were individually fit using the weighted and unweighted fits described, as well as the FFT method in one dimension. The overall data cube from each run was also fit with the weighted fit, and that is displayed for reference as well. The different fits all show good agreement to within one degree, and individual fluctuations are correlated. Most of the runs remain constant during the span of the measurement at that depth, but a few of them have a consistent change visible in each of the individual runs. Most notably, the surface run after the "event" shows a continuous change of nearly a degree per day, indicating that more rotation occurred during the weekend while the detector was half submerged than in the single event.

The theta direction, or tilt of the detector axis, was measured with both of the two dimensional fits. This was directly related to the relative depth measurements on the davits. The average $\theta_d$ value for the weighted fits to the normal runs was $-0.7° \pm 0.4°$, corresponding to an individual depth uncertainty of 0.3 inches on each cable. There does not appear to be any significant trend for subsequent runs at one depth, giving no indication of slippage on the pulleys during the runs.

Besides the runs that were intended to be level, one set of data was collected at a 6 inch offset, corresponding to a $-5.7°$ tilt. These points can be seen near the end of the running period in Figure 10.7. The fit value was a little less than the expected

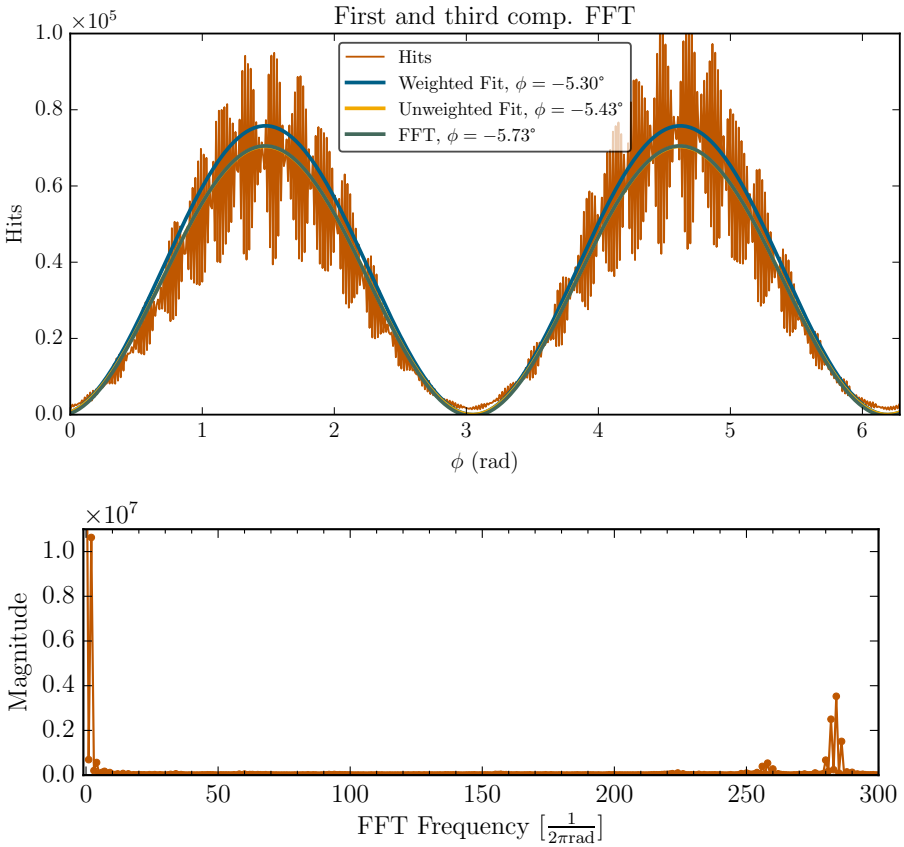


Figure 10.5: Several fitting methods compared for the roll on the $\phi$ histogram from a DataCube from the run after the lake. There was a known rotation of $5 \pm 1°$. The Fourier transform is shown below, with the primary component, and components from the finite strip width aliasing visible.

value, but clearly gets to within 1.4° of the value. The weighted fit does slightly better at recovering the rotation than the unweighted fit.

Due to the barge and nearby shore on one side of the detector, only the open water side of the detector was used for the calculations. After rotation corrections were applied, the data was split by a vertical plane down the axis of the detector in the corrected coordinates. This avoids the barge, as well as the nearby lake shore and hills. The data on the open side of the detector is from an open expanse of water stretching at least 500 m in the half circle remaining.

Making this cut causes the issue of careful measurements of the phi angle to be

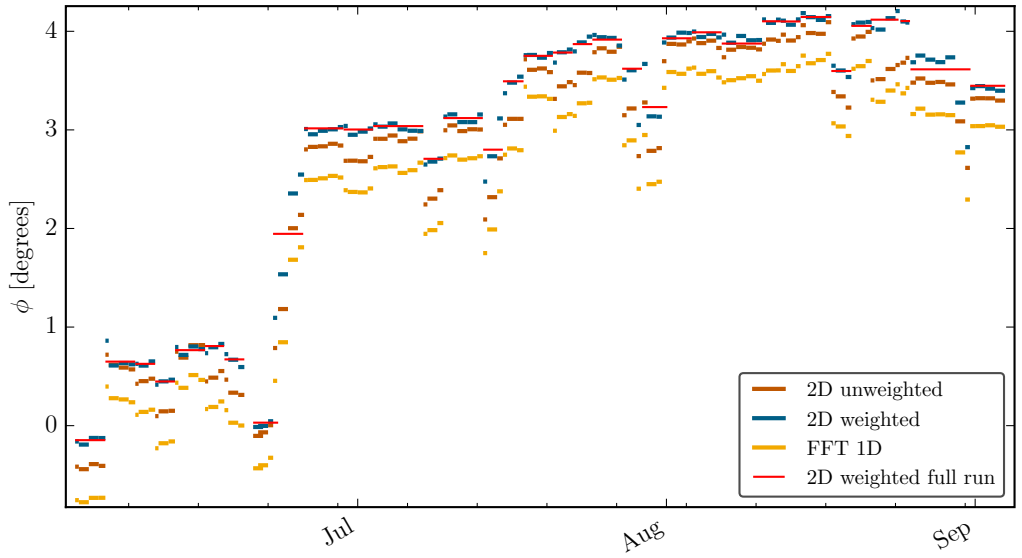


Figure 10.6: Corrections to $\phi$ from several of the described fitting methods. All of the methods provide similar results, to within 1°. The full run fit, which uses the combined run instead of fitting individual runs, is not as effective when the data changes within a single position, such as the rapid change seen in late May when the detector was half submerged. The 2D weighted fit on single runs was deemed best for correcting the data.

significantly more important than if the cut was not being made. In the first two plots in Figure 10.9, the fit value $\phi_d$ and $\theta_d$ have been plotted, along with significant perturbations from the fit of $\pm 3\,\phi_d$. The symmetry of the behavior for the two signs is only seen for symmetric deviations from the fitted value. The values are fairly stable under even significant variances in either value; however, this symmetry is broken by the open water cut that needs to be made. The same values are used in the third plot, but the resulting curves change drastically. This is due increased flux on one side of the $\cos\theta$ circle averaging out with the decreased flux on the other side over the integral in $\phi$, but this is no longer the case when the integral only is over one half of the circle.

To illustrate the difference in the data, Figure 10.8 has the flux curves over $\cos\theta$. The character of the two different curves for each depth indicates that there is a correction needed. The dip seen in the 5.5 m at small $\cos\theta$ is an indicator that the minimum flux does not occur horizontally, like it should. The fit on the right fixes

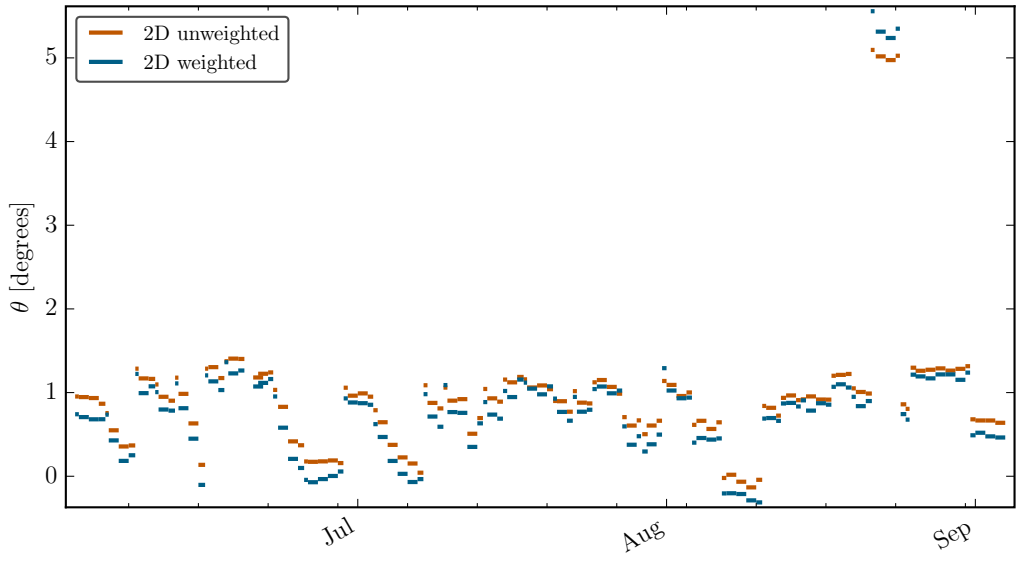


Figure 10.7: Theta corrections from several fitting methods. This component was directly controlled by the depth set on of each davit, and stays between 0 to 1°. A test run with a known offset of 5.7° was run near the end of the time at the lake, and was slightly under fit from both methods, though the weighted fit does slightly better.

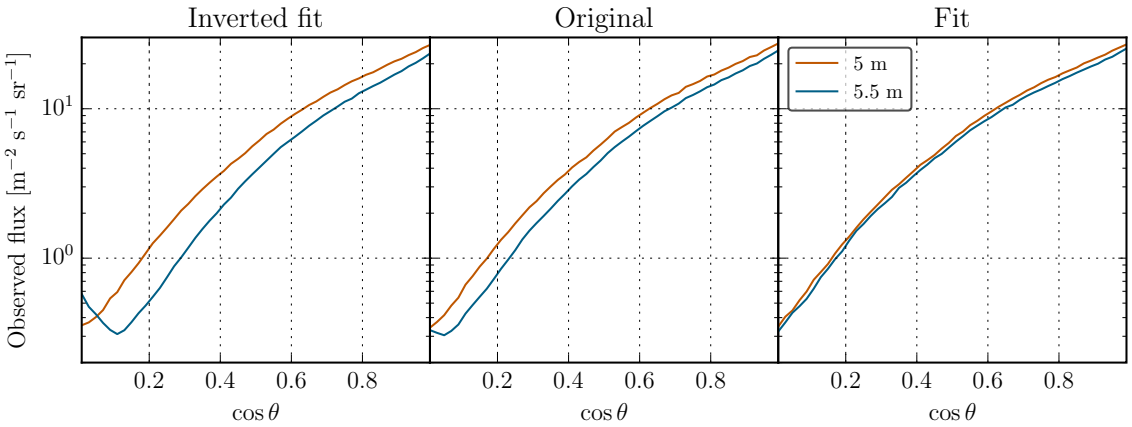


Figure 10.8: The flux vs. $\cos\theta$ for two runs at similar depths but significantly different $\phi_d$ values. The center plot is not corrected for the fit orientation. The values $-$ and $+$ the fit are given on the left and right, respectively. The flux is not corrected for efficiency. Only the fit correction shows the correct scaling behavior at small $\cos\theta$.

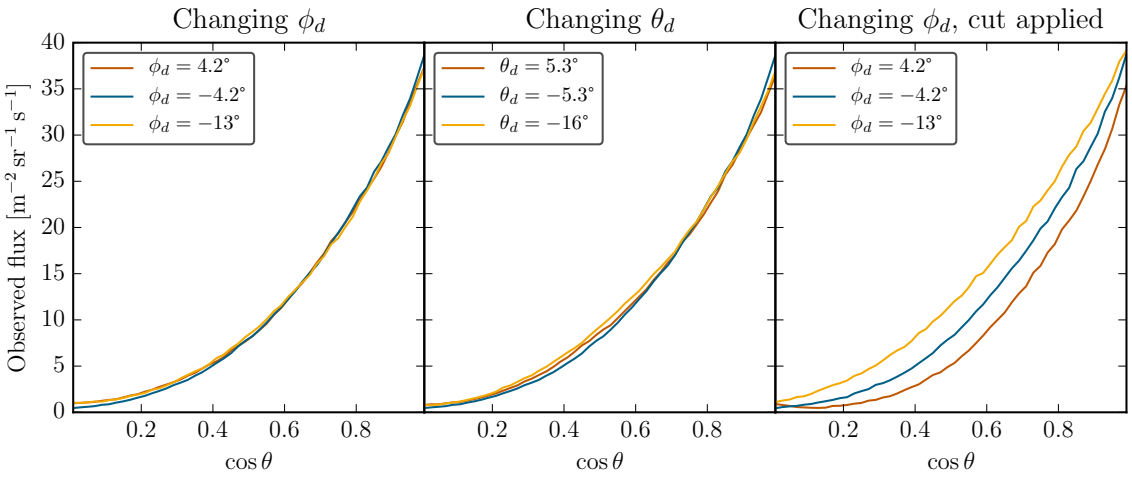


Figure 10.9: Perturbations from the fit (green line) over phi and theta show symmetry in the first and second plots, respectively. The third plot, on the right, is over just the active portion of the detector, and shows the increase to the rotation parameter $\phi_d$ from making the active area selection.

this issue, with a minimum at zero for both curves. The 5 m run was before the event, and has a $\phi_d$ correction of 0.65°, while the 5.5 m run was after the event, and has a $\phi_d$ correction of 4.1°.

## 10.3 Collected Data Coverage

For the purposes of this study, the average path length per position will be sufficient for the analysis of the muon spectrum. However, it is informative to do a full path length calculation to see the actual space covered by the runs.

Each detector sees a variety of different set of path lengths for each angle, due to the geometry of the surface of the water and the geometry of the detector described above. The coverage of path length and $\cos\theta$ was calculated and is shown in Figure 10.10(a). In Figure 10.10(b), the vertical path length, which is directly related to $\zeta$, is shown.

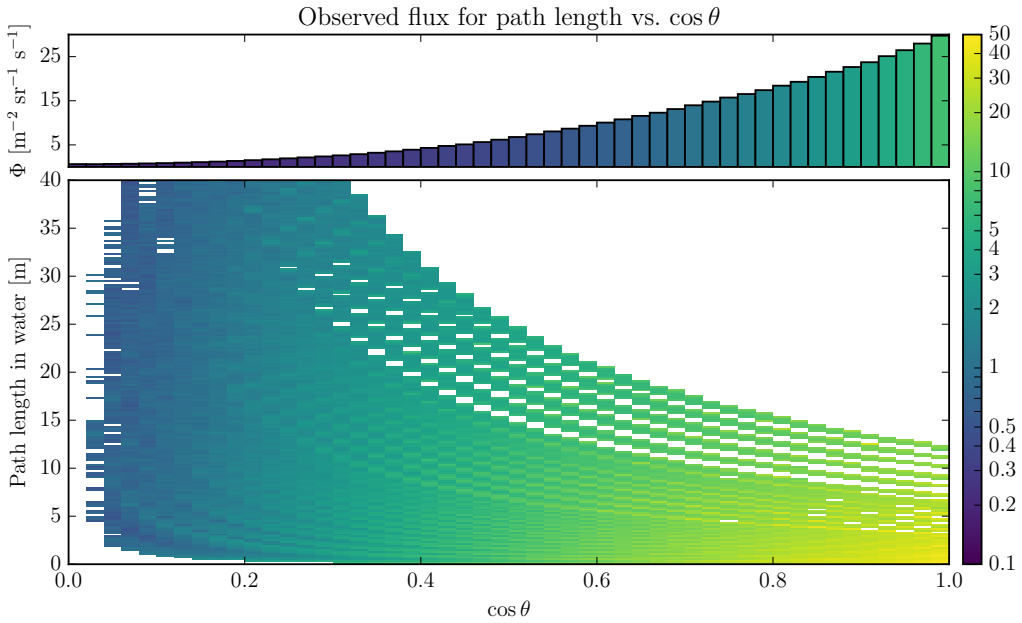


(a) The total path length of each back-projected trajectory through the water.

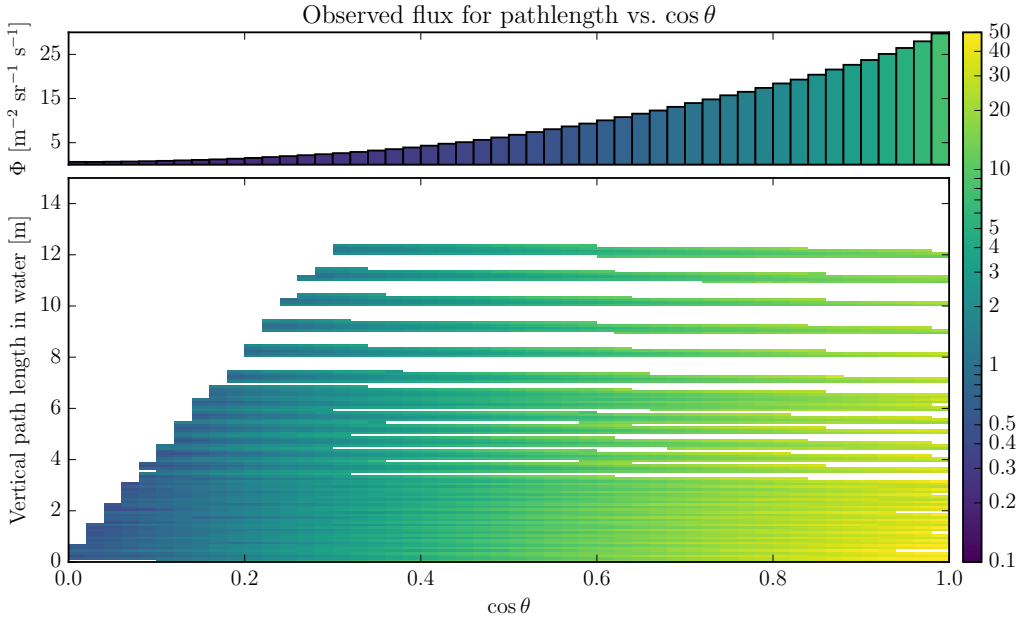


(b) The total vertical path length component, which is related to $p\cos\theta$.

Figure 10.10: The total path lengths, with the color-scale indicating observed flux measured at different $\cos\theta$ values in $\mathrm{m}^{-2}\ \mathrm{sr}^{-1}\ \mathrm{s}^{-1}$. The width of each band comes from the physical geometry of the detector, and the shallow depths overlap.

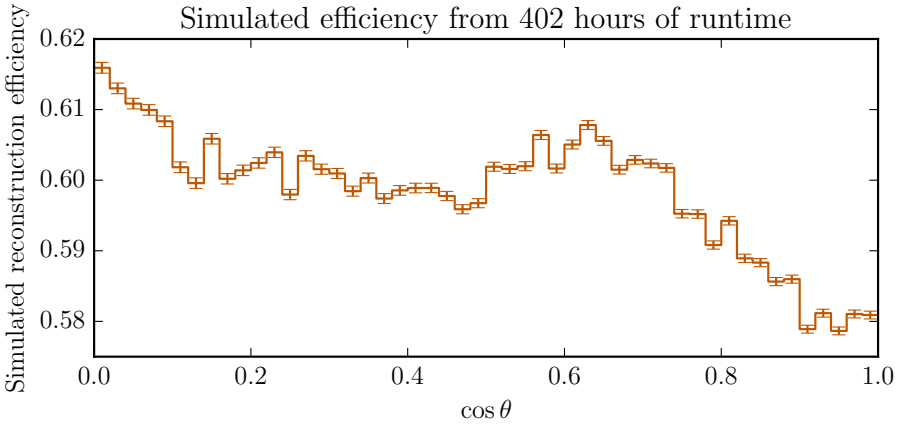


Figure 10.11: Modeled tracking efficiency from Monte Carlo calculation of detector 1 in the horizontal orientation in $\cos\theta$, measured from vertical. Fine structure present from strip design, and large $\cos\theta$ has some extra loss from the detector ends, but overall very even around 0.60. Only tracks that are within the histogram parameter cuts are considered.

## 10.4 Weights

To find the corrected flux from the observed flux, binned over $p_\mu(d)$ and $\cos\theta$, the solid angle in each bin needs to be calculated according to Equation 4.35. The efficiency in each cell was simulated using the Geant4 simulation described earlier, and a modified log Gaussian distribution. By taking $n \to 0$ in Equation 6.2, even statistics are collected across the $\cos\theta$ spectrum. The momentum spectrum retains its characteristics over any given value of $\cos\theta$. The efficiency then is the histogram of reconstructed tracks divided by the histogram from the original generated tracks. The efficiency over $\cos\theta$ is plotted in Figure 10.11.

The strip efficiency model was based on a run from Detector 3 with typical flat-fielding conditions. This model was applied to the geometry of Detector 1, but there still is an overall track rate reduction between the Monte Carlo model reference run and the above water runs after the experiment. This factor, 1.440, is believed to be caused by aging and reduced light transmission from the glue in the strips on detector 1. There are deviations even in an individual detector, depending on the individual configuration and condition of the detector, such as the current thresholds and aging. This factor will be included in the efficiency corrections.

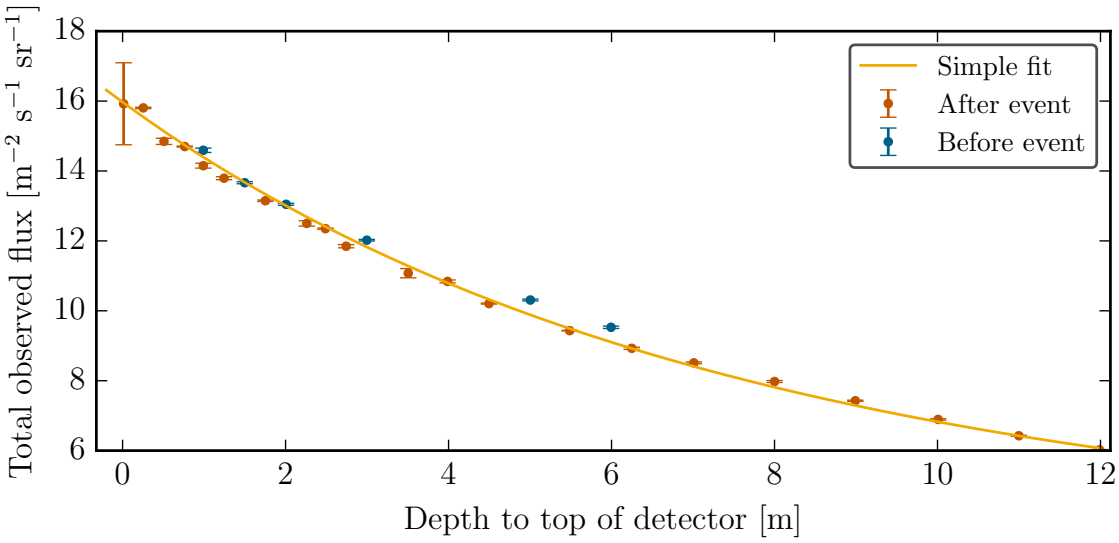


Figure 10.12: Total flux as a function of depth. The data has been categorized by relationship to the event. Flux in this figure has not been corrected for detector efficiency. Error bars are from Poisson statistics and variance between individual runs at each depth.

When plotting the total flux through the detector, which does not depend on the rotation correction, a noticeable change is seen that has a correlation with the event. The post event runs appear to have a slightly lower efficiency. This is visible in Figure 10.12.

A sense of the reproducibility of the runs is given in Figure 10.13. This is from four separate flat fielding runs, to in succession at the lake, and two after the detector returned. There was a 5° offset in $\phi_d$ for the final data sets.

## 10.5 Raw data

Table 10.1 summarizes a selection of the recorded data from the run. Distances here are measured from the surface of the detector to surface of the lake. The counts given in a range of $\theta$ that corresponds to a constant angular acceptance per bin. The flux includes the corrections and efficiency factors discussed above.

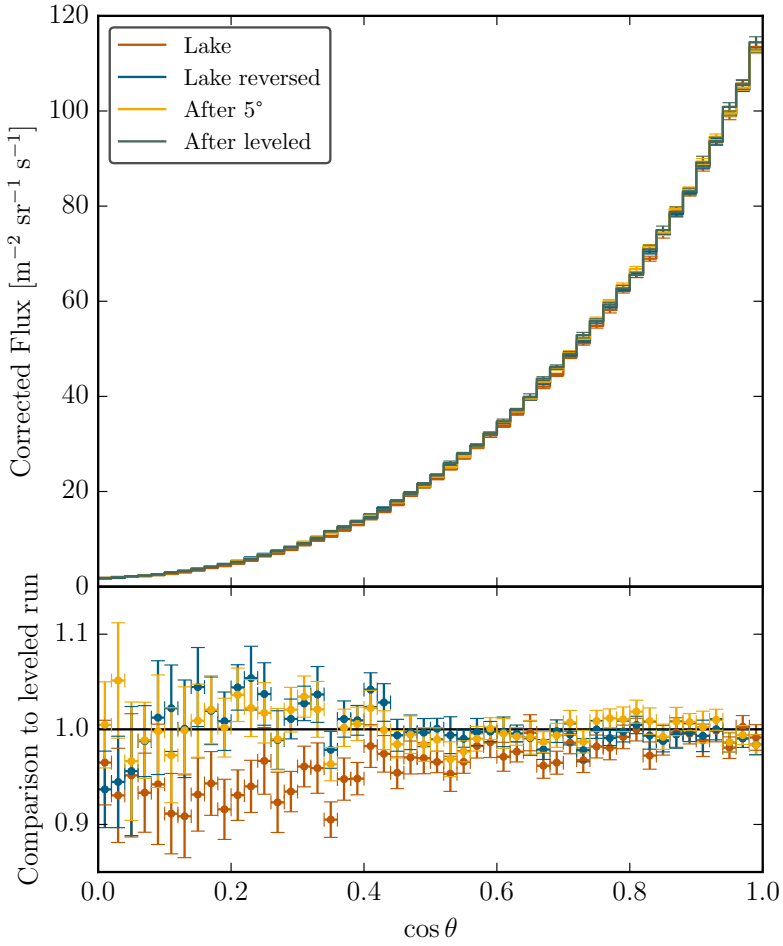


Figure 10.13: Flux in the flat field runs, showing the stability of the detector and the rotation corrections. The first two runs are from the lake, with the detector suspended above the water. One run was made in the same orientation as the final underwater run, and one was rotated 180°about the vertical axis. The final two runs were after the lake experiment, on ARL property, in a field. One was at the final 5° rotation in $\phi_d$, and one was after being leveled. The bottom plot shows the first three data sets divided by the final one.

| | 0.0°- 11.5° | | 34.9°- 36.9° | | 76.1°- 74.9° | |
|---|---|---|---|---|---|---|
| Depth [m] | Hits | Flux [$m^{-2}$ $s^{-1}$ $sr^{-1}$] | Hits | Flux [$m^{-2}$ $s^{-1}$ $sr^{-1}$] | Hits | Flux [$m^{-2}$ $s^{-1}$ $sr^{-1}$] |
| 0.01 | 330838 | $74.4 \pm 3.3$ | 188186 | $44.7 \pm 1.7$ | 8452 | $3.02 \pm 0.15$ |
| 0.25 | 256413 | $73.97 \pm 0.28$ | 147006 | $44.81 \pm 0.15$ | 6682 | $3.06 \pm 0.06$ |
| 0.51 | 366613 | $69.0 \pm 0.4$ | 214109 | $42.6 \pm 0.5$ | 10798 | $3.23 \pm 0.15$ |
| 0.76 | 237708 | $68.10 \pm 0.27$ | 137216 | $41.53 \pm 0.14$ | 6515 | $2.96 \pm 0.04$ |
| 0.99 | 400451 | $66.5 \pm 0.8$ | 237516 | $41.7 \pm 1.0$ | 12217 | $3.22 \pm 0.26$ |
| 1.24 | 228193 | $62.88 \pm 0.19$ | 131746 | $38.36 \pm 0.15$ | 6084 | $2.66 \pm 0.07$ |
| 1.50 | 220663 | $62.97 \pm 0.23$ | 132862 | $40.06 \pm 0.12$ | 7540 | $3.42 \pm 0.04$ |
| 1.75 | 205325 | $59.3 \pm 0.4$ | 119515 | $36.45 \pm 0.14$ | 5477 | $2.51 \pm 0.04$ |
| 2.01 | 200449 | $59.52 \pm 0.16$ | 121180 | $38.02 \pm 0.19$ | 6876 | $3.24 \pm 0.07$ |
| 2.26 | 192691 | $56.02 \pm 0.24$ | 112264 | $34.49 \pm 0.15$ | 5047 | $2.33 \pm 0.04$ |
| 2.49 | 288143 | $55.39 \pm 0.14$ | 170578 | $34.64 \pm 0.13$ | 8225 | $2.51 \pm 0.05$ |
| 2.74 | 187456 | $53.06 \pm 0.15$ | 109947 | $32.88 \pm 0.16$ | 5133 | $2.31 \pm 0.05$ |
| 3.00 | 189882 | $54.20 \pm 0.21$ | 116837 | $35.24 \pm 0.17$ | 6919 | $3.14 \pm 0.05$ |
| 3.51 | 160739 | $48.9 \pm 0.4$ | 94026 | $30.20 \pm 0.18$ | 4423 | $2.14 \pm 0.04$ |
| 3.99 | 331084 | $47.88 \pm 0.20$ | 198648 | $30.35 \pm 0.11$ | 10060 | $2.310 \pm 0.025$ |
| 4.50 | 156093 | $44.77 \pm 0.14$ | 92047 | $27.90 \pm 0.10$ | 4288 | $1.95 \pm 0.05$ |
| 5.00 | 241179 | $45.90 \pm 0.27$ | 148343 | $29.83 \pm 0.12$ | 9016 | $2.725 \pm 0.032$ |
| 5.49 | 221668 | $41.10 \pm 0.11$ | 131439 | $25.75 \pm 0.09$ | 6136 | $1.81 \pm 0.04$ |
| 5.99 | 222350 | $42.07 \pm 0.12$ | 138252 | $27.64 \pm 0.12$ | 8397 | $2.523 \pm 0.029$ |
| 6.25 | 139033 | $38.92 \pm 0.12$ | 82376 | $24.36 \pm 0.09$ | 3767 | $1.675 \pm 0.031$ |
| 6.43 | 349924 | $39.68 \pm 0.15$ | 210135 | $25.18 \pm 0.08$ | 10860 | $1.956 \pm 0.035$ |
| 7.01 | 194316 | $37.11 \pm 0.14$ | 115174 | $23.24 \pm 0.11$ | 5632 | $1.71 \pm 0.04$ |
| 8.00 | 241328 | $34.70 \pm 0.10$ | 145657 | $22.13 \pm 0.11$ | 7749 | $1.77 \pm 0.04$ |
| 8.99 | 165629 | $32.10 \pm 0.09$ | 99104 | $20.30 \pm 0.08$ | 5014 | $1.54 \pm 0.05$ |
| 10.01 | 155746 | $29.75 \pm 0.16$ | 93278 | $18.83 \pm 0.07$ | 4557 | $1.382 \pm 0.032$ |
| 11.00 | 145310 | $27.64 \pm 0.10$ | 87791 | $17.64 \pm 0.07$ | 4394 | $1.327 \pm 0.033$ |
| 11.99 | 183187 | $25.78 \pm 0.11$ | 110524 | $16.44 \pm 0.10$ | 5425 | $1.21 \pm 0.04$ |

Table 10.1: A selection of data from the Lake Travis run. Each depth is shown, along with the total counts collected, and the calculated flux in the bin. The uncertainties come from both Poisson statistics and the standard deviation of the individual one day runs. The runs are colored based on the event date; runs before the event occurred are in orange, runs after the event are in blue. There seems to be an small efficiency change between the two runs.

# Chapter Eleven: The Low Energy Spectrum

The data collected can be used to reconstruct the momentum spectrum over a wide range of angles and from a minimum vertical momentum of 200 MeV/c to 2.9 GeV/c. The fits and efficiency calculations in the previous chapter were applied on a per-run basis.

The data was summed over bins in constant width of $\cos\theta$ and depth $d_c$ corresponding to the center of the detector to the surface. The value of $\cos\theta$ was calculated from the center-of-bin direction $\mathbf{D}$ and the vertical direction $\hat{\mathbf{z}}$ from the $\phi_d$ and $\theta_d$ from the rotation fit on each run. Then $\cos\theta = \mathbf{D} \cdot \mathbf{z}$. The counts, weights, and efficiencies were summed separately for each run. Each unique depth was then combined to produce the master flux histogram. The uncertainty in each bin is a combination of Poisson statistics for the counts, the standard deviation of individual runs at one position, and the uncertainty in the efficiency weights from simulation.

The depth $d_c$ is the vertical component of the path length of the muon through the water. Using a fit to the range tables for water on the PDG given in Figure 2.6, and the threshold of our detector given in Figure 4.8, the relationship between the depth and the minimum momentum for a muon to pass through the detector and get detected is $p_{\min}\cos\theta = 0.2262\,\mathrm{GeV/m} \times d_c + 0.11\,\mathrm{GeV}$. This leads to the natural notation that we have seen earlier, $\zeta_{\min} = p_{\min}\cos\theta$. This will be an effective quantity for the analysis.

The limit on $\cos\theta$ from a geometrical argument using the depth and the open portion of the lake gives us measurements down to 2°; however, the count rate drops at large $\theta$, the angle uncertainty plays a larger role, and multiple scattering from smaller $\theta$ is present, reducing the effectiveness of these bins. For the purposes of this study, I will usually be limiting the analysis to the 75° bin as the largest angle, unless otherwise noted.

The collected data can be seen in Figure 11.1. Here, the actual path length, $p_{\min} = \zeta_{\min}/\cos\theta$, was calculated and used to make the plot, showing the momentum range and a selection of angle ranges with constant solid angle. This sort of plot provides a clear picture of the momentum range that we have captured, but provides very little insight into the structure of the spectrum.

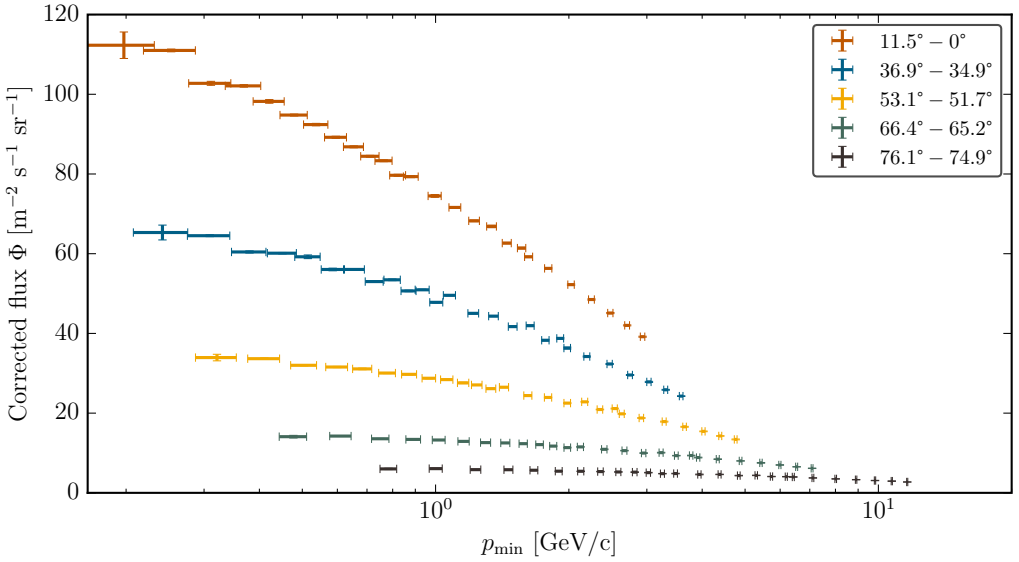


Figure 11.1: The full collected momentum spectrum, at several selected angles. This is the full corrected flux versus the momentum from path length through the water, averaged over the width of the detector.

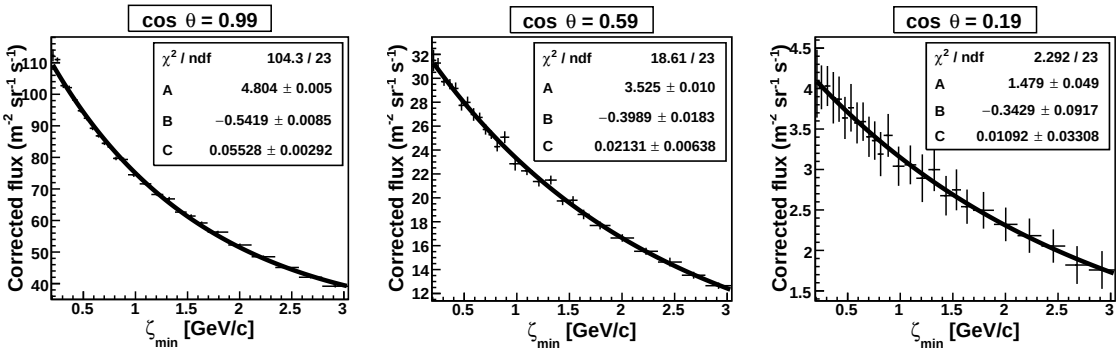


Figure 11.2: The $\zeta$ spectrum for three values of $\cos\theta$, 0.99, 0.59, and 0.19 bin centers. Each bin has a width of 0.02. Fits are of the form $e^{A+Bx+Cx^2}$.

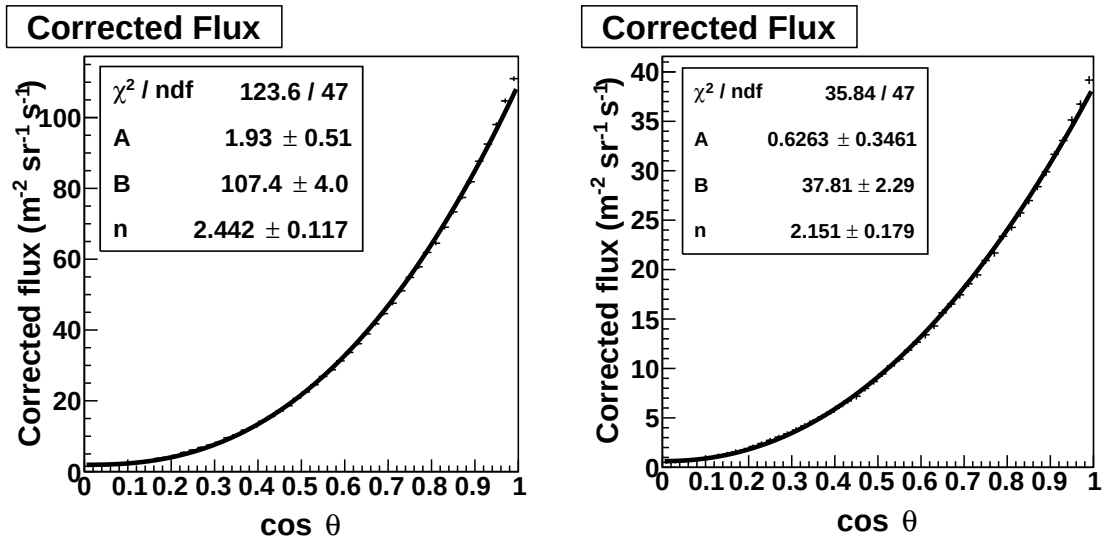


Figure 11.3: The $\cos\theta$ spectrum for two values of $\zeta_{\min}$.

A more natural value for momentum, given the way our measurements were made and the nature of the distribution we expect, is $\zeta_{\min} = p_{\min}\cos\theta$. Selecting three bins covering the active range in $\cos\theta$, Figure 11.2 shows flux as a function of $\zeta_{\min}$, with a simple fit of $e^{A+Bx+Cx^2}$ as a smooth function to model the decay. Even at large angles, the flux remains generally consistent with a smooth decaying function; this is not true if we are not careful to calculate $\phi_d$. The remaining outliers, such as the one around $\zeta_{\min} = 0.8$, are also seen as outliers on the plots of the total flux, Figure 10.12, so corrections to the orientation of the detector cannot be expected to account for the deviations.

Looking at the $\cos\theta$ behavior over constant $\zeta_{\min}$ provides a clue for a phenomenological fit to the distribution. In Figure 11.3, for two different values of $\zeta_{\min}$ on either end of the active range, I have plotted the integral spectrum, and for each, I have a fit with a function of the form

$$A + B\cos^n\theta. \tag{11.1}$$

The fact that this is a good fit, save for a minor deviation at large $\cos\theta$, gives us an idea for a fit to the entire distribution.

If we take slices along $\cot\theta$, and fit each with the above $\cos\theta$ fit, we can monitor the changes in the three parameters across the changing $\zeta$. These parameters, along with the $\chi^2$ for the fits, are shown in Figure 11.4. The first two parameters of

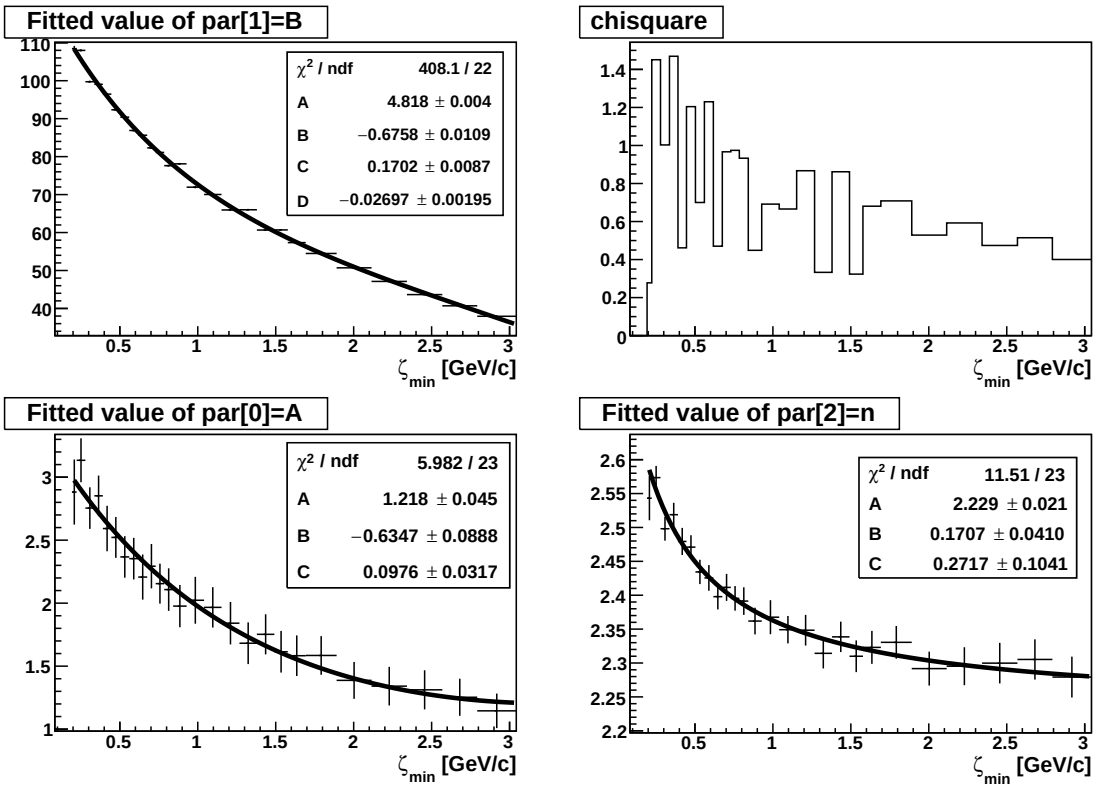


Figure 11.4: Fits to each of the parameters of $n = A + B/(C + \zeta_{\min})$ for slices along $\cos\theta$.

11.1, $A$ and $B$, are fit to exponentials. The $n$ parameters is a bit harder; it should approach $n = 2$ to match the known value for the high energy spectrum, but deviates from that for low momenta, breaking the scaling seen by Reyna. The fit chosen is $n = A + B/(C + \zeta_{\min})$; where $A$ is the value that $n$ approaches as $\zeta_{\min}$ gets large. This value is $2.035 \pm 0.009$, compared to the value seen in other experiments of 2, quoted from the PDG [25]. The fits then, are of the form:

$$A = e^{A_A + B_A\zeta + C_A\zeta^2} \tag{11.2}$$

$$B = e^{A_B + B_B\zeta + C_B\zeta^2 + D_B\zeta^3} \tag{11.3}$$

$$n = A_n + B_n/(C_n + \zeta_{\min}) \tag{11.4}$$

This fit can be then applied to the whole spectrum, as seen in Figure 11.5. The parameters from the previous fits were used as a starting point, with final values from

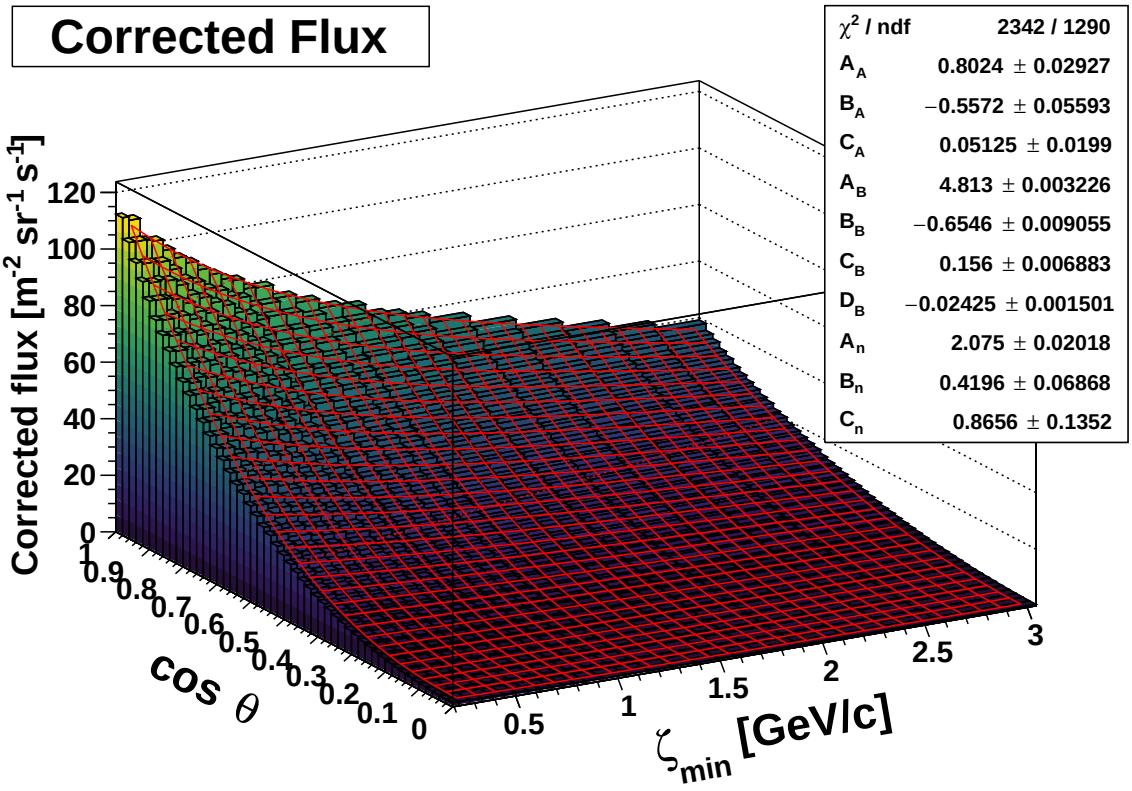


Figure 11.5: Fit to entire integral spectrum.

a minimal $\chi^2$ fit for the full two dimensional function,

$$e^{A_A+B_A\zeta+C_A\zeta^2} + e^{A_B+B_B\zeta+C_B\zeta^2+D_B\zeta^3} \cos^{A_n+\frac{B_n}{(\zeta+C_n)}} \theta. \tag{11.5}$$

This is a comprehensive, phenomenological fit to our data, with good agreement through most of the spectrum. This fit is only valid for the range we covered in the data in $\zeta$, and is intended to provide a basis for numerical predictions from our data.

Reyna [32] found a grouping by spectral shape was possible in the differential spectrum by the plotting $\zeta$ instead of $p$ and introducing a scaling factor $\cos^n \theta$ to the intensity, where best agreement was for $n = 3$. We can apply the same idea to the integral spectrum, for our $n$, as seen in Figure 11.6. General agreement is for lower angles to previously recorded data and Reyna's fit for higher momentums. The breaking seen for the small $\cos\theta$ in the order of the curves is due to the constant term in Equation 11.1 being non-zero, providing a component that is not dependent on $\cos\theta$.

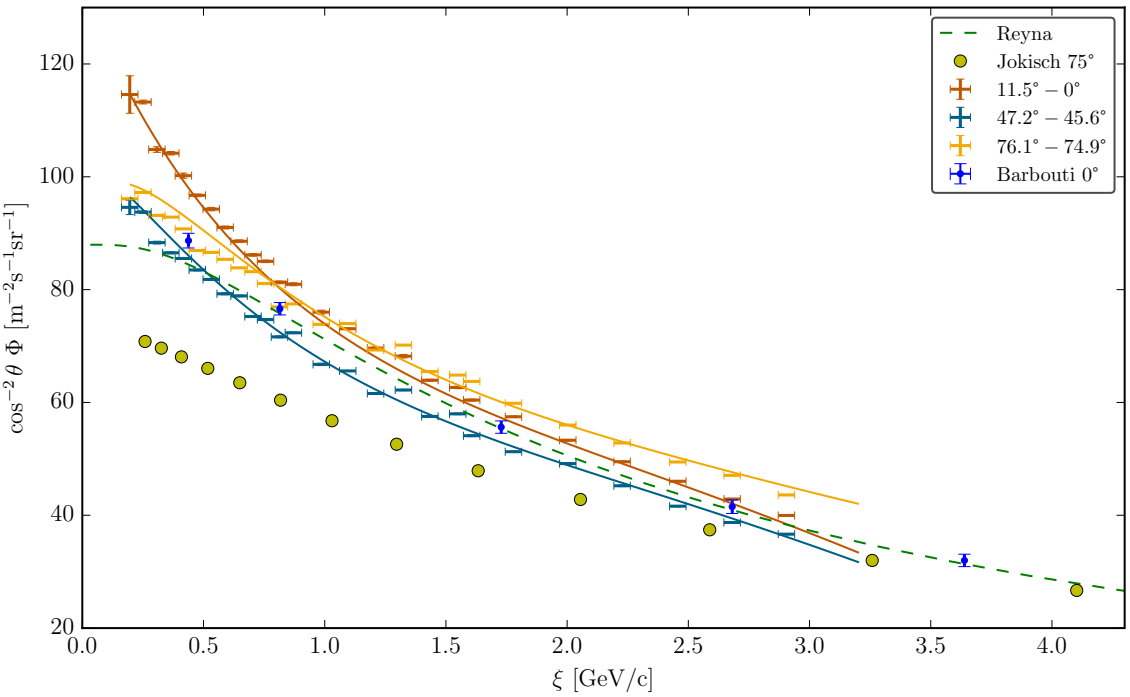


Figure 11.6: Spectrum compared to the fits provided by Reyna [32] and Barbouti and Rastin [31]. Our fit is shown for the midpoint of each angle range.

## 11.1 Attenuation

The non-zero component that breaks our $\cos^n\theta$ dependence model can be investigated by comparing to the above surface runs. Falling back on our imaging methods, we can measure the attenuation of the different runs compared to a flat field, the "After 5°" run from Figure 10.13, the flat field run with the longest run time. The flyseye plots shown in Figure 11.7 were created with the 6 m data. The first plot simply shows the importance of the rotation correction; this run was made about 3° compared to over 5° for the flat field, and this effect dominates the attenuation plot. The second plot, with rotation corrections applied, shows the even attenuation across the unit hemisphere. A small bright rim around 0°is the extra attenuation from the shore; the dimmer rim on the other side is from slightly more attenuation in low $\cos^n\theta$.

Several of the depths have been provided in Figure 11.7. The deeper runs show a slight dip as they go out from vertical, then have a sudden rise and peak for horizontal tracks. There are more shallow tracks above the water than in it, and the effect seems

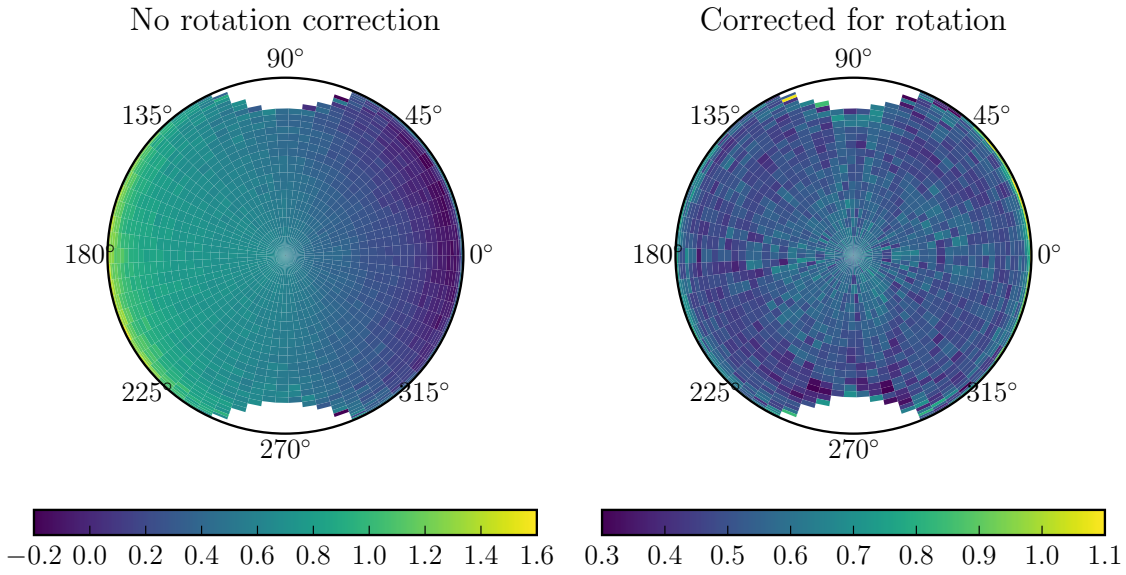


Figure 11.7: Flyseye plots for the attenuation at a depth of 6 m, before and after corrections have been applied to both data and flat field. The nearby shore can be seen around 0°.

to be steady for depths below the near surface run.

As a final visualization of this data, Figure 11.9 shows the data from all the runs. The bright peak along the small $\cos\theta$ bins is seen, along with the "valley" for the central bins.

## 11.2 Vertical Differential Spectrum and Contrast

In order to calculate the contrast, we will need to make a slight modification to our fit. The derivative is sensitive to the curvature at near the ends of the fit, near $p = 3\,\text{GeV}$, so one extra term will be added to the fit, making it $Ae^{P(4)}$, where $P(4)$ is a fourth order polynomial. The values from the fit are given in Table 11.1. This fit is shown in Figure 11.10.

The data is closely spaced in $p$ and has some noise, causing a direct calculation of the differential spectrum to introduce a huge error in $d\Phi/dp$. To avoid this, a moving linear fit to 4, 3, or 2 data points was performed, with the number of points selected to balance the uncertainty between $d\Phi/dp$ and $p$. The uncertainty in $d\Phi/dp$ comes

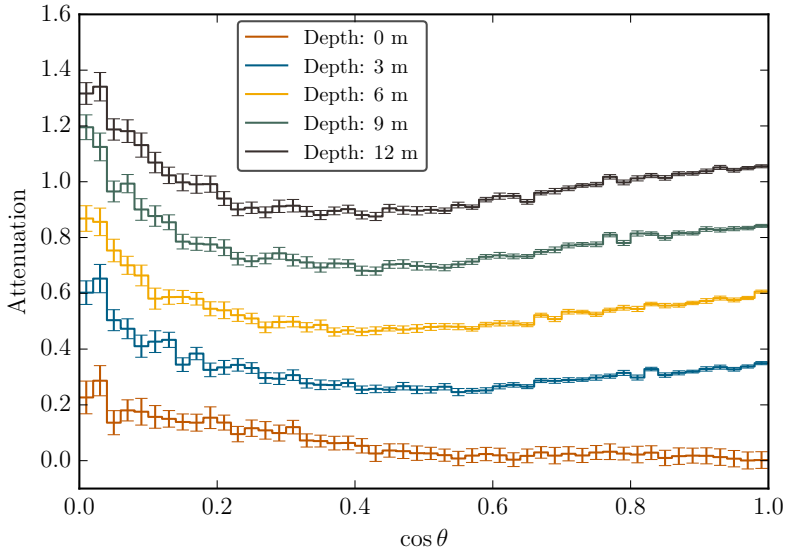


Figure 11.8: The attenuation at several depths, on the open side of the detector only, over $\cos\theta$.

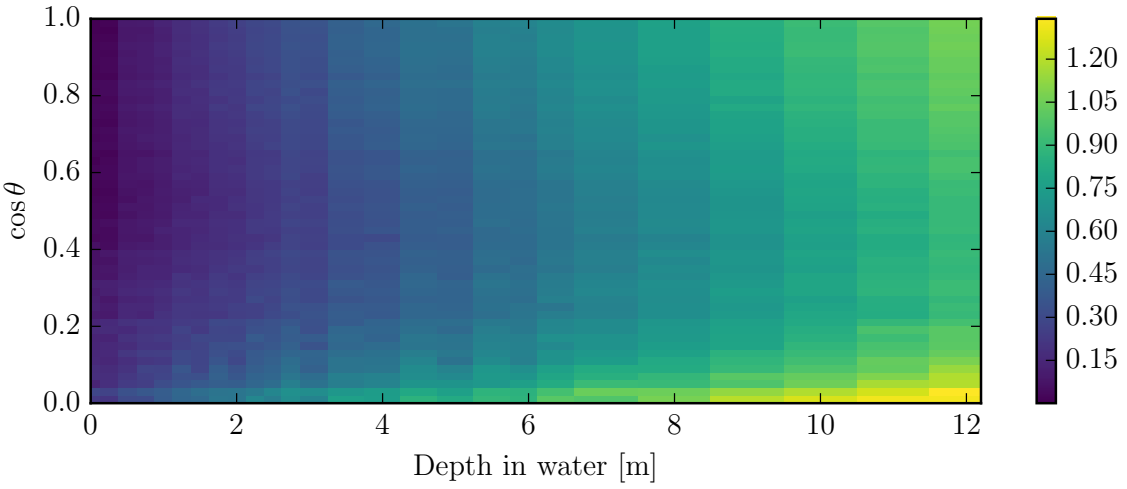


Figure 11.9: The attenuation at all depths, over $\cos\theta$. Again this is only over the open side of the dector.

| Coefficient | value |
|---|---|
| A | $132.9 \pm 0.8\,\mathrm{m}^{-2}\ \mathrm{s}^{-1}\ \mathrm{sr}^{-1}$ |
| B | $-0.855 \pm 0.024$ |
| C | $0.383 \pm 0.030$ |
| D | $-0.125 \pm 0.014$ |
| E | $0.0153 \pm 0.0023$ |

Table 11.1: The vertical fit coefficients from the fit $Ae^{Bp+Cp^2+Dp^3+Ep^4}$, where $p$ is in GeV.

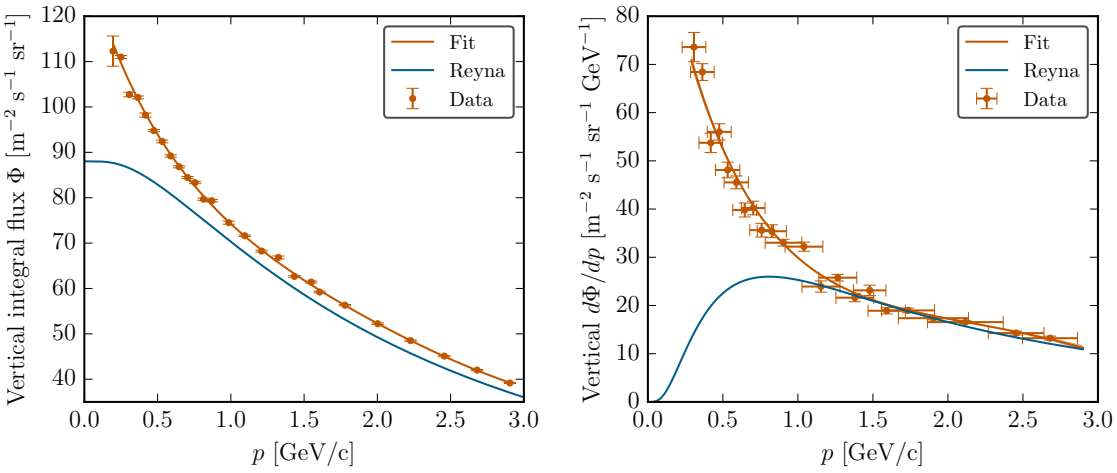


(a) Integral spectrum with an extra term in the fit.

(b) Differential spectrum with the same fit.

Figure 11.10: The vertical spectrum. The Reyna model is shown for comparison.

from the correlation matrix of the fit, and the uncertainty in $p$ comes from the spread of $p$ values used in the fit. The derivative of the previously described fit is also shown.

The goal of this measurement is to accurately predict the image contrast for small targets. The contrast can be directly calculated from a derivative of the integral flux using the following method. The measured flux,

$$\Phi_\mu\left(p_{\min},\,\cos\theta\right) = \int_{p_{\min}}^{\infty} \frac{d\Phi_\mu}{dp}\left(p,\,\cos\theta\right) dp, \tag{11.6}$$

can be used to calculate the attenuation by describing the attenuation as a shift in

$p \to p_{\min} + \Delta$, and by our attenuation definition,

$$D_\mu = -\ln\left[\frac{\Phi_\mu\left(p_{\min} + \Delta,\, \cos\theta\right)}{\Phi_\mu\left(p_{\min},\, \cos\theta\right)}\right]. \tag{11.7}$$

We can expand this for small $\Delta$ as

$$D_\mu \approx -\ln\left[\frac{\Phi_\mu\left(p_{\min},\, \cos\theta\right) - \left.\frac{d\Phi_\mu}{dp}\right|_{p_{\min}} \Delta}{\Phi_\mu\left(p_{\min},\, \cos\theta\right)}\right], \tag{11.8}$$

where we now have a derivative of the integral flux evaluated at $p_{\min}$. This can be rewritten in the form,

$$= \frac{d\ln\Phi_\mu\left(p_{\min},\, \cos\theta\right)}{dp_{\min}}\Delta. \tag{11.9}$$

This is just the contrast function,

$$= C_\mu\left(p_{\min},\, \cos\theta\right)\Delta. \tag{11.10}$$

Using our previous fit, the log of the integral spectrum is just a polynomial, and the contrast is

$$C_\mu = C + 2Dp + 3Ep^2, \tag{11.11}$$

where again $p$ must be in GeV. The contrast above, along with the data, using the same differentiation scheme described earlier, are shown in Figure 11.11. Compared to the previous Reyna prediction, the small depth contrast is drastically improved.

Using a lead brick target, a 12 by 12 inch block, with a height of 8 inches sitting directly above the detector, rotated 45° from the detector axis, we can test this new prediction. This target gives us an attenuation of $0.278 \pm 0.035$ inside the area shown in Figure 11.12. The previous model would predict, from the 2.2 mwe thickness of the cube, an attenuation of 0.113. The new model predicts an attenuation of 0.294. This is much improved over the previous model, and is in good agreement with the measurement.

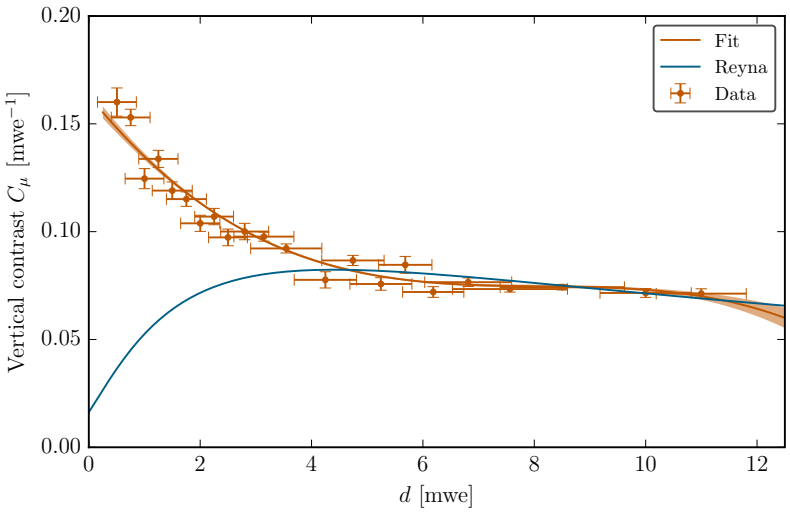


Figure 11.11: The contrast observed in the vertical spectrum. The shaded band indicates the uncertainty from the correlation matrix of the fit. The Reyna model is shown for comparison.

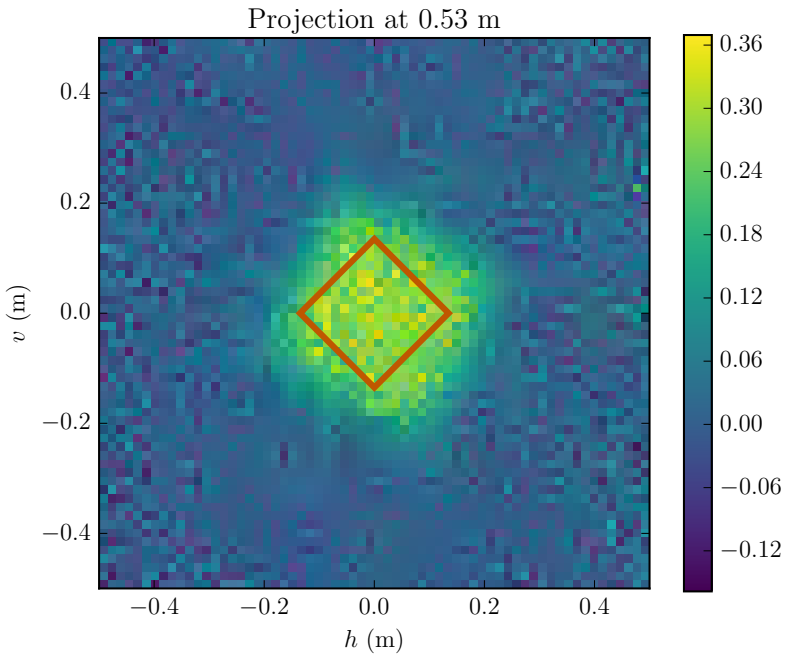


Figure 11.12: The attenuation of a lead cube, $12 \times 12 \times 8$ inches, averaged over a 7.5 inch square through the center of the target. The attenuation in the square is $0.278 \pm 0.035$.

# Chapter Twelve: Project Belize

I would like to conclude with one more imaging project that is currently underway. Two of our detectors were transported to the La Milpa archaeological site in Belize, where they are recording data next to a sealed Mayan pyramid known as Structure 3. The difficulties associated with running our detectors in remote conditions without external power are briefly highlighted here. An image of the pyramid is presented, showing the latest data from the project. The work started here will continue for several years, ultimately resolving the interior of the pyramid to the level of detail required for the detection of undiscovered voids or architecture.

## 12.1 The Power System

Detector 3 and Detector 4 were shipped to Belize in the summer of 2013. The first year, we set them up each with a generator and two deep discharge 6 V batteries. They were in the horizontal orientation. The tanks on the generators were filled every day to provide continuous operation. This power system lasted just under a week. On the first Sunday after starting the detectors, the local workers were unable to buy gas for the generators, causing the batteries to completely discharge. We were never able to revive that system, and put the detectors in storage for that year.

We spent the next year designing and preparing a solar system. In the summer of 2014, we returned to Belize and put in a 14 panel solar system. They were connected to a system of 48 6 V batteries. A clearing some distance from the site was selected for the construction of the system. There was very limited exposure to the sky, but

| Year | Det 3 [days] | Det 4 [days] |
|---|---|---|
| 2013 | 5.49 | 4.12 |
| 2014 | 25.0 | 26.0 |
| 2015 | 95.2 | 84.9 |
| 2016 | 10.4 | 11.4 |

Table 12.1: Total collected run time.

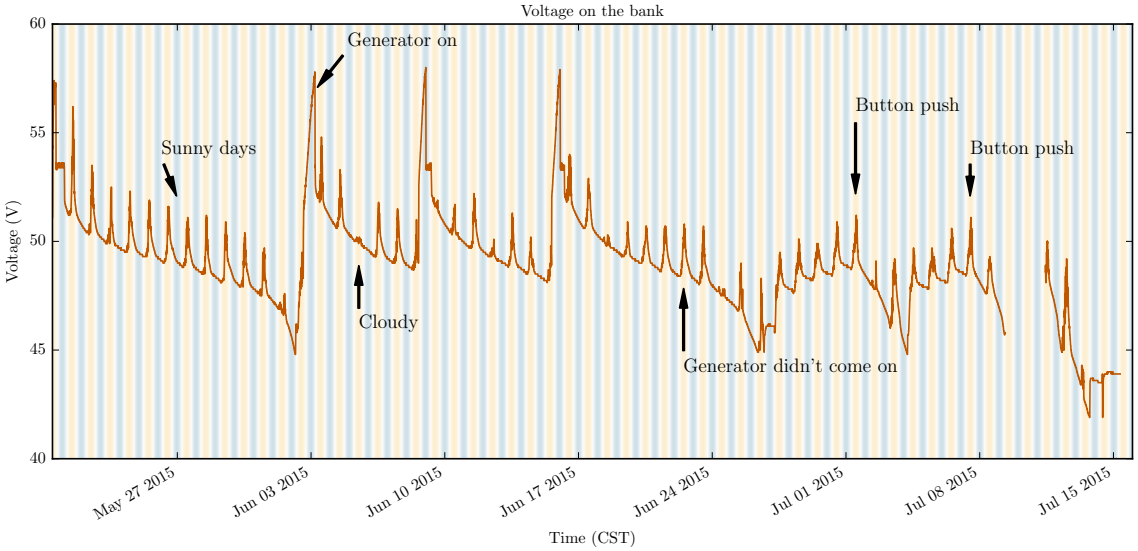


Figure 12.1: The voltage logs during a difficult period, annotated with interpretations. The color patter indicates the day/night cycle.

we were seeing at least several panels with full sun for 6-8 hours every day. The entire system was in full sun for just 2-3 hours during that time.

To reduce the power loss over the 300 m distance between the panels and the detectors, we converted the internal power supplies on the detectors to run at 48 V input. Although we had converted a system at UT Austin to run on 48 V successfully, both detectors in Belize would not run successfully with a high voltage supply running on 48 V, noise levels were too high to manage. The final solution was to run a separate 12 V line just for the high voltage, and to get the power from "tapping" a subset of the battery bank. The high voltage supply draws a very low current, so the power loss on the 12 V would be small.

This system lasted longer than the generator solution, but still had several issues that limited the data collection. The draw on the extra 12 V line was higher than originally anticipated, and the batteries under the extra load were discharging at a significantly different rate. Although intended in the original design, there was not a working hysteresis loop in the charging cycle, causing the detectors to come on immediately when the sun came out, and never managing to make it to the first point that data was written to the flash memory after one hour of run time.

| Det | Location | Run [days] |
|---|---|---|
| 3 | 2013 | 5.49 |
| 4 | 2013 | 4.12 |
| 3 | 2014 | 85.2 |
| 4 | 2014 | 61.5 |
| 3 | 2014 - rotated | 35.0 |
| 4 | 2014 - rotated | 56.6 |
| 3 | 2016 | 10.4 |
| 4 | 2016 | 11.4 |

Table 12.2: Run time per position. Positions are named by the year that the detectors were moved.

The first fix to these problem was installing a large generator for the battery bank. A manual switch was added for reactivating the system after the low voltage disconnect activated. A voltage logger was also added to help with the analysis of the performance of the system. In Figure 12.1, the voltage on the bank is seen as a function of time during a period in 2015. The periods when the system was on can be seen as a downward sloping sawtooth pattern. The generator activation can be seen three times, once per week, until the week of the 17th of June. The generator had mechanical difficulties, so during the last portion of the graph the system was entirely on solar power. There is an upward trend until the button was pushed, indicating that the system was charging under solar power.

At the end of 2015 and beginning of 2016, a new relay system was installed, with proper hysteresis; the system had to stay above a certain voltage for 18 hours; this avoids false triggers when the bank is being charged during the day. The tapped lines were replace with a 48 V to 12 V power supply at the solar system site, and the tapped batteries were replaced. This system was stable enough to gather data consistently. The collected run times for each year are visible in Table 12.1.

There were several sites prepared for the detectors. They are shown in Figure 12.3, and the run times are listed in 12.2.

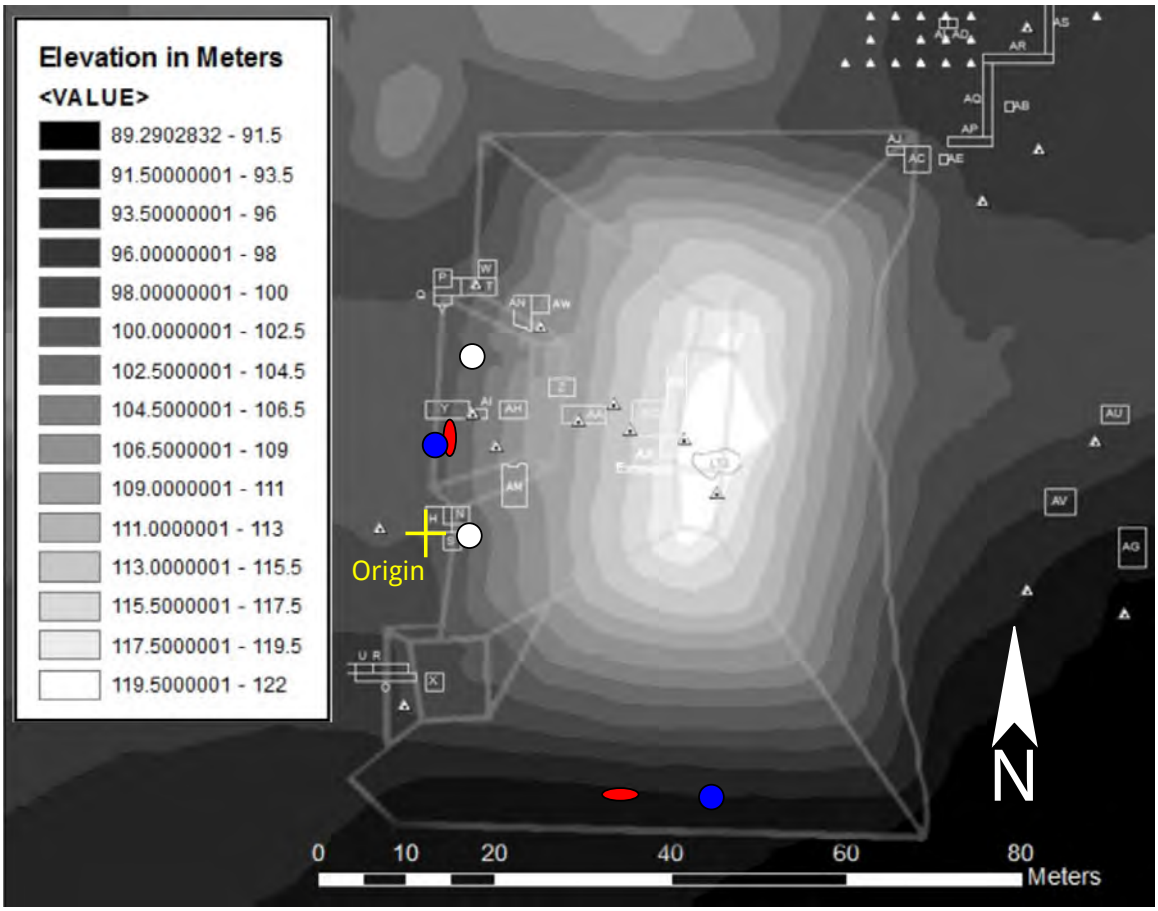


Figure 12.2: Topographic map, provided by field director Debora Train. ● 2013 horizontal locations, ○ 2014 locations, and ● 2016 locations.

## 12.2 The Images

A topographic map of the site is given in Figure 12.2. The detectors and the origin is marked on the topographic map. For each pair of locations, the northern detector is always detector 3. The 2016 locations are nearly the same as the 2013 locations, only now the detectors are vertical, and we hope to get far more run time.

A current image, with the data listed in Table 12.2, is shown in Figure 12.3. This image uses several of the techniques listed in the previous chapters. This is a projection onto a plane 16 m from the (100,100,100) point assigned by the archaeologists, near the base of the pyramid. The variable binning scheme has been used to keep nearly constant statistical error across the image. There are several features in this

image that can be seen more clearly with a high pass filter. In Figure 12.4, the same plane is shown with such a filter. The outline of the pyramid is seen coming down to just past (0,20) and then turning sharply to form the southern face. The trench and the cave directly west of the northern most detector location can be seen jutting into the pyramid.

## 12.3 Conclusion

Muon tomography has proven to be a powerful tool for investigating a wide variety of problems. I have shown a assortment of tools for reconstruction and analysis with portable muon detectors. While the system produces useful images without a knowledge of the underlying spectrum and the detector response, these things are needed to understand the contrast visible in the images.

I have demonstrated the expected threshold in momentum, tracking resolution, and efficiency of our detector through calculations and Monte Carlo simulation, providing the best description to date of the performance of our detectors. This knowledge became valuable in the spectrum measurement. I have also covered the detector track reconstruction software, and have improved the analysis that can be collected during a run.

A careful measurement of the low energy muon spectrum has added a much better description of the 110 MeV to 1.2 GeV spectrum, while reproducing the previous results found in literature for 1.2 GeV to 2.7 GeV. This is proving valuable for interpreting images of smaller targets.

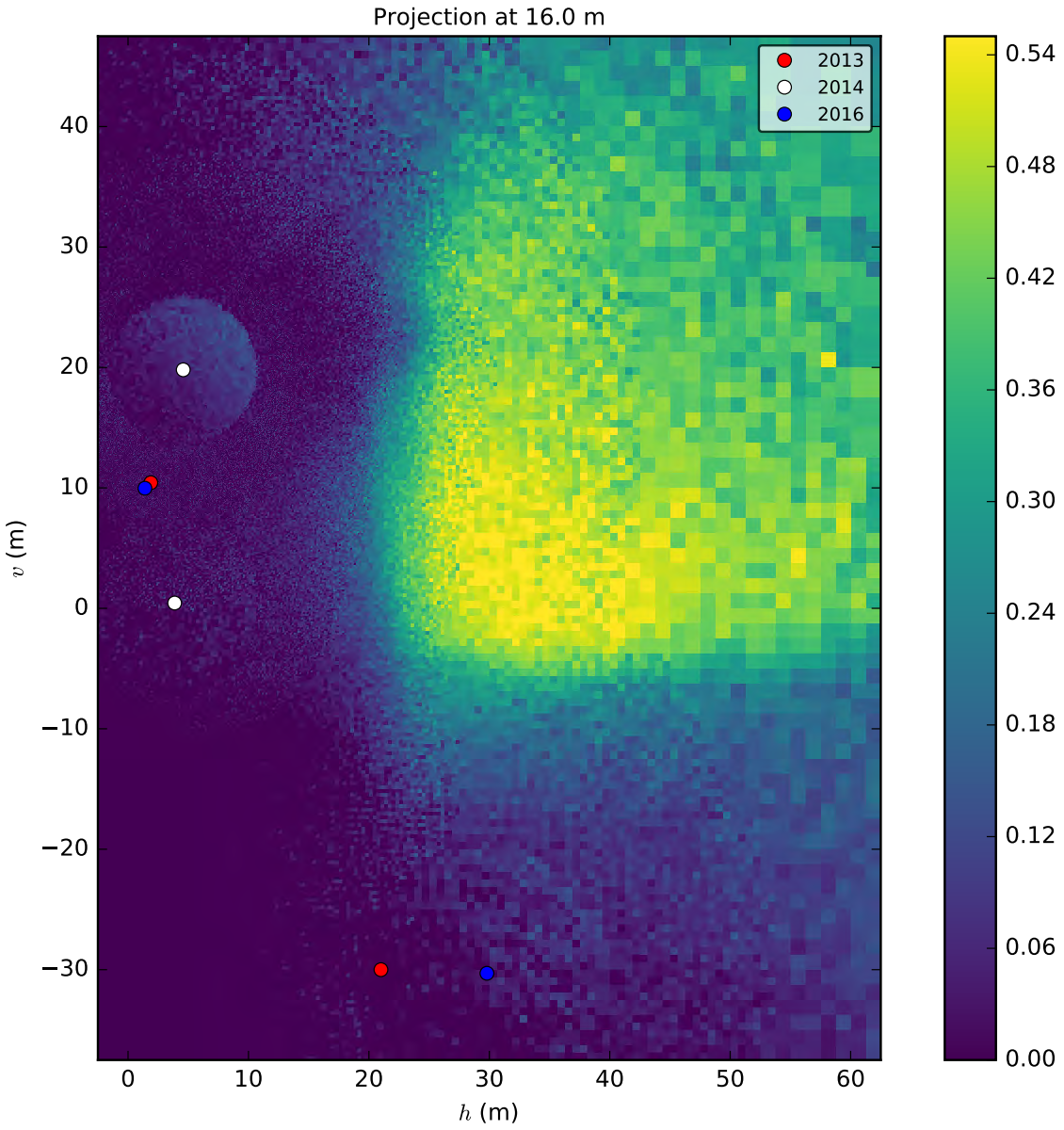


Figure 12.3: The Belize data, projected at 16 m. The detector locations are shown as points. The "shadow" effect can be seen on the far side of the pyramid, since any muon on that side must past through the pyramid (and attenuate) before reaching the detector.

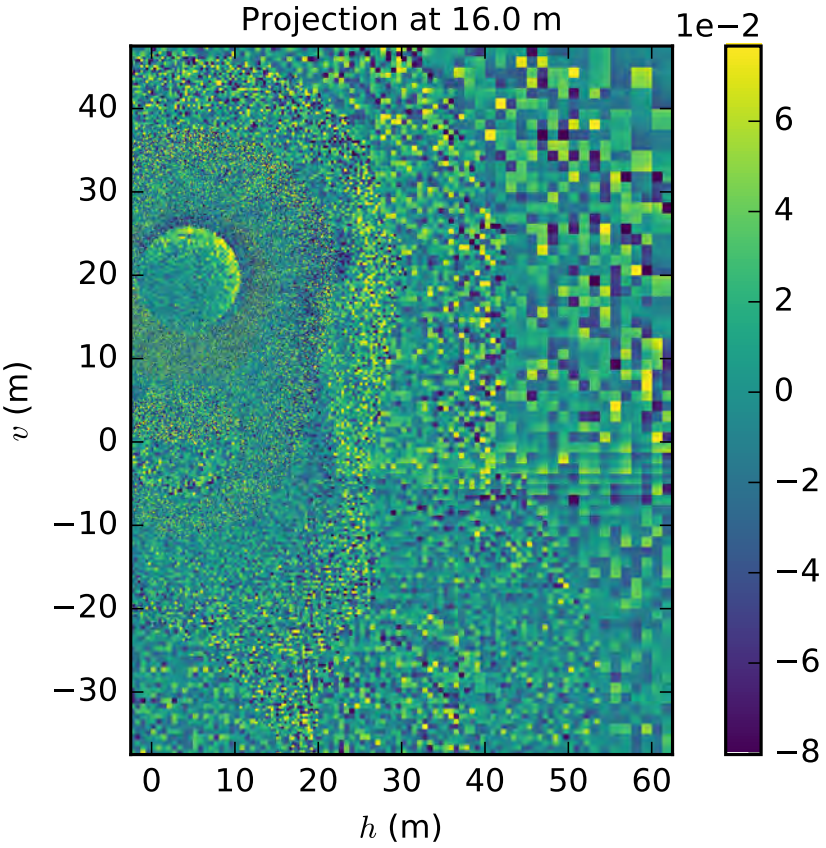


Figure 12.4: The Belize data with a high-pass filter, projected at 16 m. The south west corner of the pyramid is visible, as is a small known cave directly across from one of the detector positions at $v = 20$ m.

# Appendix A: Raw Data

## A.1 Introduction

This note covers the matlab tracking code and algorithms. A new naming scheme is introduced, and future expansion is also covered. Carefully analyzing the work flow was necessary in preparation for the creation of a Geant4 simulation.

## A.2 Data Flow

The current system consists of several steps. First, the data is produced in the detector. This is output in three forms. A metafile, '.meta', holds running conditions in plain text. A sample file, '.samp.bin', holds a few seconds of raw output from the detector. This is a binary listing of strip number hit and timestamp. The final file is a 30+ MB uncompressed histogram file, '.hist.dat'. This stores some basic information about the run and the 18,000,000 histogram bins.

The next step is the conversion of raw data and metafile to matlab histogram. This is done either through strips resting in Maya1, or using histtomat('filename'), being careful not to include either of the extensions. This uses a matlab algorithm to read the data. A built in static class method, DataCube.frombinary, also can read the files. Once saved as a structure in a matlab format, it is possible to leverage the rest of the data processing workflow, including the gui.

## A.3 Reconstruction Parameters

It is necessary to name and track the various parameters used in reconstruction. Here I'll outline the basic parameters and their uses.

### A.3.1 Global Parameters

The global parameter structure will be called PAR and is loaded using initdetparam(). A local version can be created by collecting an output from initdetparam(). Par

consists of the following parts:

#### A.3.1.1 World Values

There are several global constants in PAR. They are PAR.world.x, PAR.world.y, and PAR.world.z; as well as PAR.world.R. These are the directions of the basis vectors; using them ensures flexible code. They are not always used in the current implementation and are assumed to always be x=[1 0 0], etc.

#### A.3.1.2 Detector Orientation

The location and rotation of the detector are part of initdetparam() and are changed after loading or in the file. The rotation of the detector is PAR.ori.x, PAR.ori.y, and PAR.ori.z, along with the rotation matrix PAR.ori.R. The location of the detector is PAR.ori.center.

#### A.3.1.3 Detector Specifics

readparamfile('filename') will return a structure from the parameter file. These values were given similar names to in the PAR structure. The length for the detector is stored as PAR.det.length

#### A.3.1.4 Layers

Layer contents are all in three vectors indicating the strip, with the inner strip 1, middle strip 2, and outer strip 3. The data is in PAR.layer.radius for the strip center radii, a PAR.layer.N for the number of strips in a layer, and PAR.layer.omega for the wrap angles. Computed angles, theta, for the intersection of the strip with the end of the detector, are stored in PAR.layer.theta.

#### A.3.1.5 Lists

There are several lists of values for strips. The individual strip locations are stored in PAR.list.phi, as numeric arrays in a 3 cell array. PAR.list.phi{2}(3) would be the second layer, 3rd strip. The other two lists are 448 element arrays with two values each. The first is PAR.list.daqmap, which gives [layer number, strip number] for each daq number, which is the index -1. Similarly, PAR.list.febmap has [feb, channel] for

each daq-1 address. A calculated convenience parameter is PAR.list.idaq, a cell array of arrays with the daq numbers+1 in strip coordinates.

#### A.3.1.6 Strip

The strip width and thickness are in PAR.strip.width and PAR.strip.thickness.

#### A.3.1.7 Cut

PAR.cut.b and PAR.cut.chisq are stored here.

#### A.3.1.8 Other

PAR.other.energythreshold, PAR.other.minstripshit, PAR.other.lambda, PAR.other.description, and PAR.other.clockrate are stored here.

## A.4 Tracks

The tracking system builds a polygonal model of the detector, and calculates the pathlength through each strip $\rho$ and the distance from the sensor along the axis $z$ or corrected for the strip length $z_{eff}$. Assuming an attenuation length $d$, the intensity at the sensor is then

$$I \propto A\rho e^{-\frac{z}{d}}$$

Selecting a proportionality constant, $A$, we can trigger on $I > I_{trigger}$.

## A.5 Functions Available

### A.5.1 Tracking Function Set

Notice that x,p are in world frame, while D,O are in detector frame.

**initdetpar()** This sets up the PAR variable. Optionally returns PAR. PAR is global, allowing user edits after initialization. Notice that initdetpar will not reload PAR if it exists. Use clear global to remove PAR.

**readparamfile(file)** Reads a parameter file, returns a structure with identical names.

**visualizecan()** This draws the cylinder shape of the detector.

**visualizeline(p,x)** This draws a line through the detector that intersects the edges. p is direction, x is a point on the line.

**visualizestrips(hits)** This will draw strips hit. Takes either simple or regular hitlist output

**visualizestripshit(p,x)** This will compute and draw the hits.

**visualizestripshitsimple(p,x)** This will compute and draw the hits. Only uses strip centers (simple algorithm)

**linecylintersect(r,D,O)** This intersects a radius r cylinder with a line at O in direction D.

**linecylangle(r,D,O)** This intersects a radius r cylinder with a line at O in direction D, but outputs cyl coords.

**triangulate(faces)** This will split up a face index array into a triangle face index array.

**spiralfromquad(quad,height,delta,res)** Spirals up the points in quad up height around delta with res points.

**spiralfrompoint(point,height,delta,res)** Spirals a point up height around delta with res points. Centered at 0.

**rotateto(array,angle)** Rotates points in array by angle.

**polylist(faces,points)** Makes a list of points for each face, appended into a giant array.

**stripshit(p,x)** Lists all strips hit, using raytracing. Outputs [strip layer, strip number, path length through strip, pathlength to sensor; ...]

**stripshitsimple(p,x)** Lists all strips hit, using simple, classic model. Outputs [strip layer, strip number; ...]

**makefourpoints(diameter,width,thickness)** Makes a quad at angle 0.

**hitcan(p,x,radius,length)** Checks to see if the line hit the detector cylinder, including finite detector length.

**guessstriphit(p,x,rad,startingangle,numstrips,delta,leng)** Outputs 2 hit strip values (not integers)

**computestriphitsimple(param,impact,unit,layer)** This is used by the old strip hit program.

**facelist(resolution)** Produces a face index array, includes end caps.

**detmodel()** Returns a model of the detector, and faces. Resolution is hardcoded in at 32, but is easy to change.

**inversedaq(daq)** Returns the inverse of the daq list. Used in initdetparam.

**hitlisttodaq(hitlist)** This creates a daqlist of hits. This does not yet have a light from strip model, but has a place for one. It is in actual daq numbers (not daq + 1)

**cell2daq(hits arrays)** This makes a daqlist stream of hit strips from a cell array of hit strips, spaced appropriately in time (10 timestamps).

**genTRX()** This will generate a track set. Returns ps, xs, and time.

**plotsTRX(ps,xs)** This will view the generated tracks. Makes several plots. No input params will cause it to use genTRX.

**g4totracklist** This is a script that handles the conversion to .samp.bin. It will not overwrite an old file.

# Appendix B: Detector Software Manual

## B.1 Installation

| |
|---|
| *Note on easy installation in Matlab 2012b or newer*: all four main programs can be installed in a single click each by running the four `.mlappinstall` files in `hfunction/quickinstall`. They will be in the 'Apps' tab in Matlab and can be run from there. |

The Plane Viewer suite of tools are comprised of set of Matlab GUI apps. Because Matlab cannot access a file unless it is in the Matlab path, you must set up the path before running the apps.

#### B.1.0.1 Setting the Path

To run the gui, the four folders (`hfunction/gui`, `hfunction/helper`, `hfunction/-compiled`, and `hfunction/class`) must be in the Matlab path (Open Matlab, (file menu) set path → add folder, save path). A shortcut can be made to each of the apps in `hfunction/gui`, or the name of the app can be typed at a Matlab prompt. To make a shortcut, the following is an example target:

```
"C:/Program Files/MATLAB/R2012b/bin/matlab.exe" /nosplash /n-
odesktop /r "RawDataConverter;quit"
```

The addition of quit to the string must not be used with either `PlaneViewer` or `StackViewer`. Names are typed without spaces.

#### B.1.0.2 Compiled Files

Note that there are some compiled "mex" files in `hfunction/compiled`; these should be available for both 32 and 64 bit windows systems. If a new compilation is needed, the source is provided in `hfunction/mexfiles`. Run `compileall` to compile all files.

#### B.1.0.3 App Descriptions

Here are simple descriptions of the four apps. More detailed information follows

**Raw Data Converter** This asks for a folder containing raw detector files then processes everything that folder into `.mat` files.

**Run Combiner** This allows you to select multiple `.mat` files and combine them into one `.mat` file. Options are given to combine runs or leave runs separate in that single file.

**Plane Viewer** This is the main analysis app. Planes can be provided and projected to. Many options are presented.

**Stack Viewer** This is a viewer for the stacks that you can create in Plane Viewer. Completely optional; all functionality is now in Plane Viewer. Useful for post-analysis.

### B.1.1 Data Acquisition

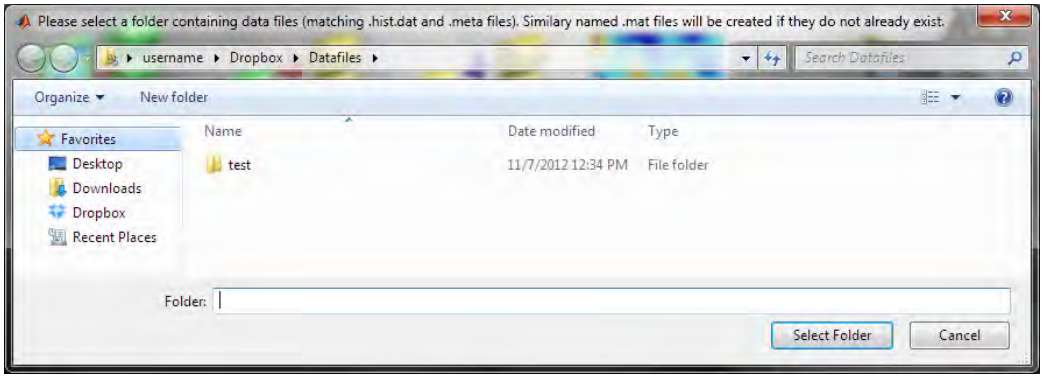


Figure B.1: Raw Data Converter

Detector control is managed through DetGUI tools[1]. A run (one time period of data) is comprised of three files. The name is the time and date of the run. All information taken by the detector is stored in a histogram in the 34 MB file `name.hist.dat`. A short sample of the run is stored in `name.samp.bin`[2]. The run information (provided by the user before the run was taken) is in `name.meta`. These

[1]See previous note on running DetGUI

[2]This is not stored in the `.mat` files; this used to be used primarily for basic detector testing.

three files can be compressed by some versions of DetGUI into a single `.gz` zipped file that can be unzipped by 7-zip and other tools.

Conversion of these raw intermediate files into `.mat` files, the standard storage and working file format, is done through either the main server application on maya1, or locally with the RawDataConverter app. Only the `.mat` files are needed for future reconstruction.

To run RawDataConverter, simple run the app and choose a directory that contains one or more set of raw files. It will quickly convert all files to `.mat`s, leaving the original files intact. It will not uncompress a `.gz` file; please do that manually first if needed. 7-zip allows multiple files to be unzipped at once.

You now can rename files, as well as choose odd names like ones that start with a number or contain spaces[3].

### B.1.2 Data Preparation

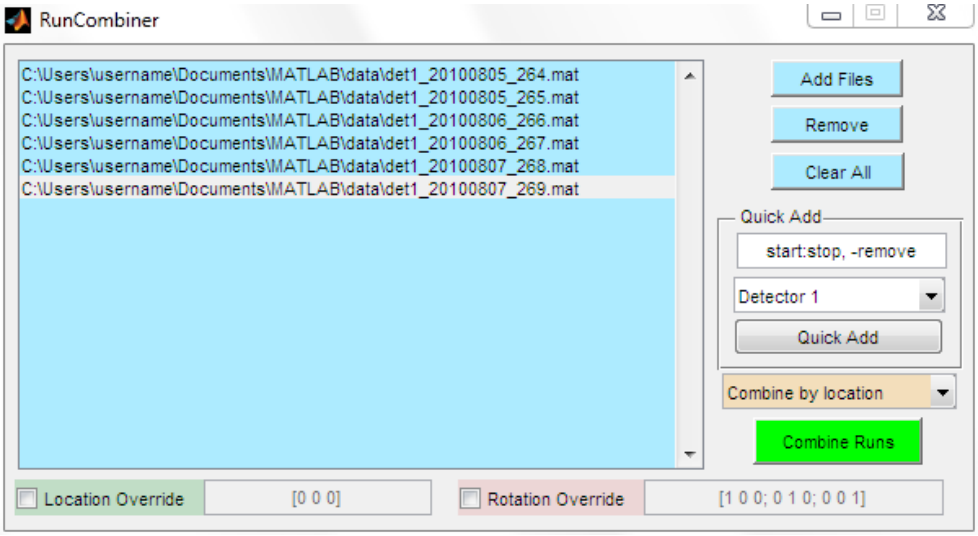


Figure B.2: Run Combiner

You must create single data files that contain all the run information you need to process. [4] This allows adding several consecutive runs, for example. Simple build

[3]Best naming practices usually do not contain extra spaces or dots or other symbols, or numbers at the beginning of the name. The underscore is perfectly fine and recommended.

[4]Using the command line object oriented interface eliminates this restriction.

a list of all files that need to be combined using Add Files, Remove, and Clear All. Once you have a list, the Combine Runs button will complete the operation, and ask you for an output file name.

Quick Add allows you to quickly add run ranges, as long as you are using the predefined directory for storing data (edit `hfunction/helper/aquiredir.m` to change or add a directory for a single username). Use the format 3:5 to add runs 3, 4, and 5, comma separated lists and negative values (exclude from previous) work also. As a final example, 1:100, 125, -50 would add runs 1 through 100 excluding 50, and 125.

The system can combine the data as a list, or sum it together. A drop-down below the quick add section controls this behavior. The default, add by location, will sum everything at matching locations and almost always is the best choice.

Finally, you also have the option to override the location or rotation for the cubes. This is useful if you have a lot of cubes that were mistakenly entered when DetGUI ran.

### B.1.3 Imaging Your Data

This is the primary tool in the system. Use the upper-right buttons to add a file to use as background and a file to use as the foreground. As soon as the files are loaded, the plane will be projected if auto-preview is checked. Uncheck and manually push preview if you are on a slow system or projecting a large multi-location `.mat` file. The orientation of the plane can be selected from the orientation drop-down, and if a valid Matlab $3 \times 3$ matrix is input in the custom orientation box, that will override the drop-down box[5]. The center and size of the plane can be entered below that, as well as the bin size. Along with the display option, which shows different representations of the data. The 3D display in the lower right shows a simple representation of the situation, and can be rotated by dragging with the mouse.

Stack options, in the upper left, allow you to set a step size and a total length to step. Stacks are always along the normal to the image. These are used in the stack menu, allowing a numbered stack of planes in any image format or a stack file (used with the optional stacking system) to be saved.

Range and Contours, along with filter and flatten, control the image and do not require recalculation. These options allow you to adjust the image to pinpoint

[5]Warning: any Matlab code entered here is executed.

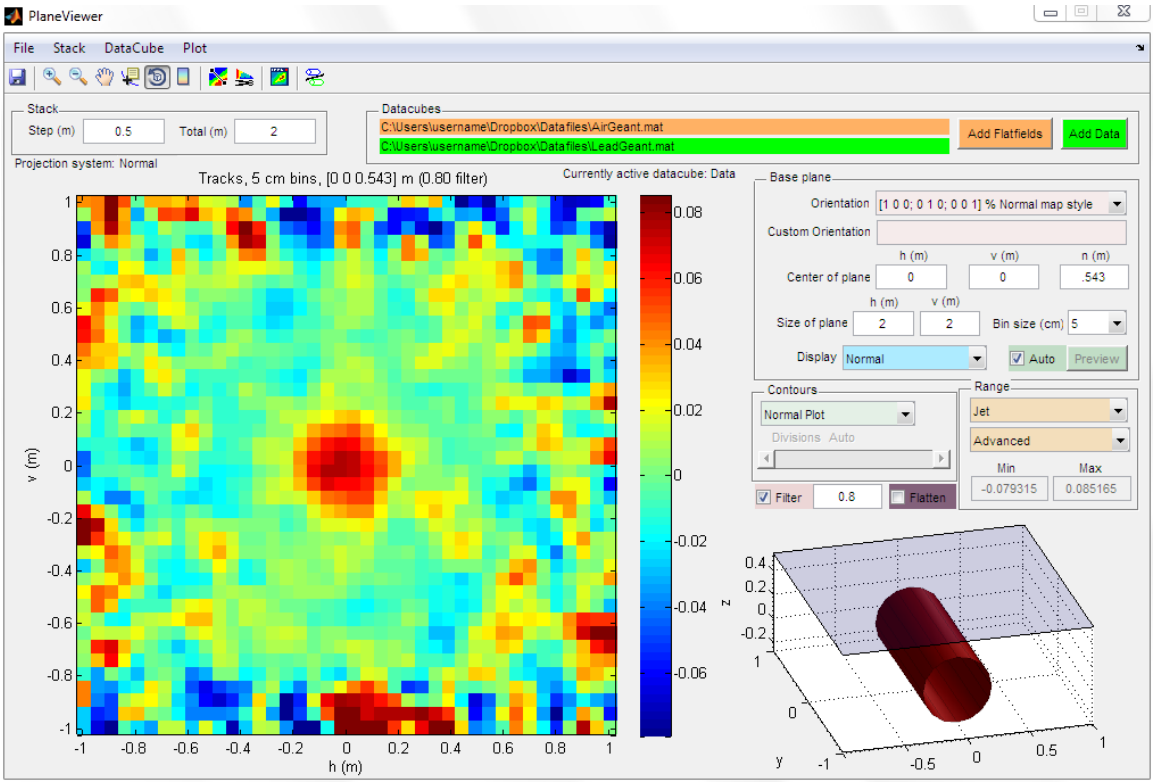


Figure B.3: Plane Viewer

features. Range adjust the visible color range; you can choose to use traditional range (maximum to minimum), advanced range (average $\pm 3\sigma$), or manually set and adjust the limits. Filter adds a Gaussian blur with an adjustable amount. Flatten will try to take out the best fit plane from the image, to reduce overall slopes/tilts. WARNING: Filter seems to be occasionally unstable. Select it last. Also, running contour on unfiltered data can be slow.


Figure B.4: Plane Viewer toolbar

The toolbar at the top shows several important common tools. Counting from left to right (see Figure B.4), the options are

1. Save current projection.
2. Magnify area in image.
3. Zoom back out to normal magnification.
4. Drag the image when magnified.
5. Toggle. Click when this is selected to display a cursor with coordinates and value at those coordinates. Right click on plot with this tool on for more options. Useful for checking an attenuation value at a single location, or locating a feature.
6. Toggle. Rotation button. Plane Viewer tries to handle this automatically for you. Leave this alone unless the 3D lower-right view gets stuck.
7. Color bar. Toggle the color bar on the side.
8. Cross-section. Turn this on then click two or more times on the image, then press enter to see a lineout 1D or 2D cross-section for your chosen lines.
9. Snip. Draw an area to get statistics for that area. You can draw multiple areas or modify the current one before finalizing and getting statistics.
10. Separate plot. Makes a separate Matlab plot that can be adjusted easily using the full Matlab plot GUI for publication quality output.
11. Swap data/flat-field. Only works if supported by your data (multi-location data cannot be used as flat-field)

Finally, the menu system allows a few more useful features. The file menu has options to save and load the current settings to a file, along with the ability to change the projection system. This is useful if you are experiencing instability or don't have a compiled projection system on your PC. The current system is displayed below the Stack settings.

The Stacks menu has already been discussed, and the DataCube menu has options that affect the active cube file. You can see the active cube (data or flat-field) right below the DataCubes selector. Besides the ability to toggle the active cube, you can

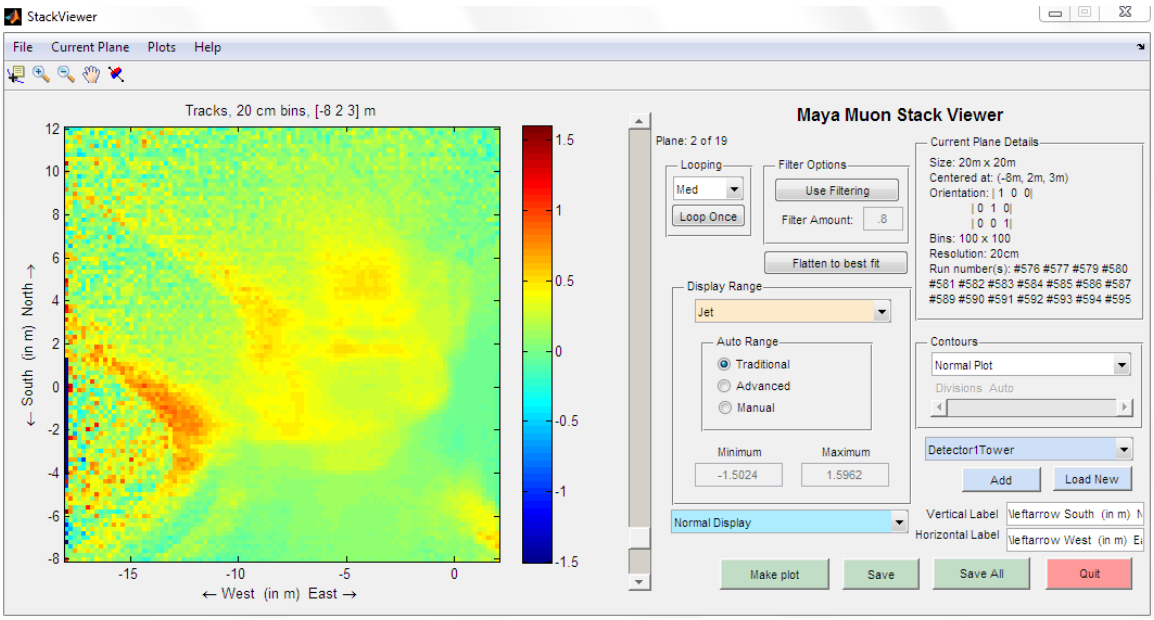


Figure B.5: Stack Viewer

also get a printout of the information stored in this cube, or one of several useful plots.

The Plot menu has copies of the common plot commands, and the ability to rename the axes and set the ground level (for nicer title display).

Behind Plane Viewer there is a white simple Matlab instance. Some unnecessary information is occasionally output here, along with useful error information if there was a user or program error. It needs to be manually closed when Plane Viewer is closed.

### B.1.4 Optional Stacking System

This is optional; the only reason it still exists is to easily view pre-rendered images in a stack. Nothing is significantly different than in Plane Viewer, except the ability to select from multiple stacks in a file.

## B.2 Matlab Classes and Functions

### B.2.1 Installation

The command line interface is comprised mainly of classes powered by helper functions and a few compiled files. Because Matlab cannot access a file unless it is in the Matlab path, you must set up the path before using the classes.

#### B.2.1.1 Setting the Path

To run the normal tools, three folders (`hfunction/helper`, `hfunction/compiled`, and `hfunction/class`) must be in the Matlab path (Open Matlab, (file menu) set path → add folder, save path).

#### B.2.1.2 Compiled Files

Note that there are some compiled "mex" files in `hfunction/compiled`; these should be available for both 32 and 64 bit windows systems. If a new compilation is needed, the source is provided in `hfunction/mexfiles`.

### B.2.2 Command Line Interface

#### B.2.2.1 Documentation and Overview

The command line Matlab interface is self documented. Just type `doc`, then one of the following four commands: `DataCube`, `Planes`, `Scans`, or `Sweeps`. These are the four classes that represent everything in the Plane Viewer Suite.

A DataCube is a class that represents DataCubes. For compatibility reasons, it should always be stored as a classicdatacube (methods included for conversion and saving). Scans is a class that holds multiple data DataCubes and one flat-field DataCube. Planes represents a physical plane in space, and has a projection method that takes DataCubes or Scans. Sweeps is used to store and project multiple planes (used by StackViewer).

#### B.2.2.2 DataCube

This is the main workhorse of the classes, and it represents a single detector run. Load a file with `myrun = DataCube('name of file');`, and then use your newly created variable's methods to analysis the cube. Tab key will show you the available methods.

# Bibliography


[1] E. P. George, "Cosmic rays measure overburden of tunnel," *Commonwealth Engineer*, vol. 455, Jul. 1955 (cit. on p. 1).

[2] L. W. Alvarez *et al.*, "Search for hidden chambers in the pyramids," *Science*, vol. 167, no. 3919, pp. 832–839, Feb. 1970. [Online]. Available: http://www4.rcf.bnl.gov/~edmundo/alvarezpyramids.pdf (cit. on pp. 1, 2).

[3] C. G. Wohl, "Scientist as detective: Luis Alvarez and the pyramid burial chambers, the JFK assassination, and the end of the dinosaurs," *American Journal of Physics*, vol. 75, no. 11, pp. 968–977, 2007. [Online]. Available: http://www.6911norfolk.com/d0lbln/105f06/105f06-wohl-alvarez.pdf (cit. on p. 1).

[4] K. Nagamine, M. Iwasaki, K. Shimomura, and K. Ishida, "Method of probing inner-structure of geophysical substance with the horizontal cosmic-ray muons and possible application to volcanic eruption prediction," *Nuclear Instruments and Methods in Physics Research Section A: Accelerators, Spectrometers, Detectors and Associated Equipment*, vol. 356, no. 2–3, pp. 585–595, 1995, ISSN: 0168-9002. DOI: http://dx.doi.org/10.1016/0168-9002(94)01169-9. [Online]. Available: http://www.sciencedirect.com/science/article/pii/0168900294011699 (cit. on p. 2).

[5] K. Nagamine, "Geo-tomographic observation of inner-structure of volcano with cosmic-ray muons," *Journal of Geography (Chigaku Zasshi)*, vol. 104, no. 7, pp. 998–1007, 1995. DOI: 10.5026/jgeography.104.7_998. [Online]. Available: http://dx.doi.org/10.5026/jgeography.104.7_998 (cit. on p. 2).

[6] H. Tanaka *et al.*, "Development of a two-fold segmented detection system for near horizontally cosmic-ray muons to probe the internal structure of a volcano," *Nuclear Instruments and Methods in Physics Research Section A: Accelerators, Spectrometers, Detectors and Associated Equipment*, vol. 507, no. 3, pp. 657–669, 2003, ISSN: 0168-9002. [Online]. Available: http://www.sciencedirect.com/science/article/pii/S016890020301372X (cit. on p. 2).

[7] J. Marteau *et al.*, "Muons tomography applied to geosciences and volcanology," *Nuclear Instruments and Methods in Physics Research Section A: Accelerators, Spectrometers, Detectors and Associated Equipment*, vol. 695, pp. 23–28, 2012, New Developments in Photodetection NDIP11, ISSN: 0168-9002. DOI: http://dx.doi.org/10.1016/j.nima.2011.11.061. [Online]. Available: http://www.sciencedirect.com/science/article/pii/S016890021102105X (cit. on p. 2).

[8] V. Gentry, "Design and construction of a 1024 channel muon tracking telescope," Senior Thesis, University of Texas at Austin, May 2014 (cit. on p. 2).

[9] R. F. Schwitters, "A detector for muon tomography," The Maya Muon Group, Conceptual Design Report, Jun. 2004. [Online]. Available: http://www.hep.utexas.edu/mayamuon/files/papers/cdr.pdf (cit. on pp. 2, 17, 44).

[10] L. Allen *et al.*, "Technologies for the detection and monitoring of clandestine underground tunnels, Fall 2007," Global Innovation and Strategy Center Omaha NE Intern Program, Final Report Project 07-03, Jan. 2008, Accession Number : ADA497908. [Online]. Available: http://oai.dtic.mil/oai/oai?verb=getRecord&metadataPrefix=html&identifier=ADA497908 (cit. on p. 2).

[11] V. A. Kudryavtsev *et al.*, "Monitoring subsurface CO2 emplacement and security of storage using muon tomography," *International Journal of Greenhouse Gas Control*, vol. 11, pp. 21–24, 2012, ISSN: 1750-5836. DOI: http://dx.doi.org/10.1016/j.ijggc.2012.07.023. [Online]. Available: http://www.sciencedirect.com/science/article/pii/S1750583612001806 (cit. on p. 2).

[12] A. Bonneville *et al.*, "Borehole muon detector development," in *2015 AGU Fall Meeting*, AGU, 2015. [Online]. Available: https://www.netl.doe.gov/File%20Library/Events/2015/carbon%20storage/proceedings/Bonneville-poster.pdf (cit. on p. 2).

[13] D. Bryman, J. Bueno, and J. Jansen, "Blind test of muon geotomography for mineral exploration," *ASEG Extended Abstracts*, vol. 2015, no. 1, pp. 1–3, 2015 (cit. on p. 3).

[14] K. N. Borozdin *et al.*, "Surveillance: Radiographic imaging with cosmic-ray muons," *Nature*, vol. 422, no. 6929, pp. 277–277, Mar. 20, 2003. [Online]. Available: http://dx.doi.org/10.1038/422277a (cit. on p. 3).

[15] C. Morris *et al.*, "Tomographic imaging with cosmic ray muons," *Science & Global Security*, vol. 16, no. 1-2, pp. 37–53, 2008 (cit. on p. 3).

[16] L. Schultz *et al.*, "Statistical reconstruction for cosmic ray muon tomography," *Image Processing, IEEE Transactions on*, vol. 16, no. 8, pp. 1985–1993, Aug. 2007, ISSN: 1057-7149 (cit. on p. 3).

[17] L. Cremonesi, "Cosmic ray muon tomography for anti-terrorism applications," Master's thesis, University College of London, 2011. [Online]. Available: https://www.hep.ucl.ac.uk/~rjn/creamtea/reports/Linda%20Cremonesi%20952446.pdf (cit. on p. 3).

[18] J. Armitage *et al.*, "First images from the CRIPT muon tomography system," *International Journal of Modern Physics Conference Series*, vol. 27, 1460129, p. 60 129, Feb. 2014. [Online]. Available: http://adsabs.harvard.edu/abs/2014IJMPS..2760129A (cit. on p. 3).

[19] J. Durham *et al.*, "Tests of cosmic ray radiography for power industry applications," *AIP Advances*, vol. 5, no. 6, p. 067 111, 2015 (cit. on p. 4).

[20] J. Perry *et al.*, "Imaging a nuclear reactor using cosmic ray muons," *Journal of Applied Physics*, vol. 113, no. 18, p. 184 909, 2013 (cit. on p. 4).

[21] H. Miyadera, "Discussion - next step for Fukushima Daiichi muon tomography," in. Los Alamos National Laboratory, Aug. 2012. [Online]. Available: http://www.osti.gov/scitech/servlets/purl/1048840 (cit. on p. 4).

[22] E. Guardincerri *et al.*, "Imaging the inside of thick structures using cosmic rays," *AIP Advances*, vol. 6, no. 015213, 2016. DOI: 10.1063/1.4940897. arXiv: 1601.01291 [physics.ins-det] (cit. on p. 4).

[23] M. Hohlmann *et al.*, "GEANT4 simulation of a cosmic ray muon tomography system with micro-pattern gas detectors for the detection of high-z materials," *Nuclear Science, IEEE Transactions on*, vol. 56, no. 3, pp. 1356–1363, 2009 (cit. on p. 4).

[24] B. Suerfu and C. G. Tully, "High resolution muon computed tomography at neutrino beam facilities," 2015. arXiv: 1501.07238 [physics.ins-det] (cit. on p. 4).

[25] K. Olive *et al.*, "Review of particle physics," *Chin.Phys.*, vol. C38, p. 090 001, 2014 (cit. on pp. 7, 8, 14, 105, 133).

[26] T. K. Gaisser, *Cosmic rays and particle physics*. Cambridge University Press, 1990 (cit. on p. 7).

[27] J. A. Smith and N. M. Duller, "Effects of pi meson decay-absorption phenomena on the high-energy mu meson zenithal variation near sea level," *Journal of Geophysical Research*, vol. 64, no. 12, pp. 2297–2305, 1959, ISSN: 2156-2202 (cit. on p. 7).

[28] H. Jokisch *et al.*, "Cosmic-ray muon spectrum up to 1 TeV at 75 zenith angle," *Phys. Rev. D*, vol. 19, pp. 1368–1372, 5 Mar. 1979. DOI: 10.1103/PhysRevD.19.1368. [Online]. Available: http://link.aps.org/doi/10.1103/PhysRevD.19.1368 (cit. on pp. 9, 10).

[29] T. Wada *et al.*, "Atmospheric muon measurements using the okayama telescope," *Nuclear Physics B - Proceedings Supplements*, vol. 151, no. 1, pp. 465–468, 2006, Proceedings of the XIII International Symposium on Very High Energy Cosmic Ray Interactions, ISSN: 0920-5632. DOI: http://dx.doi.org/10.1016/j.nuclphysbps.2005.07.080. [Online]. Available: http://www.sciencedirect.com/science/article/pii/S0920563205009710 (cit. on p. 9).

[30] R. F. Schwitters, "Analytic forms of cosmic ray spectra suitable for muon tomography," Muon tomography note, 2013, [Online]. Available: http://www.hep.utexas.edu/mayamuon/files/papers/spectra.pdf (cit. on pp. 9, 71).

[31] A. I. Barbouti and B. C. Rastin, "A study of the absolute intensity of muons at sea level and under various thicknesses of absorber," *Journal of Physics G: Nuclear Physics*, vol. 9, no. 12, p. 1577, 1983. [Online]. Available: http://stacks.iop.org/0305-4616/9/i=12/a=018 (cit. on pp. 10, 111, 135).

[32] D. Reyna, "A simple parameterization of the cosmic-ray muon momentum spectra at the surface as a function of zenith angle," Jun. 2006. arXiv: hep-ph/0604145v2 [hep-ph] (cit. on pp. 11, 67, 71, 134, 135).

[33] E. V. Bugaev *et al.*, "Atmospheric muon flux at sea level, underground, and underwater," *Phys. Rev. D*, vol. 58, p. 054 001, 5 Jul. 1998. DOI: 10.1103/PhysRevD.58.054001. [Online]. Available: http://link.aps.org/doi/10.1103/PhysRevD.58.054001 (cit. on p. 11).

[34] D. Groom and S. Klein, "Passage of particles through matter," *The European Physical Journal C - Particles and Fields*, vol. 15, pp. 163–173, 1 2000, 10.1007/BF02683419, ISSN: 1434-6044 (cit. on p. 13).

[35] W. Lohmann, R. Kopp, and R. Voss, "Energy loss of muons in the energy range 1-10000 GeV," *CERN Report 85-03*, 1985. [Online]. Available: http://inspirehep.net/record/213550/ (cit. on p. 14).

[36] T. Cundiff *et al.*, "The MINOS near detector front end electronics," *IEEE Trans. Nucl. Sci.*, vol. 53, pp. 1347–1355, 2006. DOI: 10.1109/TNS.2006.876771 (cit. on pp. 17, 18).

[37] E. T. Wright, "A detector for muon tomography: Data acquisition and preliminary results," Master's thesis, University of Texas at Austin, May 2007 (cit. on p. 17).

[38] C. Hui, "Maya muon tomography: Muon tracking, and muon simulation," Master's thesis, University of Texas at Austin, Aug. 2007 (cit. on p. 17).

[39] G. Thurston, "Cosmic ray detection and tomographic imaging," Undergraduate Senior Thesis, University of Texas at Austin, May 2012 (cit. on pp. 17, 22).

[40] N. Tagg *et al.*, "Performance of Hamamatsu 64-anode photomultipliers for use with wavelength—shifting optical fibres," *Nuclear Instruments and Methods in Physics Research Section A: Accelerators, Spectrometers, Detectors and Associated Equipment*, vol. 539, no. 3, pp. 668–678, 2005, ISSN: 0168-9002. DOI: http://dx.doi.org/10.1016/j.nima.2004.11.003. [Online]. Available: http://www.sciencedirect.com/science/article/pii/S0168900204023460 (cit. on p. 20).

[41] C. Posch, E. Hazen, and J. Oliver, *Atlas muon note revision 2.1*, Harvard University, Sep. 2007 (cit. on pp. 22, 24).

[42] S. Avvakumov *et al.*, "Spontaneous light emission from fibers in MINOS," *Nuclear Instruments and Methods in Physics Research Section A: Accelerators, Spectrometers, Detectors and Associated Equipment*, vol. 545, no. 1–2, pp. 145–155, 2005, ISSN: 0168-9002. DOI: http://dx.doi.org/10.1016/j.nima.2005.01.340. [Online]. Available: http://www.sciencedirect.com/science/article/pii/S0168900205005875 (cit. on p. 23).

[43] T. H. Group, *Hierarchical data format, version 5*, 1997. [Online]. Available: http://www.hdfgroup.org/HDF5/ (cit. on pp. 27, 83).

[44] R. F. Schwitters, "Pattern-recognition and reconstruction for muon tracking," Tracking note, 2006, [Online]. Available: http://www.hep.utexas.edu/mayamuon/files/papers/recon.pdf (cit. on p. 29).

[45] R. Brun and F. Rademakers, "Root—an object oriented data analysis framework," *Nuclear Instruments and Methods in Physics Research Section A: Accelerators, Spectrometers, Detectors and Associated Equipment*, vol. 389, no. 1, pp. 81–86, 1997 (cit. on p. 40).

[46] H. A. Bethe, "Molire's theory of multiple scattering," *Phys. Rev.*, vol. 89, pp. 1256–1266, 6 Mar. 1953. DOI: 10.1103/PhysRev.89.1256. [Online]. Available: http://link.aps.org/doi/10.1103/PhysRev.89.1256 (cit. on p. 44).

[47] R. F. Schwitters, "Detector-based track parameters," Tracking parameters note, Mar. 2013, [Online]. Available: http://www.hep.utexas.edu/mayamuon/files/papers/tracking2013.pdf (cit. on p. 56).

[48] J. Amanatides and A. Woo, "A fast voxel traversal algorithm for ray tracing," in *Proceedings of EUROGRAPHICS*, vol. 87, 1987, pp. 3–10. [Online]. Available: http://www.cse.yorku.ca/~amana/research/grid.pdf (cit. on p. 66).

[49] G. Cosmo, "The Geant4 geometry modeler," in *Nuclear Science Symposium Conference Record, 2004 IEEE*, vol. 4, Oct. 2004, 2196–2198 Vol. 4 (cit. on p. 78).

[50] K. Lang *et al.*, "A comprehensive characterization of Hamamatsu 16- and 64-anode PMTs," *Nucl. Instrum. Meth.*, vol. A461, pp. 571–573, 2001. DOI: 10.1016/S0168-9002(00)01302-4 (cit. on p. 80).

[51] S. Agostinelli *et al.*, "Geant4—a simulation toolkit," *Nuclear Instruments and Methods in Physics Research Section A: Accelerators, Spectrometers, Detectors and Associated Equipment*, vol. 506, no. 3, pp. 250–303, 2003, ISSN: 0168-9002. DOI: http://dx.doi.org/10.1016/S0168-9002(03)01368-8. [Online]. Available: http://www.sciencedirect.com/science/article/pii/S0168900203013688 (cit. on p. 80).

[52] J. Allison *et al.*, "Geant4 developments and applications," *IEEE Transactions on Nuclear Science*, vol. 53, no. 1, pp. 270–278, Feb. 2006, ISSN: 0018-9499. DOI: 10.1109/TNS.2006.869826 (cit. on p. 80).

[53] B. Dawes, D. Abrahams, R. Rivera, *et al.*, "Boost C++ libraries," *URL http://www.boost. org*, vol. 35, p. 36, 2009 (cit. on p. 81).

[54] K. Martin and B. Hoffman, *Mastering CMake*. Kitware, 2015 (cit. on p. 81).

[55] D. M. Beazley, "Swig: An easy to use tool for integrating scripting languages with C and C++," in *Proceedings of the 4th Conference on USENIX Tcl/Tk Workshop, 1996 - Volume 4*, ser. TCLTK'96, Monterey, California: USENIX Association, 1996, pp. 15–15. [Online]. Available: http://dl.acm.org/citation.cfm?id=1267498.1267513 (cit. on p. 83).

[56] J. Erdfelt and D. Drake, *Libusb*, 2007. [Online]. Available: http://www.libusb.info (cit. on p. 83).

[57] N. Agafonova *et al.*, "Measurement of the atmospheric muon charge ratio with the OPERA detector," *The European Physical Journal C-Particles and Fields*, vol. 67, no. 1, pp. 25–37, 2010 (cit. on p. 93).

[58] A. Astbury and D. Axen, "Comparison of Geant4 simulation of atmospheric cosmic rays with measured terrestrial muon and neutron spectra," *TRI-PP-06-14*, vol. 1, p. 10, 2006. [Online]. Available: http://publications.triumf.ca/pub/arch06/pp-06-14.pdf (cit. on p. 93).

[59] C. Sanderson, "Armadillo: An open source C++ linear algebra library for fast prototyping and computationally intensive experiments," NICTA, Tech. Rep., 2010 (cit. on p. 95).

[60] S. Behnel *et al.*, "Cython: The best of both worlds," *Computing in Science and Engineering*, vol. 13, pp. 31–39, 2011 (cit. on p. 95).

[61] F. Prez and B. E. Granger, "IPython: A system for interactive scientific computing," *Computing in Science and Engineering*, vol. 9, no. 3, pp. 21–29, May 2007, ISSN: 1521-9615. DOI: 10.1109/MCSE.2007.53. [Online]. Available: http://ipython.org (cit. on p. 95).

[62] J. D. Hunter, "Matplotlib: A 2D graphics environment," *Computing In Science & Engineering*, vol. 9, no. 3, pp. 90–95, 2007 (cit. on p. 95).

[63] Texas Advanced Computing Center (TACC), The University of Texas at Austin, *Lonestar 5* (cit. on p. 96).

[64] O. Allkofer, K. Carstensen, and D. Dau, "The absolute cosmic ray muon spectrum at sea level," *Phys.Lett.*, vol. B36, pp. 425–427, 1971. [Online]. Available: http://inspirehep.net/record/69152/ (cit. on pp. 111, 112).

[65] R. Bellotti *et al.*, "Measurement of the negative muon spectrum between 0.3 and 40 gev/$c$ in the atmosphere," *Phys. Rev. D*, vol. 53, pp. 35–43, 1 Jan. 1996. [Online]. Available: http://link.aps.org/doi/10.1103/PhysRevD.53.35 (cit. on p. 111).

[66] B. C. Rastin, "An accurate measurement of the sea-level muon spectrum within the range 4 to 3000 GeV/c," *Journal of Physics G: Nuclear Physics*, vol. 10, no. 11, p. 1609, 1984. [Online]. Available: http://stacks.iop.org/0305-4616/10/i=11/a=017 (cit. on p. 111).

[67] C. Hagmann, D. Lange, and D. Wright, "Monte carlo simulation of proton-induced cosmic-ray cascades in the atmosphere," Lawrence Livermore National Laboratory, Tech. Rep., Feb. 2012 (cit. on p. 111).